ELECTRICAL AND OPTICAL PROPERTIES OF RRAM

by

Yubo Cui

A thesis submitted to the Graduate Council of
Texas State University in partial fulfillment
of the requirements for the degree of
Master of Science
with a Major in Materials Physics
August 2016

Committee Members:

Wilhelmus Geerts, Chair

Casey Smith

Alexander Zakhidov

FAIR USE AND AUTHOR'S PERMISSION STATEMENT

Fair Use

Duplication Permission

ACKNOWLEDGEMENTS

I would like to thank Dr. Wilhelmus Geerts for guiding me during thesis research. Also, I would like to thank Dr. Ravi Droopad for giving me access to the Ellipsometer in the MBE lab, and Dr. Casey Smith and Dr. Eric Shires for training me. Furthermore Dr. Alex Zhakidov for the thin film class to make the RRAM test sample, and Dr. Stefan Zollner for the FTIR measurements at Sandia National Lab and additional measurements at NMSU on our cleaned substrates. Also James shook and Ricky Scott need to be thanked for help with electrical characterization of the device wafer.

Furthermore, I would like to thank Shane Arabie from Engineering Technology for letting us use the bead-blaster.

The work at Tx state University was funded by a Texas State research enhancement grant, a thesis support fellowship of the Graduate College, and a DOD grant ((HBCU/MI grant W911NF-15-1-0394). The work at NMSU was funded by the National Science Foundation (DMR-1104934). The FTIR measurements were performed at the Center for Integrated Nanotechnologies, an Office of Science User Facility operated for the U.S. Department of Energy (DOE) Office of Science. Sandia National Laboratories is a multi-program laboratory managed and operated by Sandia Corporation, a wholly owned subsidiary of Lockheed Martin Corporation, for the U.S. Department of Energy's National Nuclear Security Administration under contract DE-AC04-94AL85000.

Part of this thesis was presented at various scientific meetings and published elsewhere including:

[1] Yubo Cui, Wilhelmus Geerts, Fidele Twagirayezu, Stefan Zollner, "IR Ellipsometry on RF sputtered Permalloy Oxide thin films", National APS-March Meeting, 2015, San Antonio, Texas.

[2] Fidele Twagirayezu, Wilhelmus Geerts, Yubo Cui, "Optical Properties of Magnetron Sputtered Nickel Thin Films", National APS-March Meeting, 2015, San Antonio, Texas.

[3] Yubo Cui, Wilhelmus J. Geerts, “The Influence of the Deposition Parameters on the Film Thickness of RF sputtered Permalloy Oxide Thin Films, 6h. International Research Conference for Graduate Students, Texas State University, November 5-6, 2014.

[4] Yubo Cui, Fidele Twagirayezu, Wilhelmus Geerts, Optical Properties of Permalloy Oxide Grown by reactive RF magnetron sputtering, presentation at the 2014-Fall meeting of the Texas Section of the American Physical Society, October 17-19, College Station, 2014.

[5] Leonardo I. Escandon Jackson, Yubo Cui, Wilhelmus J. Geerts, Magnetometer measurements on large samples for magneto-plastic research, Undergraduate Research Conference and Honors Thesis Forum, Texas State University April 24, 2015.

[6] James Shook, Yubo Cui, Md Abdul Ahad Talukder, Tang Xi, Greg McClendon, Alex Zakhidov, Luisa Scolfaro, Wilhelmus Geerts, Sheet resistance measurements on a Fe-

doped NiO ReRam Test Chip, oral presentation 2015 TSAPS-Fall meeting Baylor University, October 29-31, Texas.

[7] Yubo Cui, Md Abdul Ahad Talukder, Greg McClendon, Yubo Cui, Xi Tang, Wilhelmus Geerts. Iron Doped NiO Based Resistive RAM Test Chip, oral presentation 7th international research conference for graduate students, Texas State University, Nov. 17-18, 2015.

[8] Md Abdul Ahad Talukder**,** Yubo Cui, Wilhelmus J. Geerts, Study of the Crystal Properties of Iron Doped NiO using an X-ray Diffractometer, oral presentation 7th international research conference for graduate students, Texas State University Nov. 17-18, 2015.

[9] Md Abdul Ahad Talukder, Yubo Cui, Maclyn Compton, Wilhelmus Geerts, Luisa Scolfaro and Stefan Zollner, FTIR Ellipsometry Study on RF sputtered Permalloy-Oxide Thin Films, published in MRS Advances spring 2016. doi:10.1557/adv.2016.427.

TABLE OF CONTENTS

Page

LIST OF TABLES

Table **Page**

LIST OF FIGURES

Figure **Page**

ABSTRACT

Recently several electronic devices have achieved significant enhancements that have been attributed to an oxidized NiFe layer. A study on lateral spin valves, was found to have an increased magnetoresistance after leaving it exposed to air. The enhancements were attributed to the partly oxidation of a NiFe layer [1]. Even more recently the turn on voltages of Hematite based water splitting devices was lowered to record low of .61 V with the addition of an amorphous $NiFeO_x$ layer [1]. We investigated the optical properties of Ni_xFe_{1-x}-oxide thin films that were deposited by reactive RF sputtering on different substrates. Deposition was performed in an AJA Magnetron System using a gas flow of 10 sccm and a sputter pressure of 10^{-3} Torr. Ni_xFe_{1-x}Oxide films were made for different substrate temperatures (room temperature-588 degrees Celsius), different deposition times (38-1200s), and different Oxygen flow rates (5-20%). Films with two different Fe concentrations were studied (10-19 at.%). The optical properties of the films from the UV to the far IR were studied by ellipsometer as a function of the deposition parameters. The electrical properties were studied by the linear four-point probe technique. Chemical composition, morphology and roughness were studied by EDAX, SEM, and AFM. In addition, three real RRAM memory cell device test wafers were made.

I. INTRODUCTION

1.1 Permalloy oxide

Permalloy ($Ni_{0.81}Fe_{0.19}$) was invented in 1914 by physicist Gustav Elmen at Bell Telephone Laboratories. Permalloy was first used for inductive compensation in submarine telegraph cables to prevent signal distortion. It has high enough permeability to increase the inductance significantly and turn the transatlantic telegraph cable into a loaded line with reduced distortion. Since then permalloy has found application in a lot of other devices including sensors and actuators [2]. Permalloy is a soft magnetic material, whose magnetization is easily modified by a magnetic field. Its magnetic properties do not depend on stress, a parameter difficult to control in thin film devices. The hard disk drive was introduced by IBM in 1956. It is using a ferromagnetic material to store the data. A thin magnetic layer is magnetized by a recording head, and written bits are read by a reading head as shown in Fig. 1. The high permeability of the Permalloy and also the high magneto-resistive effect, low magnetostriction and stability under high frequency operation make permalloy a very suitable material for hard disk read/write heads [3][4].

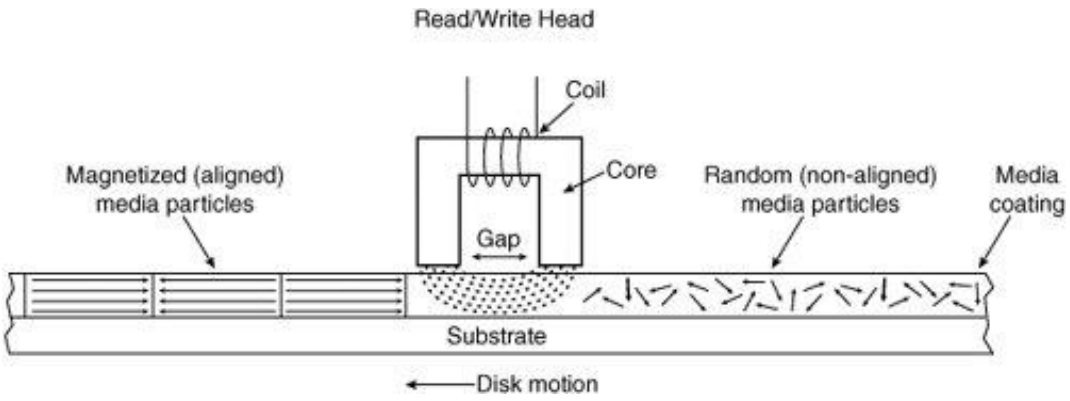

Fig. 1. Working method of the hard disk drive [5]

1.1.1 Defect as the oxide of Py

As discussed above permalloy itself is a widely used ferromagnetic material in sensors and actuators because of its very high permeability. On the other hand, Permalloy oxide is not a well-known material. In oxidized form, Permalloy will lose all its attractive magnetic properties. Permalloy Oxide is no longer a ferromagnetic material but anti-ferromagnetic. Permalloy Oxide (PyO) also has a high resistivity (> 4 $\cdot 10^3$ Ω cm) [6] and is no longer magneto-resistive. By oxidation, a device containing Permalloy can lose its function. In industry, PyO was thought of as a kind of defect and one would try to avoid oxidation of the permalloy by appropriate encapsulation [7]. Therefore, little is known about permalloy oxide. Very recently Permalloy Oxide has been shown to enhance strongly the performance of lateral spin valve devices. [8][9][10]. Not a little bit but significantly, i.e. a factor 5-10, so interesting for applications. In order to apply PyO in devices, though, it is necessary to know more about its properties. In particularly its optical and electrical properties need to be well understood.

1.2 Resistive random access memory

Fe-doped NiO also has another possible application. Flash memory that is currently used in mobile devices faces a scaling challenge beyond the 14 nm technology node. The industry is currently looking for a new technology. One of the promising candidate's technology is resistive random access memory (RRAM) [11]. A RRAM device is based on three parts i.e. two electrodes with a switching material, an oxide, in between. RRAM devices use the soft breakdown of the metal oxide to save data. Various oxide materials are applied in RRAM including transition metal oxides, chalcogenides, and perovskites [12]. The metal oxide usually has a very large resistance. But during the writing process, the resistivity of the oxide can be modified by creating a controlled soft breakdown in the oxide. The switching material can be changed between two different resistivity values, a low resistance metallic state, and a high resistance semiconducting or insulating state. So the data is stored in the resistivity value of the oxide rather than in charge. The different resistance levels are controlled by the voltage on the electrodes. The current that is allowed to flow through the device also plays a role in the set and reset processes.

The switching material will break down when the voltage of the electrodes is as large as the switching voltage, and a conductive path will form from the top to the bottom electrodes. It is believed that oxygen ions and or oxygen vacancies move if a high electric field is applied to the oxide creating a high conducting path between top and bottom electrode. The conducting path also referred to as a conductive filament (CF),

will let the electrons move more than 1000 times easier than in the high resistance state, lowering the resistance of the device. As the study of NiO shows, the resistance of RRAM devices can be changed from 30Ω to 10kΩ [13]. The conducting path will not need a certain voltage to hold it. That is the RRAM device does not need a power supply or battery to keep the data in the memory and is nonvolatile similar to flash memory. The device can be switched into a high resistance state by providing a large current, upon which local heating will destroy the conducting path. This reset operation is explained by oxidation of metallic elements in the conductive filament [14].

1.2.1 Switching in NiO RRAM

The transition metal NiO is a common material used as a switching material in RRAM devices and its switching properties and also its deposition processes have been recently extensively studied. The switching behavior in NiO is much more complicated than discussed above and is still not well understood. The NiO has two different switching behaviors, unipolar and bipolar switching [15]. In unipolar switching, resistance change takes place irrespective of the pulse polarity. The unipolar switching mode is similar as discussed before. Switching back to the high resistance state is accomplished by thermal processes. NiO RRAM can also be operated in a bipolar mode. For those devices, the resistance level can be only returned to a high resistance state by an opposite voltage [16]. For bipolar switching also ion migration contributes to the dissolution process in addition to pure diffusion.

The high resistance state in bipolar NiO behaves like a metal-semiconductor hetro-junction so depends on both the oxide and the electrode material. Both unipolar and bipolar switching processes can be used to store data. They are therefore referred to as memory switching.

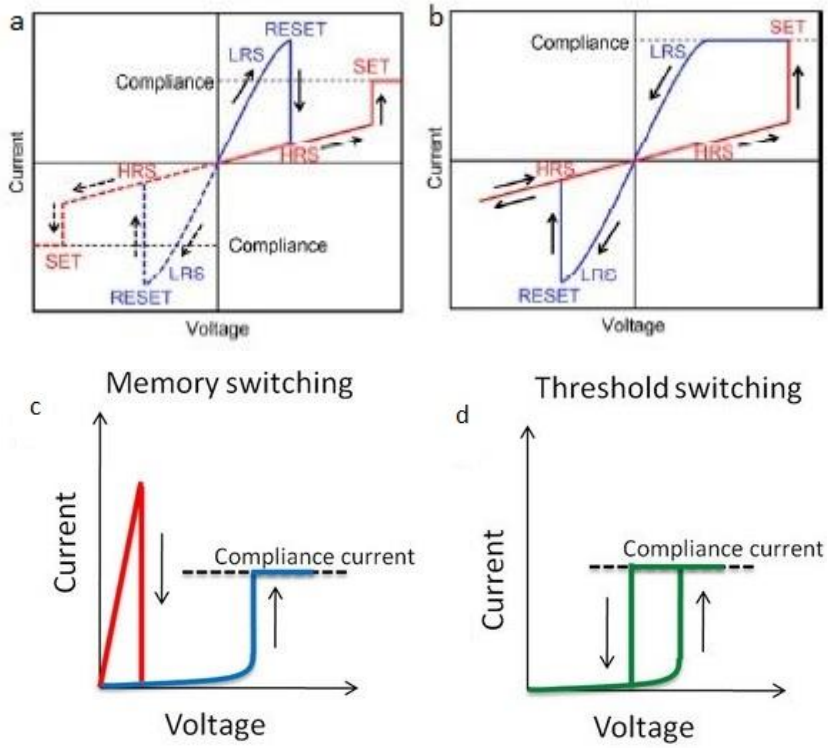

Fig. 2. Unipolar switching and bipolar switching (a,b) [17], and difference between memory switching and threshold switching (c,d) [18]

If NiO-RRAM devices are made with a large oxygen concentration the low resistance state is no longer stable and the device will return to the high resistance state at zero volts. This is called threshold switching. When the voltage across the semiconductor increases above a threshold value, the number of free carriers in the material will increase very quickly. So at the threshold voltage, the material is switched from a high resistance to a low resistance state. The resistance will return back to high

resistance when the voltage is lower than a certain voltage. The threshold devices cannot keep the data without a battery or power supply connected. The difference between the soft breakdown and threshold switching behavior is shown at the bottom of Fig. 2 [18].

There are two important parameters for the switching properties of RRAM. The electric field plays a major role in the set process. The soft break-down process needs a large enough voltage to make a free path for the free electrons, so they can move easily through the switching material. The reset process is mainly driven by thermal processes, so depends on the resistivity. Therefore, the two most important electric properties of the metal oxide of RRAM are the resistivity and the dielectric constant. If the material has a low resistivity and becomes too conductive in the high resistance state, it will no longer be possible to induce a soft break-down.

The reason we would like to add iron to NiO thin films is that the NiO can have a rather low resistivity, in particularly when samples are made at high oxygen pressure. Adding Fe could increase the resistivity of the high resistance state significantly. RF sputtered Permalloy-Oxide (PyO), i.e. $Ni_{0.81}Fe_{0.19}O_{1-\delta}$, has a resistivity of about order of $4*10^3$ Ω cm[6]. It is expected that a higher resistivity from the additional Fe doping will make the difference between the high and low resistance levels of the RRAM larger. This would improve the reading process of the PyO RRAM. A higher resistivity can also limit the operating current and lower the switching energies involved in the set processes. This thesis focuses on the properties of Fe-doped NiO and its use in RRAM devices.

1.3 Research Plan

To better understand the properties of sputtered NiFe-oxide, several thin film series were made in the clean room at Texas State University. The first series was a temperature series. It was made to determine how the electrical properties, optical properties, and the crystal structure depend on the deposition temperature (see chapter 3). The second film series was a thickness film series. This series was made to understand better how the properties of PyO change with the film thickness. A series of PyO films with thicknesses from less than 10 nm to 150 nm was made. Details on the thickness series are provided in Chapter 4. The next film series was the Oxygen flow rate series. The Oxygen concentration can change the RRAM switching behavior as it can significantly impact the resistivity of the thin film and thus its switching properties. Films were deposited for different Oxygen concentrations in the sputter gas (5-20%) with the total pressure during sputtering around 10^{-3} Torr. The result of the oxygen flow rate series can be found in Chapter 5.

Finally, three real RRAM cell device wafers were made using NiO, $Ni_{0.9}Fe_{0.1}O_{1-\delta}$ and $Ni_{0.81}Fe_{0.19}O_{1-\delta}$ as the switching material. Although none of the wafers showed clear unipolar resistive switching, the process to make the wafers as well as preliminary electrical and optical measurements on the realized wafers are reported on in Appendix VI of this thesis.

II. EQUIPMENT

2.1 Ellipsometer

To determine the thickness and also the optical properties of the thin PyO films, five ellipsometers were used in this study: A spectroscopic multi-angle Woollam M2000 ellipsometer with a spectral range from 215 to 1000 nm (MBE lab, Tx state), a spectroscopic multi-angle Woollam M2000 ellipsometer with a spectral range of 245.8 to 1688.3 nm (RSC Tx state), a Horiba fixed angle ellipsometer with a spectral range of 235 to 1000 nm (on loan from Texas Lutheran University), a variable angle VVASE Woollam ellipsometer with a spectral range of 188 to 2500 nm (New Mexico State University), and a variable angle Woollam FTIR ellipsometer with a spectral range from 1700 to 30000 nm (Sandia National Lab). The same samples that were measured by different ellipsometers showed comparable results. The Woollam M2000 ellipsometers can measure the ellipsometric quantities at different wavelengths at the same time as it uses fast spectral detection methods. The Horiba ellipsometer and the Woollam VVASE use a monochromator, so measurements are made at one wavelength at a time. It makes the measurement time much longer on that kind of ellipsometer. The wavelength bandwidth of such ellipsometers is much better though as double monochromators with superior stray light suppression can be employed. In particularly when analyzing thicker films a narrow spectral bandwidth is important.

2.1.1 Principle of Ellipsometry

If two parallel plane waves move in the z-direction and have an electric field amplitude E_{ox} and E_{oy} in the x and y-direction and have the same phase, the resulting EM-wave is linearly polarized as shown in Fig. 3 on the left. If those two plane waves have a 90-degree phase difference, the sum electric field vector at a specific location describes a circle as is shown in Fig. 3 on the right. It is called circularly polarized light. The ellipsometer is based on the change of the state of polarization of a light beam upon reflection with the material. In general, elliptically polarized incident light is used in the instrument.

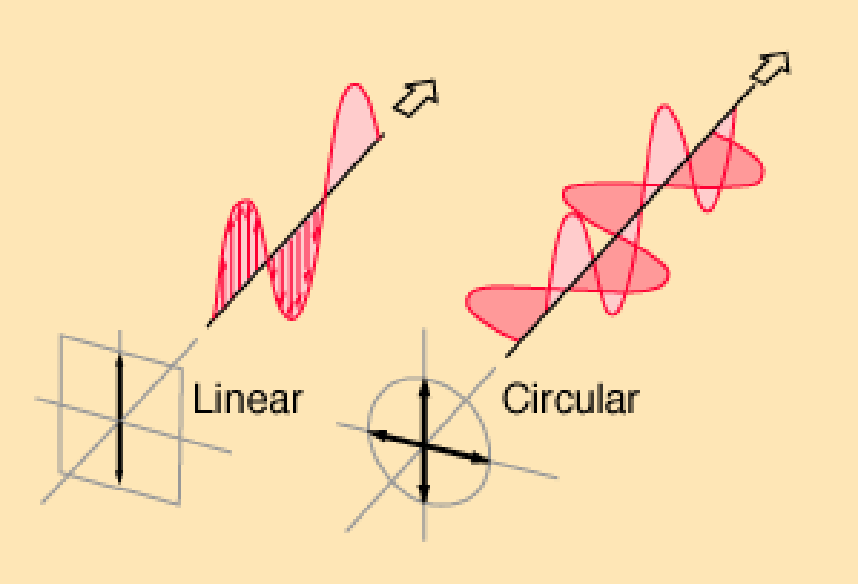

Fig. 3. Linearly polarized light (left) and circularly polarized light (right) [19]

The light reflected from a certain material may change its state of polarization upon reflection. For flat samples with a planar surface, this is described by the Fresnel

reflection coefficients. The Fresnel equations for the light polarized perpendicular and parallel to the plane of incidence are given by [20]

$$\mathrm{r_{ss}} = \frac{E_{rs}}{E_{is}} = \frac{\tilde{n}_1 \cos\theta_i - \tilde{n}_2 \cos\theta_\mathrm{t}}{\tilde{n}_1 \cos\theta_i + \tilde{n}_2 \cos\theta_\mathrm{t}}$$
$$\mathrm{r_{pp}} = \frac{E_{rp}}{E_{ip}} = \frac{\tilde{n}_2 \cos\theta_i - \tilde{n}_1 \cos\theta_\mathrm{t}}{\tilde{n}_2 \cos\theta_i + \tilde{n}_1 \cos\theta_\mathrm{t}} \qquad \text{[Equation 2.1]}$$

$\mathrm{r_{ss}}, \mathrm{r_{pp}}$ ---Fresnel Reflection Coefficients of s wave and p wave

$\tilde{n}_1$ ---complex index of reflection of ambient material

$\tilde{n}_2$ ---complex index of reflection of refraction material under study

θ_i ---angle of incidence

θ_t ---angle of refraction

The complex refraction index consists of a real part n which describes the velocity of the EM wave in the material, and an imaginary part k. The imaginary part is the extinction coefficient and describes the absorption of the wave in the material. In ellipsometry it is common to combine both quantities in the complex refraction index:

$$\tilde{n} = n - ik \qquad \text{[Equation 2.2]}$$

Note that there are different definitions of the complex refraction index. The definition of equation [2.2] is called the Nebraska convention [20].

The angle of incidence and the angle of refraction are related to each other by Snell's law:

$$\tilde{n}_1 \sin(\theta_i) = \tilde{n}_2 \sin(\theta_t) \qquad \text{[Equation 2.3]}$$

The change of polarization is expressed by two parameters, i.e. the amplitude ratio of the reflection coefficients (tan(Ψ)) and the phase shift difference of the Fresnel

reflection coefficients (Δ). The complex ellipsometric quantity gives the relationship with Fresnel Reflection Coefficients [20]:

$$\rho = \frac{r_{pp}}{r_{ss}} = \tan\psi \, \mathrm{e}^{\mathrm{i}\Delta} \qquad \text{[Equation 2.4]}$$

ρ ---complex ellipsometric quantity

tan(Ψ) ---amplitude ratio

Δ ---phase difference

Ellipsometers can measure Ψ and Δ for different photon energy or wavelength and also for different angles of incidence. The measurement results are used to calculate the optical properties using the Fresnel reflection coefficient equations provided above

If more than one layer is included in the sample, the total reflection coefficient is calculated from applying the Fresnel reflection coefficients for each interface. For a thin film on an infinite substrate, the following expressions are used to calculate the optical properties. [20]

$$R^p = \frac{r_{12}^p + r_{23}^p \exp(-i2\beta)}{1 + r_{12}^p r_{23}^p \exp(-i2\beta)}$$

$$R^s = \frac{r_{12}^s + r_{23}^s \exp(-i2\beta)}{1 + r_{12}^s r_{23}^s \exp(-i2\beta)} \qquad \text{[Equation 2.5]}$$

$$\beta = 2\pi(\frac{d}{\lambda})\tilde{n}_2 \cos\phi_2$$

r_{12}^p, r_{12}^s ---Fresnel Reflection Coefficients of s wave and p wave between air and the thin film material.

r_{23}^p, r_{23}^s ---Fresnel Reflection Coefficients of s wave and p wave between thin film material and the substrate material

d ---the film thickness

λ ---wavelength

R^s, R^p --- Total Fresnel reflection coefficient of the thin film system

The equation is much more complicated if the sample contains more layers and in general it is not possible to calculate the optical properties directly from the measurement data and angle of incidence, i.e. from ϕ, Ψ and Δ. So a model of the sample is needed and advanced data-analysis techniques to determine the model parameters from the data measured at different photon energies and different angles of incidence.

From the ellipsometric quantities, Δ and Ψ, one can determine the optical properties, film thickness, and also the roughness of the sample. The Fresnel reflection coefficients given above (equations [2.1]) are only valid for an infinite thick sample. Infinite thick means that the reflection from the bottom surface of the film is too weak and is not measurable. For most of our samples, this condition is not met, and the reflection of the light from the thin film substrate interface is noticeable. As it is not possible to determine the inverse function of equation [2.5], the measurement data and a model need to be used in a fitting process to determine the optical properties or film thickness. One starts with an educated guess for the model parameters and calculates the ellipsometric quantities Δ and Ψ. The difference between the calculated and measured Δ and Ψ is used to modify the model parameters until calculated and measured Δ and Ψ differ less than a certain amount. The difference between measured and calculated ellipsometric quantities is the

mean square error (MSE). There are different definitions of the MSE. For the data measured with the Horiba ellipsometer the following definition was used:

$$MSE = \frac{1}{N - M - 1}\sum_{i=1}^{n}[(\frac{\Psi_{E_i} - \Psi_{G_i}}{\sigma})^2 + (\frac{\Delta_{E_i} - \Delta_{G_i}}{\sigma})^2 + (\frac{R_{E_i} - R_{G_i}}{\sigma})^2] \quad \text{[Equation 2.6]}$$

N ---the number of wavelengths

M ---the number of fit parameters

Ψ ---the amplitude ratio

Δ ---the phase difference

R ---reflectivity

σ ---estimated uncertainty in the experimental values (0.5 to 0.1%)

E ---refers to the measured data

G ---refers to the model generated data [21]

The definition of MSE for the Woollam ellipsometers is:

$$MSE = \sqrt{\frac{1}{3n - m}\sum_{i=1}^{n}[(\frac{N_{E_i} - N_{G_i}}{0.001})^2 + (\frac{C_{E_i} - C_{G_i}}{0.001})^2 + (\frac{S_{E_i} - S_{G_i}}{0.001})^2]} \quad \text{[Equation 2.7]}$$

n ---the number of wavelengths

m ---the number of fit parameters

N ---Cos(2Ψ)

C ---Sin(2Ψ)Cos(Δ)

S ---Sin(2Ψ)Sin(Δ)

E ---refers to the measured data

G ---refers to the model generated data

2.1.2 Light Source, filter, and Detector

An ellipsometer includes a light source, a polarizer, a sample stage, an analyzer, possible additional polarizing optics, and a detector. Fig. 4 shows the diagram of a rotating analyzer ellipsometer. The light source of all ellipsometers used in this thesis generates a certain range of wavelengths. The light is linearly polarized after going through the polarizer and reaches the sample. The reflection of the light will go through a rotating analyzer, and the intensity is measured by the detector. The measured intensity depends on the analyzer angle and thus consists of a DC and AC component. For different type of ellipsometers different optical components are rotated which results in specific relations between the measured intensity and the ellipsometric quantities Δ and Ψ.

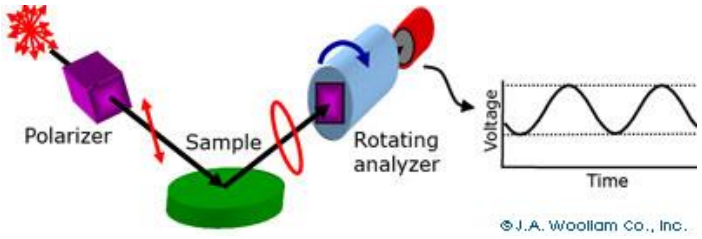

Fig. 4. Diagram of ellipsometer [22]

Woollam M2000 ellipsometer (MBE lab, TxS state)

The Woollam M2000 ellipsometer that is shown at the top of Fig. 5 employs a Xe Arc Lamp as light source. The M2000 is a rotating compensator ellipsometer. Before the light reaches the sample, the light is linearly polarized by a prism polarizer. The Woollam ellipsometer has a continuously rotating compensator that is made of an anisotropic material that has a different refraction index for different polarization directions. An analyzer is placed after the rotating compensator before the detector. The details of the rotating compensator ellipsometer is shown at the bottom of Fig.

5. The detector converts the light signal into an electronic signal. It cannot follow the high optical frequency of the EM-wave's electric field (10^{14}Hz) so measures the average of the EM radiation. Δ and ψ can be determined from the AC and DC components of the detector signal [23]. The M2000 Woollam ellipsometer has a CCD detector array. A diffraction grating is used to separate the different wavelength of the light reflected from the sample on a linear CCD detector. The resolution per CCD pixel is 1.6 nm. The spectral bandwidth, however, is 5 nm. Measurements can be made for different angles of incidence of the light. At all time, the angle of incidence is kept equal to the angle of reflection.

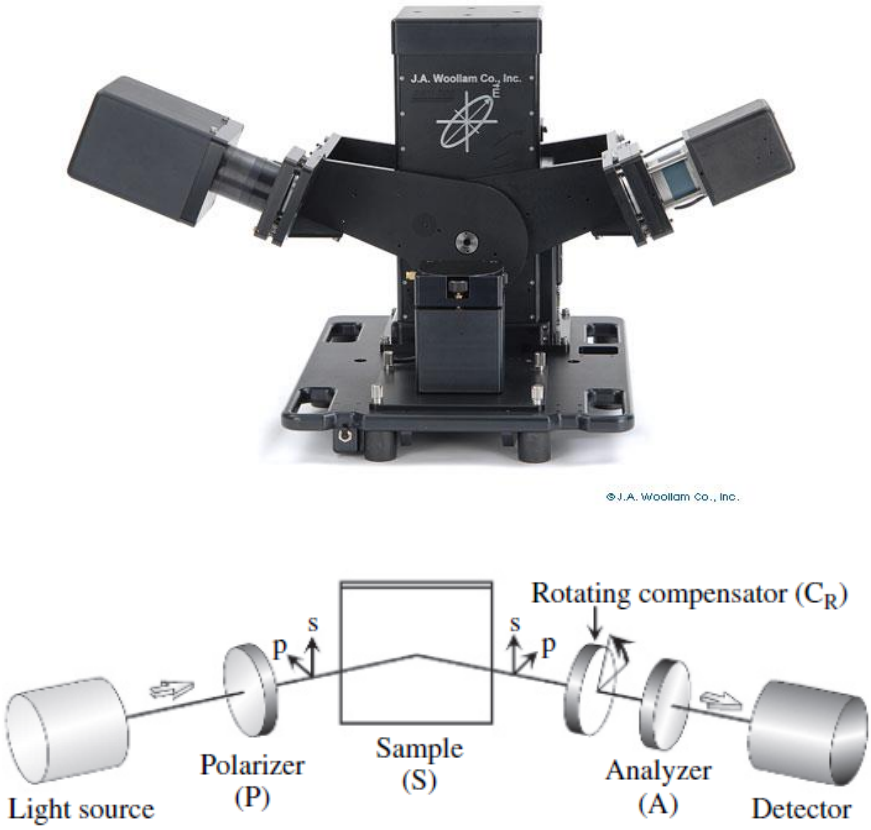

Fig. 5. Woollam M2000 ellipsometer (top) [22] and schematic diagram of RC-ellipsometer (bottom) [23]

Spectroscopic multi-angle Woollam M2000 ellipsometer (RSC Tx state)

The M2000 ellipsometer in RSC is similar as the Woollam M2000 ellipsometer in the MBE lab. The only difference is the spectral range of the lamp. This ellipsometer can measure from 245.8 to 1688.3 nm and has a larger range into the near infrared. To measure that far in the near infrared of the spectrum, the ellipsometer is furnished with two different CCD detectors. One for the visible (1.6 nm/pixel) and one for the NIR (3.4 nm/pixel). The spectral resolution for the visible and UV is 5 nm, and the spectral resolution for the NIR is 10 nm.

Horiba UVISEL ellipsometer with fixed angle of incidence (on loan from Texas Lutheran University in Seguin)

An ozone free Xenon lamp is used as the light source. The spectral range of the instrument is from 230 to 2100 nm. The Horiba ellipsometer returns a large noise on the high energy part of the spectrum, i.e. below 250 nm. Measurements below 250 nm can be performed if the ozone free lamp is exchanged with its UV version. For measurements lower than 200 nm, nitrogen needs to be used to protect the optics and to avoid the absorption of the light by the Oxygen in the air. The Horiba ellipsometer is a modulating ellipsometer employing a Photoelastic Modulator (PEM) made of fused silica. A drawing of the ellipsometer's optics is provided in Fig. 6 below. The PEM consists of a transducer coupled to a fused silica optical flat. The transducer generates a high frequency sound wave in the fused silica resulting in a

standing sound wave in the optical head. The periodic mechanical strain results in a modulation of the refraction index for one of the polarization directions. Light linearly polarized along the modulation axis moves faster/slower because of the modulated phase velocity. The Horiba ellipsometer has a photomultiplier detector for the UV-VIS part of the spectrum and an InGaAs photodiode detector for the NIR part of the spectrum. A monochromator is used to select the wavelength. The monochromator is placed between the sample and the detector. More details on the relation between the detector signal and the Δ and ψ can be found in [2.1]

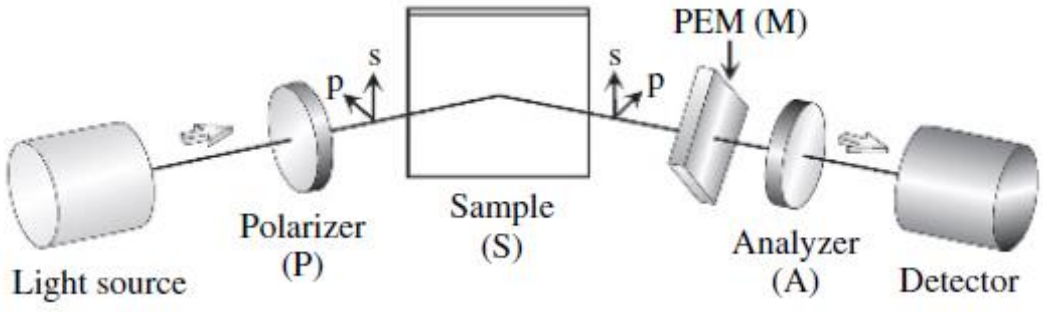

Fig. 6. Modulating ellipsometer with no rotating components [23]

To find out if the Horiba and Woollam ellipsometers gave similar results, the measurements on a calibrations sample were compared. Results are summarized in appendix VIII.

Variable angle VVASE Woollam ellipsometer (New Mexico State University)

This is a scanning monochromator rotating analyzer ellipsometer. The spectral range of the VVASE at New Mexico State is 180 nm to 2500 nm. The used measurement range for this study is from 6eV to 0.5 eV (about 200 nm-2500 nm). The ellipsometer

has an auto retarder to change the phase of the incident light from the light source. The auto retarder is an optical component that has anisotropic optical properties. The bandwidth of the Woollam VVASE depends on the slit width and can be varied by changing the slit width and is 2.3 nm/mm slit width. Typically for thin films, the monochromator in front of the detector is set at 4 nm spectral bandwidth.

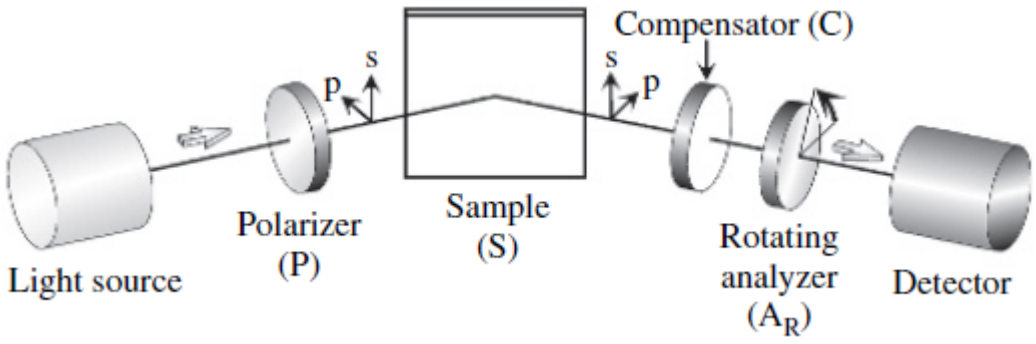

Fig. 7. Rotating analyzer ellipsometer [23]

Variable angle Woollam FTIR ellipsometer (Sandia National Lab)

The Woollam FTIR ellipsometer is a rotating compensator ellipsometer. For details on the optics see Fig. 5. It has wire grid polarizers. The wire grid polarizer is used because of its high extinction ratios, high operating temperatures, and wide bandwidth range. A wire grid polarizer only transmits light linearly polarized perpendicular to the wires. The light polarized parallel to the wires is reflected The IRVASE can perform accurate measurements from the near infrared (1.7 μm) to the far infrared (30 μm). Its spectral resolution can be varied from 1 cm^{-1} to 64 cm^{-1} depending on the measurement settings. The FTIR source has a Michelson interferometer instead of the monochromator. The interferometer (see Fig. 8.)

includes a beam splitter, a fixed mirror, and a mirror that can be moved (scan mirror). The beam splitter transmits half of the light and reflects the other half. The light from the source will be separated by the beam splitter to two different arms of the interferometer. One beam can go through the beam splitter and reach the fixed mirror while the other beam is reflected towards the moving mirror. Then the mirrors reflect the light back to the beam splitter where they are combined. The moving mirror introduces a phase shift between both beams and causes the interferogram. Because of the changing distance of the scan mirror, the wavelengths that are enhanced depend on the scan mirror's position. The intensity of the light reflected from the sample is measured by the detector for different positions of the scan mirror. This interferograph can be converted into a spectrum [24].

The Woollam FTIR ellipsometer has an ABB Bomem FTLA2000 light source with a silicon carbide glow bar that has a spectral range from 200 cm^{-1} to 5900 cm^{-1}. It also has a DTGS detector which has a measurement range from 200 cm^{-1} to 7000 cm^{-1}.

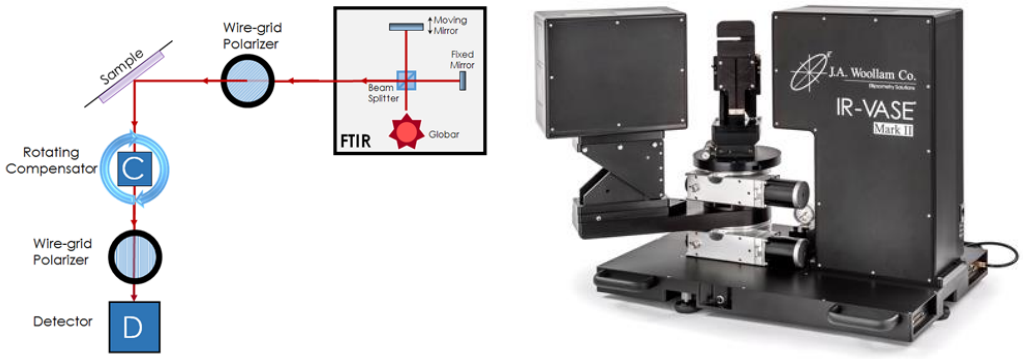

Fig. 8. Woollam FTIR ellipsometer [22]

2.1.3 Sample holder stage

The Woollam ellipsometers have a variable angle of incidence. To align the sample the sample holder stage can move in the z-direction (sample normal) and can also be tilted by two knobs to orient the sample. Knobs are adjusted until sample normal, incident and reflected beam all lay in the same plane. The Horiba ellipsometer has a fixed angle of incidence. To adjust the beam alignment in this instrument for samples of different thickness, one can only move the sample holder stage in the z-direction. Somehow a small paper is needed for all ellipsometers to find the detected point as where the light will hit the sample.

2.1.4 Software and model

All ellipsometers have an extensive software package to analyze the measurement data. The data files of the Woollam ellipsometers and the Horiba ellipsometer are in a proprietary format which will prevent to analyze data measured by one instrument to be analyzed by the other.

To describe the measurement results two different dispersion models were used. The Lorentz model was used to describe the optical properties in the infrared of the PyO and the SiO_2 substrate material. It assumes that the atoms, i.e. the positive metal ions and the negative oxygen ions, behave as a classical spring-mass system. The ions are moved by the EM-wave and can excite optical phonon modes [25]. The Lorentz dispersion is given by:

$$\varepsilon(E) = \frac{A_p Br_p E_p}{E_p^2 - E^2 - iBr_p E}$$ [Equation 2.10]

Where A_p is the peak height, Br_p is the peak width, and E_p is the peak position.

To describe the optical properties of the PyO in the visible part of the spectrum the Lorentz model is no longer useful. The large masses of the ions make it difficult to absorb photons in the visible part of the spectrum. The interaction of the EM-wave in the visible part of the spectrum is mainly through the electrons that have a lower mass. The absorption is described by the band structure of the PyO. Electrons absorb certain photons and jump from occupied states in the valence band to unoccupied states in the conduction band. The Cody-Lorentz model is used to describe the effect of the band gap on the optical properties. The model describes the band gap edge of the material. In CompleteEase the model also contains an Urbach tail to describe the absorption below the bandgap caused by for example defects. Localized states at the top of the valence band or at the bottom of the conduction band are often involved in optical transitions. The expression below shows the model. The first expression for ε_2 is the Urbach tail while the 2nd expression is the actual Cody-Lorentz term. E_1 is chosen to make the dispersion continuous at E_{gn}+E_{tn}. The real part of the dielectric constant is calculated from the integral. L(E) is a Lorentz dispersion and G(E) is the Cody term. For $E>>E_{pn}$, the Cody term becomes 1 and the dispersion is Lorentzian. E_{gn} is the bandgap.

$\varepsilon_{n\_C-L} = \varepsilon_{n1} + i\varepsilon_{n2}$, where

$$\varepsilon_2(E) = \begin{cases} \frac{E_1}{E}\exp\left(\frac{(E - E_{gn} - E_{tn})}{E_{un}}\right); & 0 < E \le (E_{gn} + E_{tn}) \\ G(E)L(E) = \frac{(E - E_{gn})^2}{(E - E_{gn})^2 + E_{pn}^{\ 2}} \cdot \frac{A_n E_{on} \Gamma_n E}{\left[(E^2 - E_{on}^2)^2 + \Gamma_n^{\ 2} E^2\right]}; & E > (E_{gn} + E_{tn}) \end{cases}$$

$$E_1 = (E_{gn} + E_{tn}) G(E_{gn} + E_{tn}) L(E_{gn} + E_{tn})$$

and

$$\varepsilon_{n1} = \frac{2}{\pi} P \int_0^\infty \frac{\xi \varepsilon_{n2}(\xi)}{\xi^2 - E^2} d\xi$$ (This is an integral in two parts*. See Ferlauto *et al*[2])

[Equation 2.11]

Where: A is the oscillator strength related to the probability for the transition, B is the broadening parameter, E_g is the bandgap, E_p is the Cody to Lorentz transition energy, E_t and E_u define the Urbach tail, an E_o is choosen so the ε_2 dispersion is continuous at E_g+E_t.

The Cody-Lorentz model was used to model the dispersion in the NIR/VIS/UV part of the spectrum for fits of the optical measurement in this thesis. A quantum mechanical derivation of the dielectric constant for a system with parabolic bands and direct interband transitions shows a Lorentzian dispersion [25]. The Cody-Lorentz model is often used for amorphous materials or for materials with a lot of defects.

2.2 Sputter Deposition System

This section contains a description of the deposition system used to make the PyO films and the device wafers.

2.2.1 Vacuum system

A high vacuum environment is needed during the deposition to get a pure film on the

surface of the substrate. A high vacuum pump usually needs a certain vacuum on its outlet to maintain the pressure difference between entrance and exit of the pump within the working range. So usually a high vacuum system requires more than one pump. Furthermore, the pump efficiency of various pumps depends on the pressure in the chamber and the type of pump. The AJA main chamber's pumping system, therefore, consists of two vacuum pumps, a roughing pump to pump down the chamber from atmospheric pressure to low vacuum (10^{-3} Torr range) and a high vacuum pump to pump down the chamber from the low vacuum to the high vacuum range (10^{-7} Torr range). The roughing pump is also used to make sure the outlet of the high vacuum pump will stay at low vacuum. The high vacuum pump of the AJA sputtering system is a turbo pump. An example is shown in Fig. 9 on the left. A turbo pump has many turbine blades and stator blades. The pump moves the gas from the entrance to the exit by the impulse exerted on the gas molecules by the high speed rotating turbine blades and stationary, static blades. The speed of the rotating parts of the turbo pump is on the order of 10^4 rpm. So a turbo pump can pump down the chamber by physically changing the momentum vectors of the remaining gas molecules. The roughing pump in the system is a multistage roots pump as shown in Fig. 9 middle and right. The roots pump mechanism is based on two synchronized rotors that are rotating in opposite directions.

Specifics on the pumps in the AJA system are discussed in this section. Three pumps are included in the AJA sputtering system. One turbo pump is directly connected to the main chamber. Another turbo pump is connected to the load-lock. The main

chamber is connected to a TMP-803LM pump which has a maximum pumping speed of 700 liters/min (35000 rpm and 5 mins of start-up time). It can reach pressures as low as 10^{-8} Torr. The load-lock is furnished with a TMH 071P pump that has a maximum speed of 90000 rpm and can get to pressure as low as 10^{-7} Torr. The other one is the ACP multistage roots pump that can get to pressure as low as 10^{-2} Torr as the roughing pump connecting to the turbo pump from the main chamber. All three pumps are controlled by the control pad and can automatically start or stop when the main power switch is toggled on or off. There is a throttle system in between the main chamber and the turbo pump to control the pressure in the chamber during the sputtering process. This throttle system can be opened and closed by the computer to reduce the effective pumping opening between chamber and turbo pump with 40% and reduces the pumping speed of the turbo pump during sputtering resulting in higher pressures during the sputtering process.

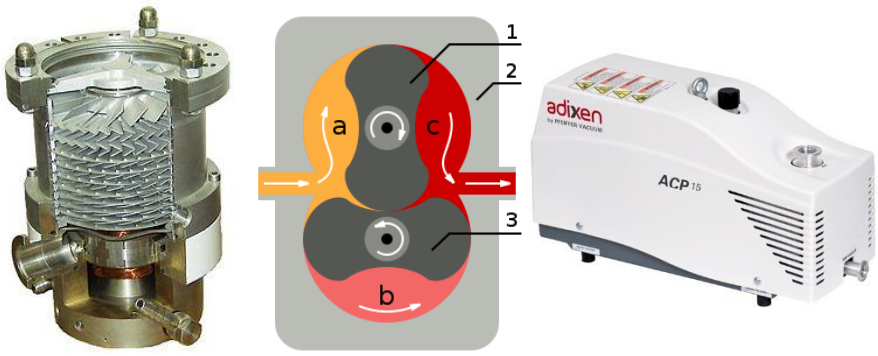

Fig. 9. Trubo pump (left), roots pump (middle), and ACP multistage roots pump (right)

2.2.2 Load-lock

The AJA deposition system has a load-lock for faster sample loading. It is between the computer/control pad and the main chamber. The load-lock that can be opened

on the top includes a pressure gauge, a sample holder for a full 4 inch wafer, a translation rod, and a high pressure vacuum valve. The pressure gauge in the load-lock is used to determine when the pressure is equalized between the load-lock and the main chamber, and one can open the valve between the main chamber and the load-lock or open the load-lock to load a new sample. So the gauge needs to have a large measurement range from atmosphere to as low as 10^{-7} to 10^{-8} Torr. It is a Televac CC-10 wide range gauge with two different sensors. The pressure in the load-lock is measured with a thermocouple sensor from atmospheric pressure to 10^{-4} Torr and with a double inverted magnetron cold cathode sensor from 10^{-2} to 10^{-9} Torr. The translation stick used to move the sample holder from the load-lock into the main chamber uses a mechanical feed through that is based on permanent magnets. Magnets outside the vacuum chamber move magnets inside the vacuum chamber, so no vacuum seal is required. The high pressure valve towards the main chamber is always closed except during the sample transfer process. The load-lock can only open if the pressure difference between the main chamber and the load-lock is smaller than a factor 10. The load-lock makes the deposition process mush faster as it cuts down considerably on pumping time. The pump down time for the load-lock is 10 minutes compared to several hours for the pump down time of the main vacuum chamber.

2.2.3 Heating lamp and temperature monitor of sample holder

The AJA system is furnished with an SHQ400 SERIES SUBSTRATE HEATER to heat the

sample during deposition. The heater includes a halogen lamp, a temperature gauge, and a quartz glass cover plane. The light of the halogen lamp directly illuminates the sample holder raising its temperature. The lamp in the main chamber is on the back of the sample holder on the top and covered by a quartz glass cover plane. The temperature can get as high as 850^{o}C. The temperature is measured with a thermocouple that is shielded from the direct radiation by an inconel and ceramic sleeve. The thermocouple does not directly touch the fused quartz cover plate and measures the temperature via radiation. The measured temperature was corrected for by a temperature offset curve provided by AJA. The temperature offset correction depends on the set temperature. It was small at 600^{o}C but much larger at low temperatures, i.e. +91^{o}C at 200^{o}C. The corrected substrate temperature can be found in Table 1. A temperature controller, i.e. an SHQ15 A, 25 A heater controller, is used to control the substrate temperature during the deposition via a control pad on the top right of the instrument panel. It can also be controlled by the computer. The temperature of the substrate can be ramped up fast. If fast temperature ramps are used, some of the glass substrates will break because of large thermal stress induced by the heating process. In this study, a 1min delay at every 50^{o}C temperature raise is safe enough to prevent the glass substrate from cracking. This delay time needs to be set manually on the computer. The sample's real temperature could be quite different from the value indicated by the measurement gauge, especially when fast temperature ramps are used because of the thermal time constant of the sample holder. Since the sample holder cannot be actively cooled it may take several hours

to let the sample cool down in the main chamber from high temperature. For the temperature series samples, the substrate heater was switched off immediately after the deposition was finished. The time it took for the 588^{o}C and 513^{o}C samples to cool down below 400^{o}C is estimated to be 5 and 2 minutes. This time is relevant as others have reported that NiO partly reduces to Ni above 400^{o}C in a vacuum. [6]

Table 1. Measured and Actual temperature of AJA sample holder

AJA substrate heater	
measured T (K)	actual T (K)
50	83
100	166
150	237
200	291
250	330
300	366
350	400
400	433
450	475
500	513
600	588
650	634

2.2.4 Pressure monitor and gauge in the main chamber

There are three gauges in the main chamber to monitor the pressure inside the chamber. An MKS capacitance manometer, a GP convectron gauge, and a GP hot ionization gauge. The three gauges have each a different measurement range. The capacitance manometer that is shown in Fig. 4 on the left includes a diaphragm, an electrode assembly, and capacitors. The pressure difference can change the

capacitance of the capacitors. The change is measured and depends on the pressure. The capacitance manometer measures the real pressure and is not sensitive to the type of the gas. But the capacitance manometer cannot measure a high vacuum: the measurement results are not reliable below approximately 10^{-2} Torr. The convectron gauge shown in the middle of Fig. 10 has a gold plated tungsten sensing wire and measures the pressure by the convection currents. The convectron gauge can measure as low as in the 10^{-4} Torr range, but its readings are sensitive to the type of gas in the chamber. It is calibrated for N_2 gas. The real pressure for Ar is a factor 1.4 larger than the indicated value. All pressure values listed in this thesis are uncorrected values. The GP hot ionization gauge in the system can cover the very high vacuum range. A hot ionization gauge, as shown in Fig. 10 on the right includes a filament, a cylindrical grid, and an ion collector. The heated filament can release electrons which can be collected by the cylindrical grid that has a positive potential. The escaped electrons ionize the gas creating a plasma. The density of the plasma depends on the density of the gas in the chamber which is proportional to the pressure. So the measured current is proportional to the pressure. The hot ionization gauge has a large measurement range on the very low pressure side (10^{-9} to 10^{-11} Torr) but cannot work in the high pressure range. Above a pressure of about 10^{-4} Torr, the filament in the gauge might burn out in particularly when high concentrations of oxygen are present in the chamber. To prevent damage, the gauge needs to be switched off during deposition or during the venting process.

To control the gas flow two MKS Type M100B/M10MB Mass-Flo Controller were

used. The mass flow controller for argon has a range of 0-100 sccm and the mass flow controller for oxygen has a range of 0-20 sccm. The control range is from 2% to 100% of the full scale of the controller. The accuracy of the flow is 1% of the full scale. The mass flow controller is used to keep a certain flow rate of O_2 and Ar that is used to make the PyO film in the main chamber during deposition. Details on the parameters of the mass flow controllers are given in Table 2. No attempt was made to zero the offsets of the mass flow controller prior to deposition.

Table 2. The mass flow controller of the deposition equipment in the cleanroom

mass flow controller	MKS Type M100B/M10MB Mass-Flow Controller
Ar range	0-100 sccm
O_2 range	0-20 sccm
Minimum scale set	2% to 100% of the scale
Accuracy	1% of the full scale

Fig. 10. MKS capacitance manometer gauge (left) [26], GP convectron gauge (middle), and GP hot ionization gauge (right)

Fig. 11. AJA system in the cleanroom of Tx state

2.2.5 Thickness monitor

The thickness monitor in the main chamber is used to measure the deposition rate for different targets and sputter parameters. A MODEL TM-350/400 quartz crystal thickness monitor is included in the equipment with the quartz crystal detector on the top of the vacuum chamber and a controller on the bottom of the control pad. The crystal thickness monitor can be moved into the sputtering beam to a position just under the sample holder. The quartz crystal has a certain oscillating frequency which depends on the total thickness of the film deposited on the monitor. The monitor measures the thickness as well as deposition rate from the change of the oscillation frequency of the quartz crystal. To calibrate the instrument, two parameters are to be entered into the monitor, the density and the impedance of the

material to be sputtered. The change of frequency is described by the equation below [27]:

$$-\nabla f = C\rho d$$

$$C = \frac{Af^2}{A_q N \rho_q} \qquad \text{[Equation 2.9]}$$

ρ ---density of the coated region of the quartz crystal in g/cm^3

ρ_q ---density of quartz crystal in g/cm^3

d ---thickness of the coated region of the quartz crystal in cm

A ---area of the coated region of the quartz crystal in cm^2

A_q ---area of the quartz crystal in cm^2

f ---frequency constant of the quartz crystal in Hz

N ---spring constant of the quartz crystal

The equation above can only calculate the mass increase of the crystal if it is less than 10%. The acoustic impedance is needed to calculate the rates if the quartz crystal‘s mass changes with more than 10%. Including the effect of the acoustic impedance ratio, the thickness can be calculated from:

$$\mathrm{d} = \left(\frac{\rho_q}{\rho_f}\right) N_q \left(\frac{\tau}{\pi R_z}\right) \arctan\left(R_z tan\pi \left(\frac{\tau - \tau_q}{\tau}\right)\right) \qquad \text{[Equation 2.10]}$$

N_q ---Frequency constant for an “AT” cut quartz crystal vibrating in thickness shear

R_z ---the acoustic impedance ratio

ρ ---density of the coated region of the quartz crystal in cm^3

ρ_q ---density of quartz crystal in cm^3

ρ_f ---density of film in cm^3

d ---thickness of the coated region of the quartz crystal in cm

τ ---period of loaded crystal in s

τ_q ---period of uncoated crystal in s

The quartz crystal thickness monitor can be inserted under the sample holder by rotating a mechanical knob connected to a feed-through on the top of the chamber. It is moved to the side during the deposition on the sample. The quartz crystal thickness monitor can block the sample so the deposition rate or thickness cannot be measured during the real deposition. A test layer or deposition run is needed before the deposition rate or thickness can be determined. The quartz crystal thickness monitor can measure deposition rates as low as 0.1 Å/s. The following values were used to monitor the rate of PyO, z=18.65, and ρ=7 g/cm^3.

2.2.6 Sputter process

There are three DC sputter guns and two RF sputter guns included in the system. In this study, an RF gun was used to form the NiFe-oxide layer. The use of an RF gun with an alternating switching voltage can avoid charging effects of the target surface during the reactive deposition process. An MDX sparcle20 power supply and a sparcle20 accessory were available for arc repression during dc magnetron sputtering. The applied voltage accelerates the Ar ions in the plasma. These ions attack the target and physically remove target atoms by momentum transfer. Removed target atoms will move towards the substrate positioned at the top of the main chamber: the substrate is covered with a thin layer. The Fe-doped NiO films were made by reactive RF sputtering from a NiFe target. Although the NiFe target is a

metal, oxygen present in the chamber during the sputtering process will oxidize the top of the target, resulting in an insulating layer on top of the target. So it is not possible using a DC power supply that has the maximum power about 400 watt as this would result in a charged target with strongly reduced sputter yields. To further increase the sputter yield a magnetron sputter gun was used. Permanent magnets under the target material create a magnetic field just above the target increasing the path length of the electrons in the plasma, increasing their ionization efficiency.

2.2.7 Deposition procedure

The details of the deposition procedure and a specific recipe on the followed procedures to vent, to load, to unload and to pump down the chamber can be found in appendix I.

2.3 Other equipment that was used in this study

2.3.1 Four-point probe measurement system.

A 4-point probe usually called 4pp is a simple method to measure high resistivity samples. To measure the semiconductor samples presented in this thesis, the linear 4-point probe station was used. It consists of 4 electrodes positioned in a line each separated by 1mm from each other. The outer electrodes are connected to a current source, and the inner electrodes are connected to a voltmeter. The 4-point probe technique will avoid the contact resistance between the electrodes and the sample to show up in the measurement results. The used voltmeter has a very large input

resistance. This large input resistance assures that no current will flow through the inner electrodes. Although a contact resistance is present between the electrodes and the sample, no voltage drop across the contacts is present as the current through the meter and electrodes is zero. A sheet resistance can be calculated from the measured I and V using the following equations [28]:

$$\rho = \frac{\pi V}{\ln(2) I}$$

$$\frac{\pi}{\ln(2)} = 4.53 \qquad \text{[Equation 2.11]}$$

The electrical characterization station with 4pp was used in the study. The station includes a Keithley-6514 electrometer, a Keithley-2182 nanovoltmeter, a Keithley-7001 switching box (includes Keithley-7065 Hall card), and a Keithley-6221 current source. As shown in Fig. 12 the system is controlled by a computer using a Labview program.

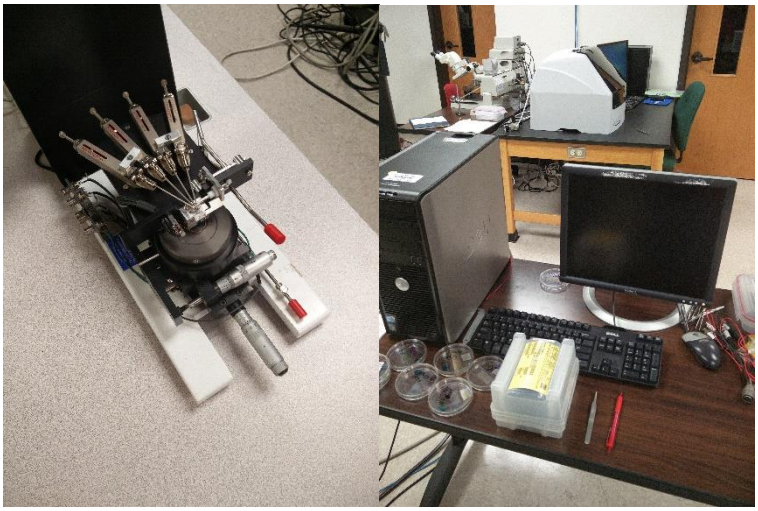

Fig. 12. 4pp electrical characterization station

2.3.2 Electron microscope and EDAX

An FEI Helios Nano Lab 400 scanning electron microscope was used to analyze the morphology and chemical composition of our samples. Fig. 13 left shows a diagram of a scanning electron microscope. The electron beam is created by an electron gun positioned at the top of the instrument. Its path and diameter are modified by different electromagnetic lenses and a spray aperture and focused into a narrow beam with a diameter of 1.4 nm. The focused electron beam is scanned across the surface of the sample and information on the morphology or chemical composition of the sample is collected by various detectors. The electron beam can interact with the atoms of the sample and generate secondary electrons, back scattered electrons and X-rays. When monitoring the elastically back scattered electrons as a function of the beam incident position, a picture of the morphology of the sample is obtained. The FEI Helios Nano Lab 400 is a fully digital Field Emission Scanning Electron Microscope (FE-SEM) that is shown at the bottom of Fig. 13. At an optimal working distance (15 kV) the ultra-high resolution electron optics can get to 0.9 nm resolution. The sample can be moved on a 5-axis x-y-z-rotate-tilt stage with piezo control. It has a 100 mm range with the x and y-axis and -10 to +60 degrees on tilt. The movement range of the z-range is 20 mm. Stage repeatability in x and y directions is 0.5 µm, at 0° and 52° tilt with less than 8 nm drift per minute at a tilt. The retractable STEM Detector has a 0.8 nm resolution on bright field, dark field, and high-angle dark field modes. The FEI Helios Nano Lab 400 has a retractable vCD-High sensitivity, solid-state back scattered detector to collect the back scattered electrons.

The incident electron beam can also generate X-rays. As the X-ray that are generated from different atoms have different energies, the measured energy spectrum of the X-ray tells us something about the chemical composition of the sample under the electron beam. The Energy-dispersive X-ray spectroscopy (EDAX) mode will measure the energy spectrum of the X-rays and calculate from the measured spectrum the concentration of atoms in the sample. The system assumes that the sample is bulk, so has a homogeneous composition. To measure the x-ray, the system has a 30mm^2 Silicon Drift Detector (EDAX Apollo XL). This detector has a wide solid acceptance angle and an ultrathin polymer. This detector shows very good resolution at low energy and excellent sensitivity for the detection of the low energy peaks for example the oxygen peak in SiO_2 [29]. As this window cannot be plasma cleaned the detector can be retracted during plasma cleaning of the SEM chamber. An example of an EDAX spectrum of a PELLA fused-quartz substrate measured in our SEM is given in Fig. 14. The ratio of the oxygen to silicon peak is a little larger than one would expect for fused quartz. This show that our SEM sensitivity for oxygen is high.

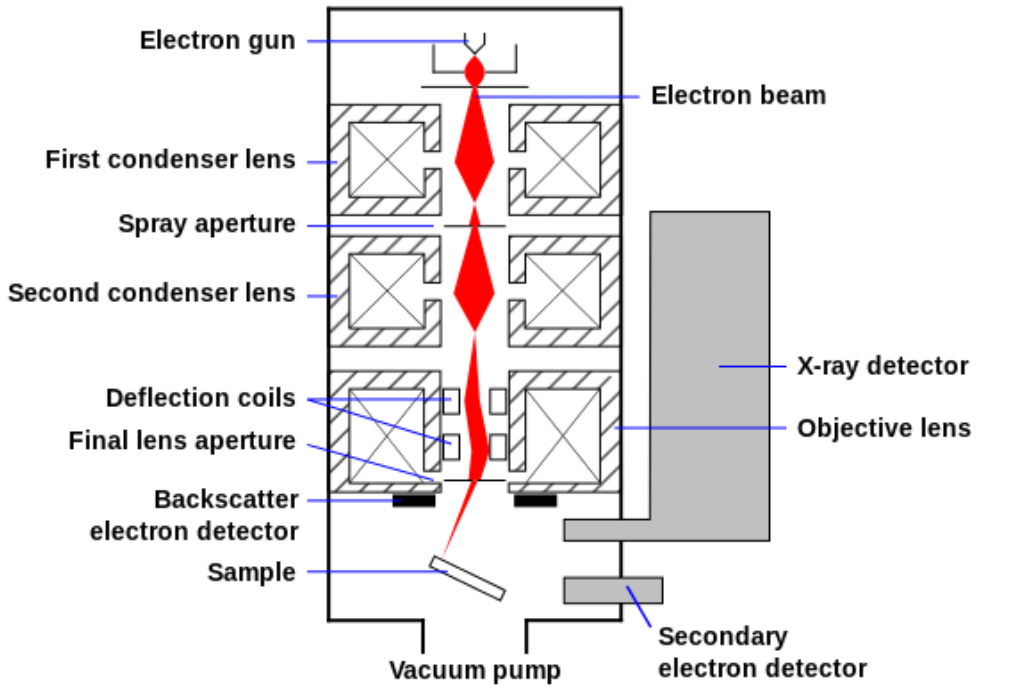

Fig. 13. Scanning electron microscope with different parts (top) [30], FEI Helios Nano Lab 400 SEM of Tx state (bottom)

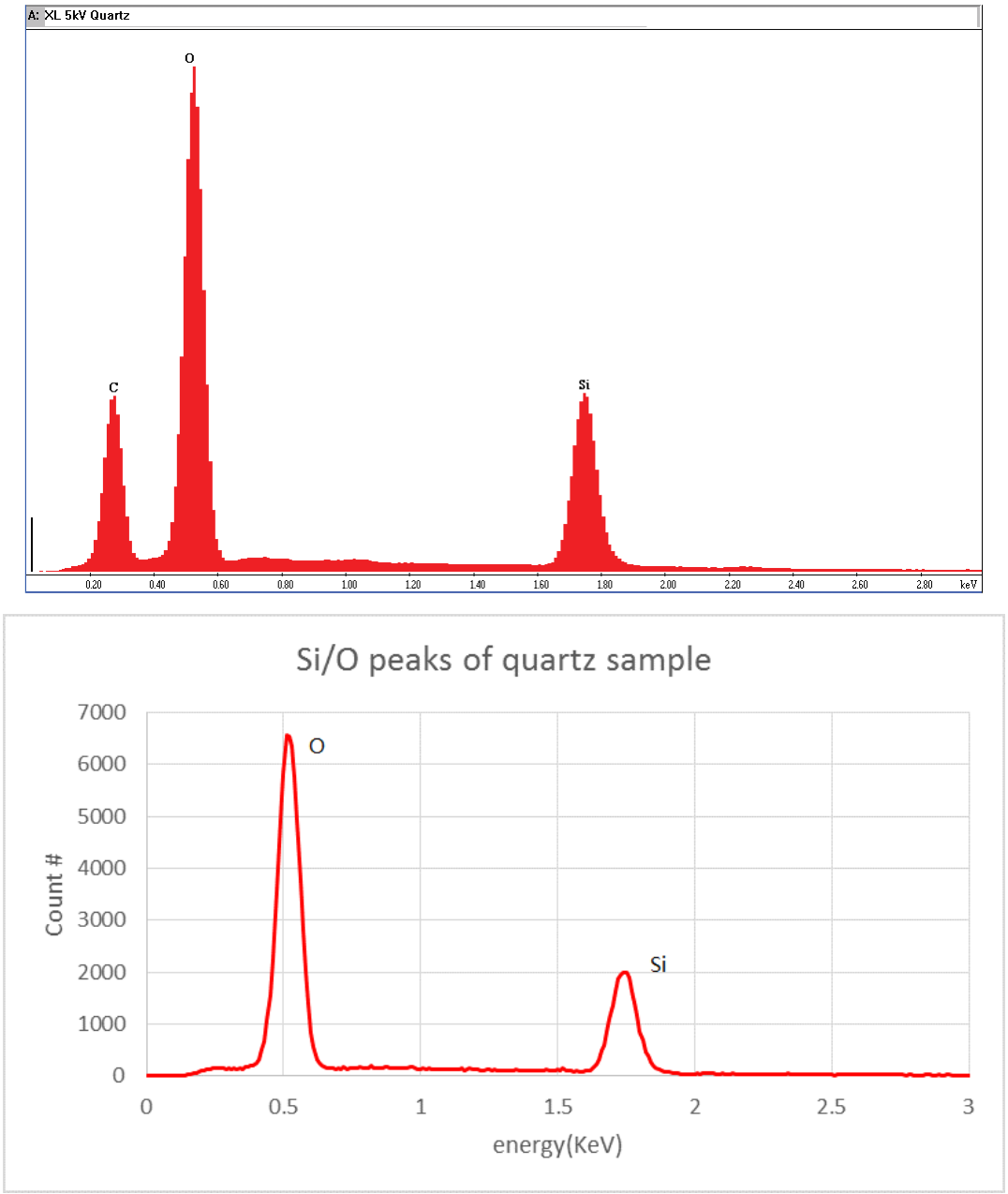

Fig. 14. Calibration measurement done by Edax Inc. (top)[29] and EDAX measurement result on quartz sample done at Tx state

Atomic Force Microscope

The surface of the samples in this thesis were also studied by atomic force microscopy (AFM). The AFM includes a laser source, a narrow tip, and a detector as shown in Fig. 15. The AFM has an oscillating cantilever that vibrates with an amplitude of 20 nm to 100 nm (with a frequency of about 170 Hz). The tip is slightly

tapping on the surface of the sample at the lowest point of the oscillation. The AFM head measures the vibration of a tip from the reflection of the laser beam from the back of the narrow tip using a four quadrant detector. The movement of the tip depends on the force between the small pin of the tip and the sample surface when they are very close. It measures the local height of the surface at the position of the tip. The tip of the AFM is usually as small as several nm.

A Veeco Dimension 3100 SPM/ AFM System was used. The equipment has a xy scanning range of 90µm and z-axis range of 6µm. The equipment was used to measure the sample surface in an area as large as 5µm * 5µm. The NSC14/AL BS tip is used in the study. The tip is made of n-type silicon and has an 8 nm probe radius that has a 40 degree top angle. The frequency is about 160 Hz. The operating step for the measurement can be found in Appendix II

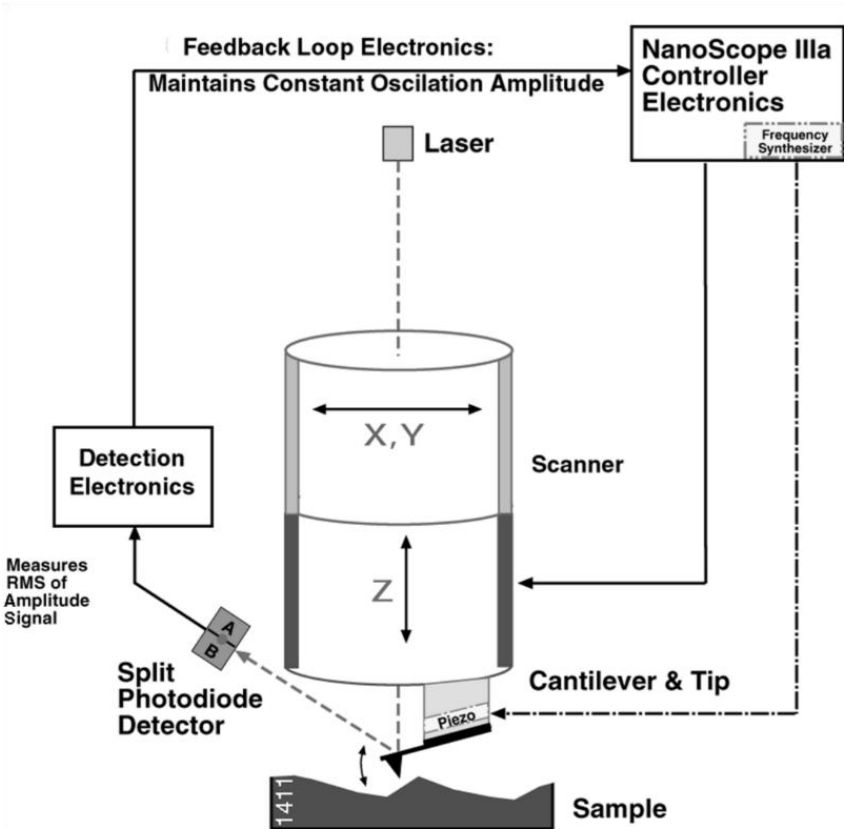

Fig. 15. Veeco Dimension 3100 AFM

III. TEMPERATURE SERIES

3.1 Introduction

Others have shown that dual ion beam sputtered PyO has the rocksalt structure [10]. According to the NiFe-oxide phase diagram [31], the maximum solubility of Fe in the rocksalt structure in air at room temperature is not more than 2 %, so sputtered PyO might be meta-stable. The crystal structure was studied by X-ray powder diffraction [32] but will not be discussed in this thesis. The X-ray measurement showed that also our RF-sputtered films have a rocksalt crystal structure. It is believed that the crystal structure is important as the rocksalt structure of both NiO and FeO can be made to be non-stochiometric. The oxygen atomic concentration of both materials depends on the deposition parameters. As RRAM is based on reversible switching from a metallic to a semiconducting state this is an important property of the RRAM memory material. The research of this chapter was done to verify the crystal structure of our RF sputtered PyO films. A Temperature series was made to determine the optical properties of the PyO layer formed under different substrate deposition temperatures. The deposition temperature was varied from room temperature to 588^{o}C. As sputter gas, a mixture containing 20% of O_2 and 80% of Ar was used. The percentage was set using the mass flow controllers. The total gas flow during deposition was kept at 10 SCCM. FTIR measurements were performed to verify the rocksalt crystal structure of the RF sputtered films. In addition, ellipsometric measurements were done in the visible part of the spectrum to determine the film thickness and optical properties.

3.2 Substrate Preparation and Deposition.

Substrate Preparation.

Two temperature series were made. The films of the first temperature series were deposited on Si/SiO_2 substrates and 3” glass wafers. Another temperature series was made because after about 2 to 3 months cracks were found on the PyO samples on the large glass substrates. The cracks are believed to originate from stress in the samples possibly due to the different rate of thermal expansion between the PyO film and the substrate. Especially with the big size of the 3” glass wafers, stress could be significant. The 2^{nd} temperature series was deposited on 2 square inch Si/SiO_2 substrates and 1 square inch fused quartz substrates purchased from Pella.

All the samples were prepared with the same cleaning procedure. Water, acetone, and Isopropyl alcohol were used in a sonicator for each 5 mins after which the samples were dried using a spinner. In addition, the substrates were also cleaned and dried again in the cleanroom before deposition. This time acetone, Isopropyl alcohol, and the ultra-clean nitrogen gas gun were used to do the cleaning.

For ellipsometer measurements, a rough backside surface is needed to prevent polarized reflections from the back surface of the substrate. As the 3” glass wafers were flat on both sides, they were measured in the ellipsometer with a scotch tape on the back of the substrate. This technique is known to give reasonable results in the visible part of the spectrum for glass substrates. The technique fails for substrates with a larger refraction coefficient such as sapphire, and it is not known

whether the scotch tape trick works in the infrared. To avoid any issues, a bead-blaster was used to roughen the back of the substrates used to make the second temperature series. The front side was covered by printer paper and painter tape to keep it clean from the bead-blaster. Several samples broke with the bead-blaster gun at perpendicular incidence to the sample. Better results were obtained by directing the gun at 45 degree angle to the sample normal and holding it at approximately 1 meter distance from the gun. The roughing time was 10s for a quartz substrate and 30s for a Si/SiO_2 substrate. It was long enough to get a high quality rough back surface suitable for optical characterization.

Fig. 16. Bead-blaster of the engineering technology department used for our experiments

The quality of the substrates and cleaning procedures was verified by ellipsometry at New Mexico State University

Fig. 17a shows the Δ and the Ψ spectra of the quartz substrate cleaned according to the standard cleaning process described above. These spectra are typical for a

dielectric material with a low refraction index. Note that Ψ becomes extremely small (less than 2°) near the Brewster angle which will lead to systematic errors when calculating the optical properties: near the Brewster angle r_p is going to be close to zero and also Ψ is around zero (see equation 2.4 in Chapter 2). Note the large systematic error in the pseudo dielectric constants calculated from the data measured at 55 degrees angle of incidence. Furthermore, note also that Δ changes sign when the angle of incidence goes through the Brewster angle.

Fig. 17b shows the real ($<\varepsilon_1>$) and imaginary ($<\varepsilon_2>$) part of the pseudo-dielectric constant of the quartz substrates exposed to different cleaning procedures. The first two graphs show the measurements on a substrate cleaned with water, acetone, and IPA (see chapter 2). We refer to this cleaning method as a normal clean. The last two graphs show similar results on a substrate that was also exposed to an oxygen plasma clean (Tx state) or an ozone clean (NMSU). The $<\varepsilon_1>$ is similar for substrates exposed to different cleaning method. Its dispersion looks as expected for a glass with normal dispersion. $<\varepsilon_2>$ seems to depend on the cleaning method. The data are not accurate for an angle of incidence of 55° because Ψ is too small at this angle of incidence (see discussion above). Even if we ignore the data taken near the Brewster angle, one can see that $<\varepsilon_2>$ is negative. This suggests the presence of a thin film with a higher refractive index than the glass on the surface of the substrates. The UV value of $<\varepsilon_2>$ is cut in half by the plasma and ozone clean which shows that those cleans should be incorporated in the substrate preparation process in future studies. The plasma clean is as good as the ozone clean to make a good condition of the surface

of the sample. Both are better than the normal clean.

a

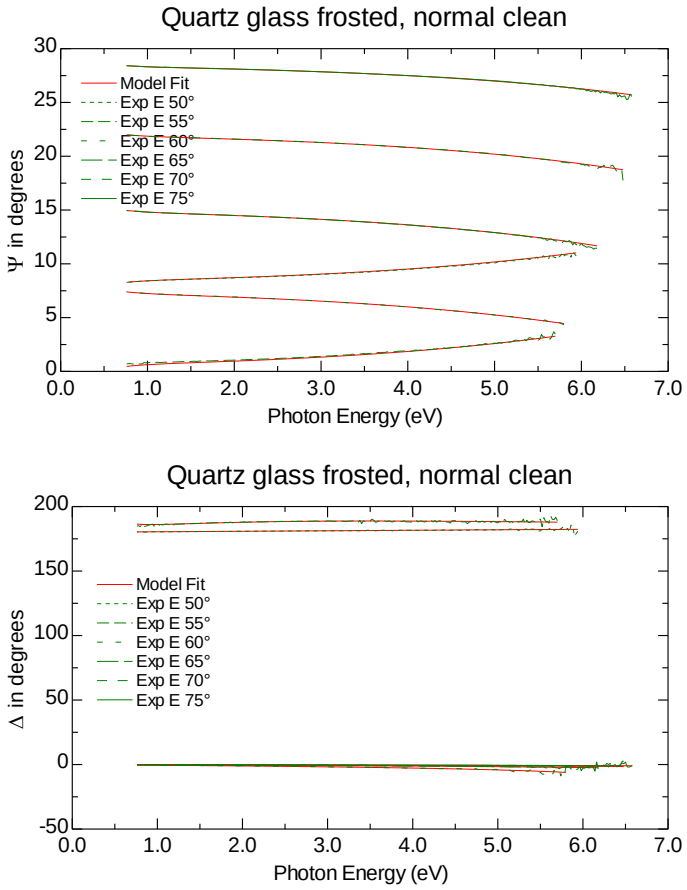

b

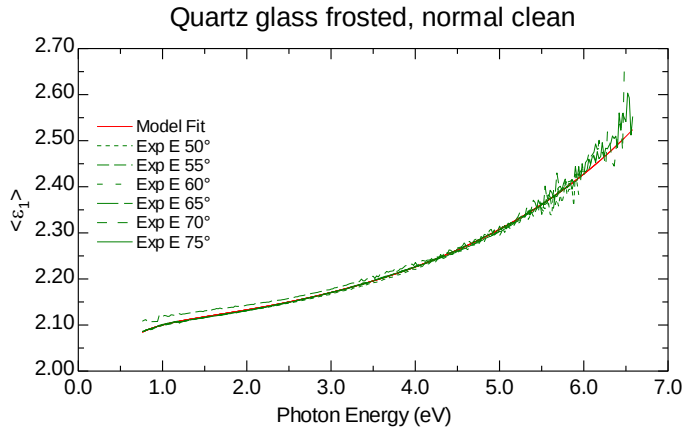

Fig. 17. Ellipsometry measurements of the Pella quartz substrates; (a)psi and delta as a function of the wavelength for different angles of incidence; (b)pseudo dielectric function of standard cleaned sample

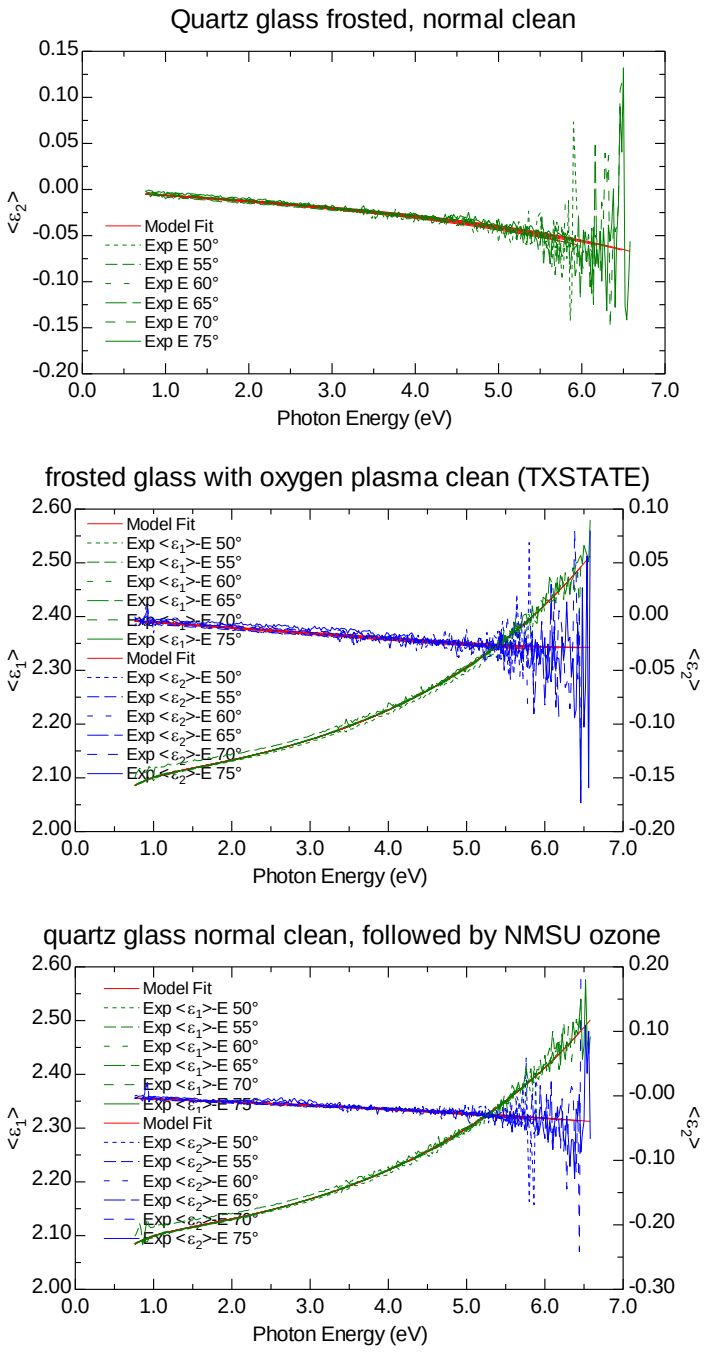

Fig. 17. Continued

Deposition of PyO

The AJA deposition system located in the cleanroom was used to make the thin PyO films. For more details on the system see chapter 2. The deposition parameters are summarized in Table 3.1 provided below including the list with the substrate

material, the sputtering time, the deposition tempe

rature, and the thickness of the PyO determined from ellipsometry measurements.

Table 3. Deposition parameters of temperature series

Ar flow rate	8 sccm
O_2 flow rate	2 sccm
Setpoints Substrate Temperatures for the 1st series	11°C, 100°C, 200°C, 300°C, 600°C
Actual Substrate Temperatures for the 1st series	11°C, 166°C, 291°C, 366°C, 588°C
Setpoint Substrate Temperatures for the 2nd series	24°C, 100°C, 250°C, 300°C, 400°C 600°C
Actual Substrate Temperatures for the 2nd series	24°C, 166°C, 330°C, 366°C, 433°C, 588°C
Substrate for the first series	Glass wafer, Si/SiO_2, Si/SiO_2/Si_3N_4, Si/SiO_2/Al
Substrate for the second series	Pella Quartz, Si/SiO_2
RF-Power	240 Watt
Background pressure	10^{-7} Torr
Pressure during deposition	10^{-3} Torr
Rotation of substrate holder	30 rpm
Target distance	215 mm
Deposition time	600 s
Throttle	40%
Target Composition	$Ni_{0.81}Fe_{0.19}$

3.3 Ellipsometer measurement results in NIR/VIS/UV part of the spectrum.

The Δ and Ψ spectra were measured at five different angles of incidence from 250-1000 nm with the Woollam M2000 ellipsometer. In addition, the transmission spectra of the films on the glass wafers were measured with the same instrument. The ellipsometric spectra and the transmission spectra were used to determine the film thickness and the optical properties of the PyO films through the NIR/VIS/UV. The transmission data was only available for the PyO on the glass wafers because the substrates of the other series were roughened before deposition. The data analysis was done with the CompleteEase software. The following procedure was used:

1. The measured spectra were fitted using a Cody-Lorentz model.

2. Next, the results of the Cody-Lorentz fit was used as the starting value for a wavelength by wavelength fit.
3. Finally, the result of a wavelength by wavelength fit was used as the starting value of a b-spline fit.

The film thickness data is summarized in the table below.

Table 4. Thickness fitting on the big glass wafer sample

Substrate	Big glass wafer	
Temperature [°C]	thickness [A] [1]	MSE
11	818.9	19.3
166	806.2	18.9
291	755.2	17.4
366	803.9	18.7
588	586.3	15.1

Table 5. Thickness fit parameters of PyO on quartz and on Si/SiO_2

Substrate	temperature	Thickness (MSE)	Substrate	temperature	Thickness (MSE)
quartz	24°C	68.2 nm (3.1)	$SiSiO_2$	24°C	68.2 nm (3.0)
	166°C	68.4 nm (3.9)		100°C	66.9 nm (2.6)
	330°C	70.3 nm (3.4)		250°C	67.3 nm (3.4)
	366°C	68.7 nm (2.4)		400°C	68.9 nm (2.8)
	433°C,	66.4 nm (32.7)		500°C	66.1 nm (3.6)
	588°C	68.7 nm (3.4)		600°C	70.2 nm (3.5)

The ε_1 and ε_2 curve calculated this way for the PyO films on the glass wafers are shown in Fig. 18a. A large peak around 2-3eV was detected in the optical spectrum. This peak becomes larger for PyO films sputtered at higher temperatures. Gosh et al. found that single crystalline NiO reduces to Ni above 400°C in a vacuum, resulting a peak a little below 2 eV in the ε_2 spectrum [33]. Very recently Petersen et al. calculated the effect of oxygen vacancies on the optical properties of NiO and found

peaks at 2, 2.25, and 3.25 eV.[34] The results of Fig. 18a suggest that all PyO films have a significant amount of oxygen vacancies in them. The calculated spectra showed in Fig. 18a, however, are not consistent with the transmission spectra, though. Fig. 18b shows the calculated and measured transmission spectrum of the sample sputtered at a substrate setpoint of 200°C. The peak in the ε_2 spectrum near 2 eV causes a large difference between calculated and measured transmission spectrum. So this peak is not physical. Fig. 19 shows the results if one uses both the measured ellipsometric spectra and the measured transmission spectra to calculate the optical properties. The peak at 2 eV is still there although much smaller than for the spectrum of Fig. 18a.

The results for the Si/SiO_2/PyO temperature series is summarized in Fig. 20. Note that also for this sample only the ellipsometric data was used as transmission data was not available. A small peak is visible between 2-3 eV.

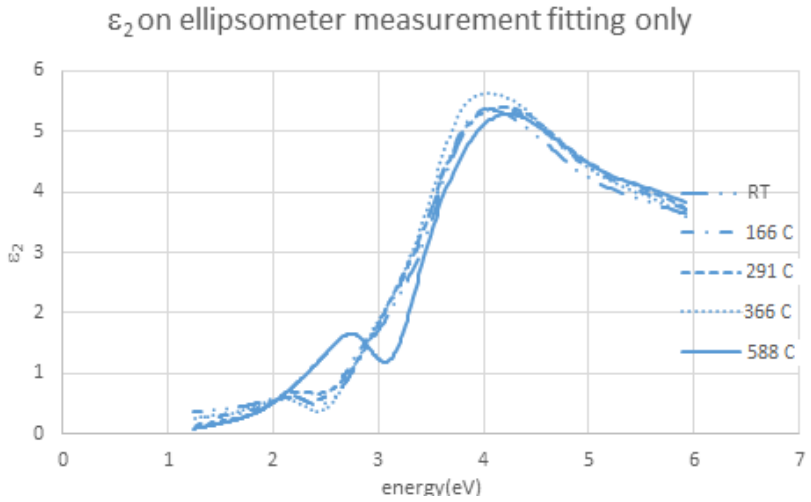

Fig. 18. (a) ε_1 and ε_2 as a function of the temperature for PyO sputtered on big glass wafer substrates (calculated from ellipsometry data only); (b) measured and calculated transmission spectrum of PyO sputtered at a temperature of 291°C

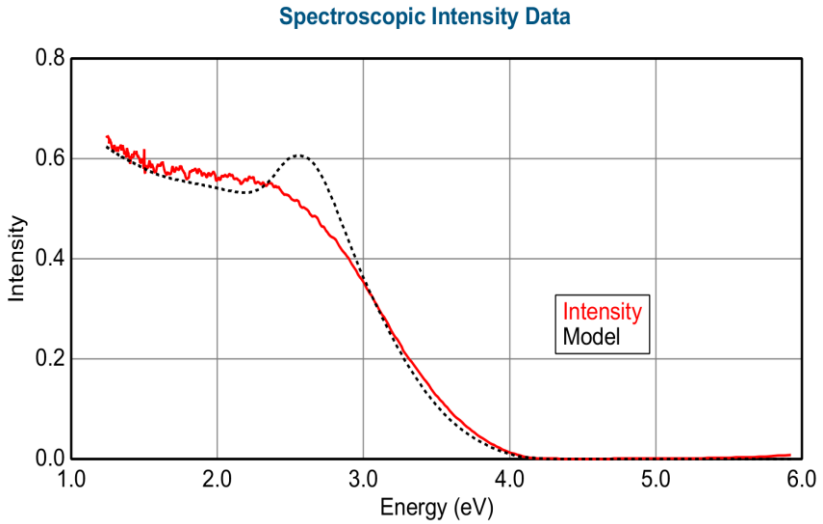

Fig. 18. Continued

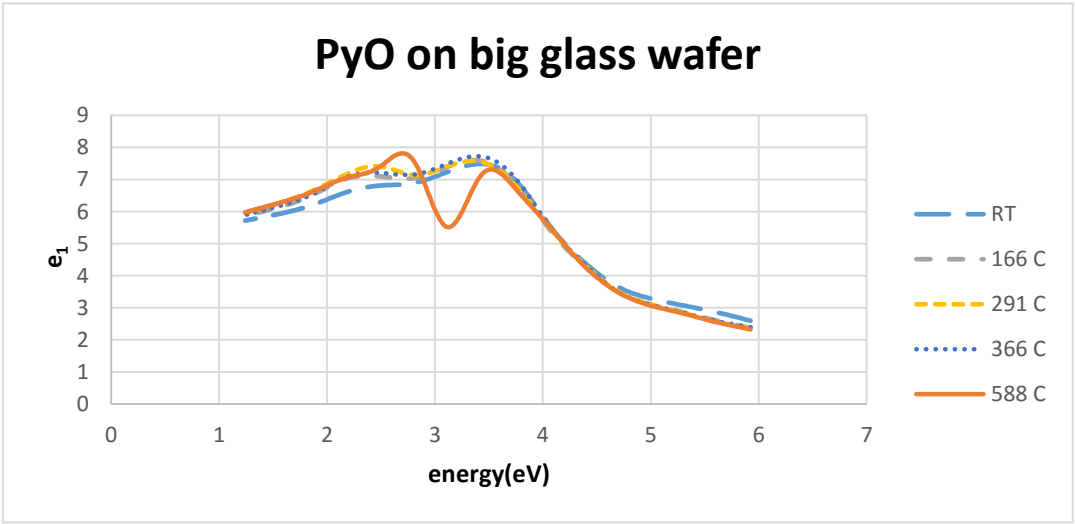

Fig. 19. ε_1 and ε_2 as a function of the deposition temperature for PyO on big glass wafer substrates (calculated from simultaneous fit of ellipsometry and transmission spectra)

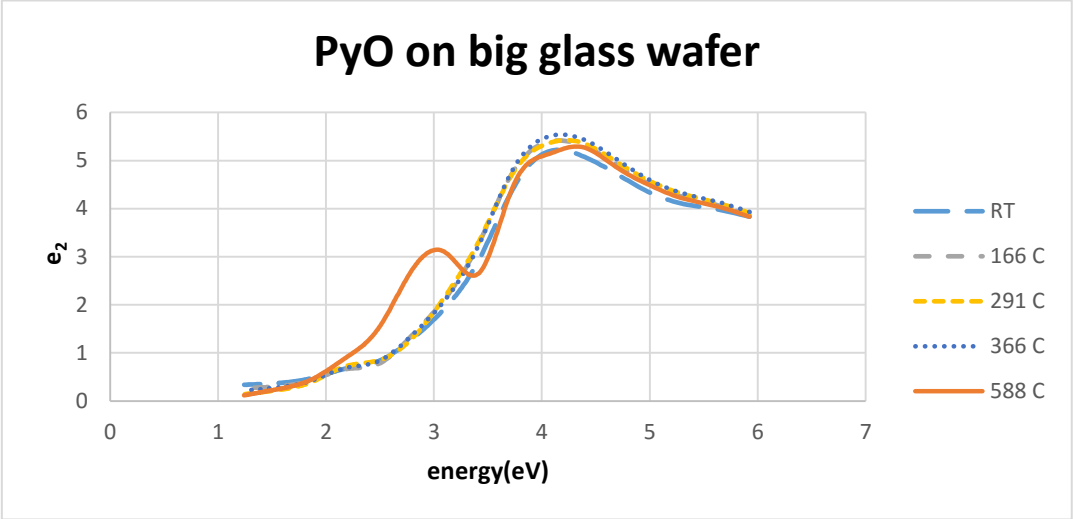

Fig. 19. Continued

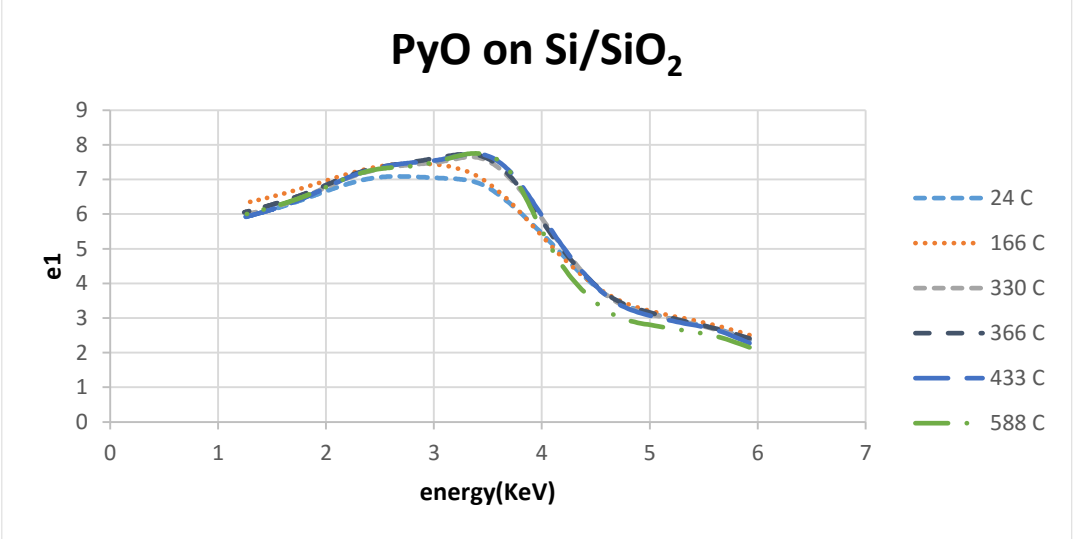

Fig. 20. ε_1 and ε_2 as a function of substrate deposition temperature for PyO on Si/SiO_2 substrates (calculated from ellipsometric data only)

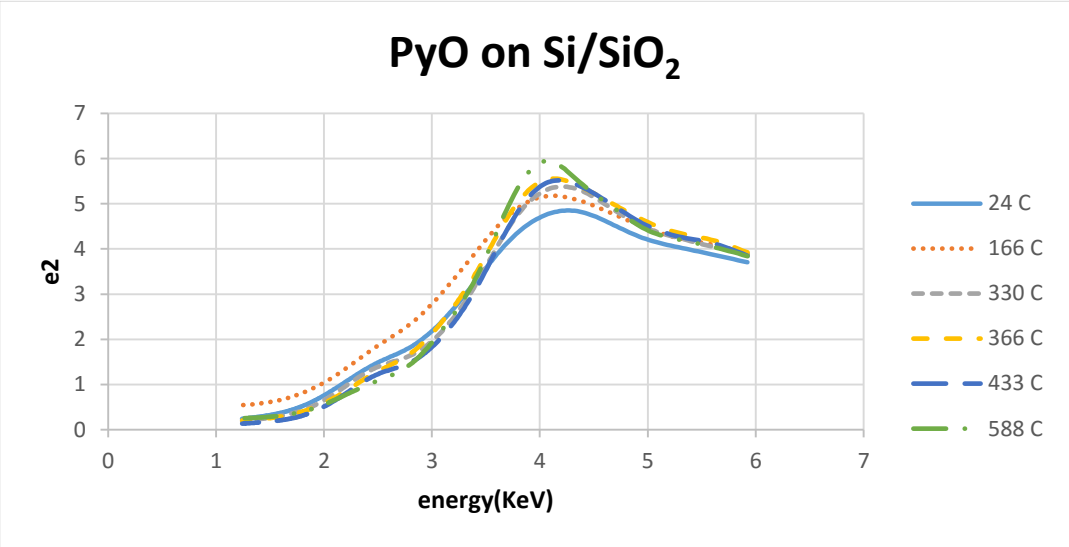

Fig. 20. Continued

3.4 Infrared Optical Properties of PyO.

The infrared optical properties of the 2nd temperature series were measured with a Woollam FTIR ellipsometer at Sandia National Lab. Measurements were done on samples deposited on Pella fused quartz and on samples deposited on Si/SiO_2. The objective of these measurements was to confirm that our PyO films had the rocksalt crystal structure and that the films did not contain other Fe-Oxide or Fe-Ferrite phases. The NiFe oxide phase diagram (see the first graph in Fig. 21 given below) [31] shows that it is hard to form a rocksalt NiFe-oxide structure at room temperature if the Fe concentration is beyond 2%. Note that Fig. 21a shows the phase diagram at atmospheric pressure. Fig. 21b (bottom) shows the phase dependence on the oxygen pressure at 1100°C for different oxygen partial pressures. The dashed line are the results obtained by [29]. At higher temperatures and lower oxygen pressure PyO seems to be stable. DFT calculations have shown that around

oxygen vacancies the nickel ions are slightly moved towards the oxygen position while around Fe impurities oxygen atoms are slightly moved away for the Fe's lattice site[34]. So local strain is opposite around oxygen vacancies and iron impurities. This could be the reason for enhanced stability at low oxygen pressure. The oxygen pressure during deposition is smaller than 10^{-6} atmosphere. Since sputtering is not an equilibrium process, the phase diagram might not be very relevant though.

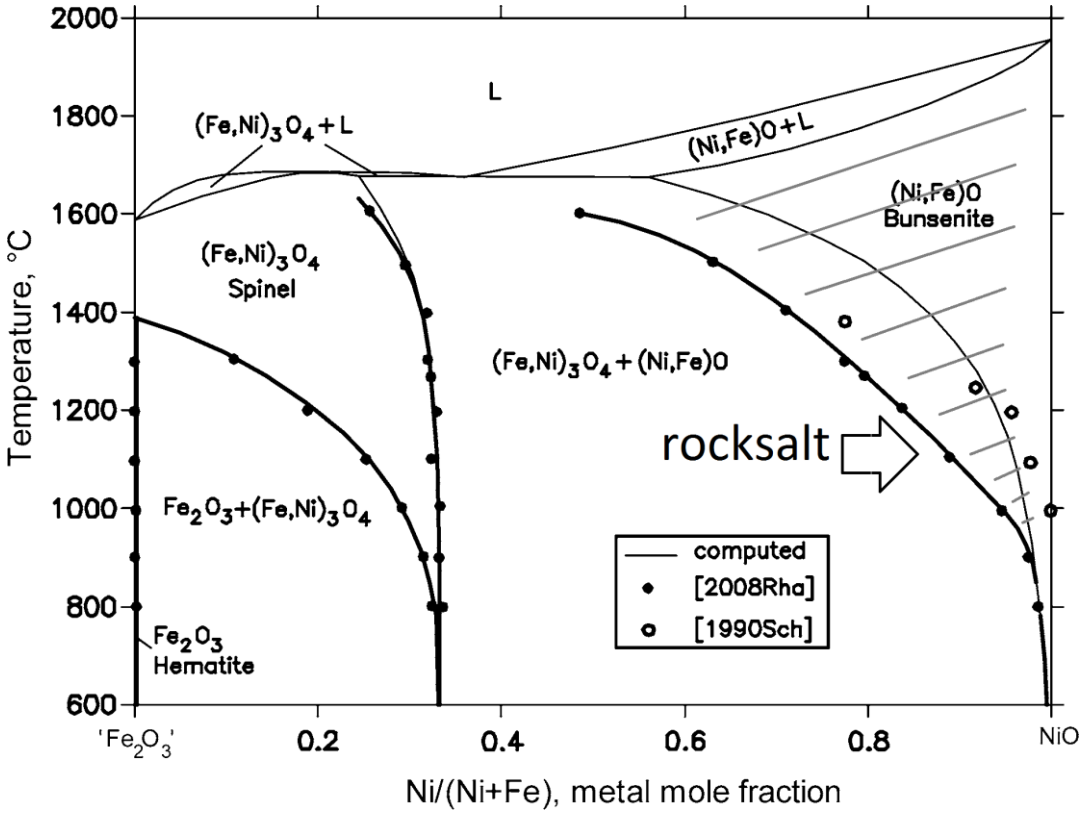

Fig. 21. (a) Phase diagram of NiFe-oxide in an air at 1 atmosphere (top) and (b) at 1100oC (bottom) [31]

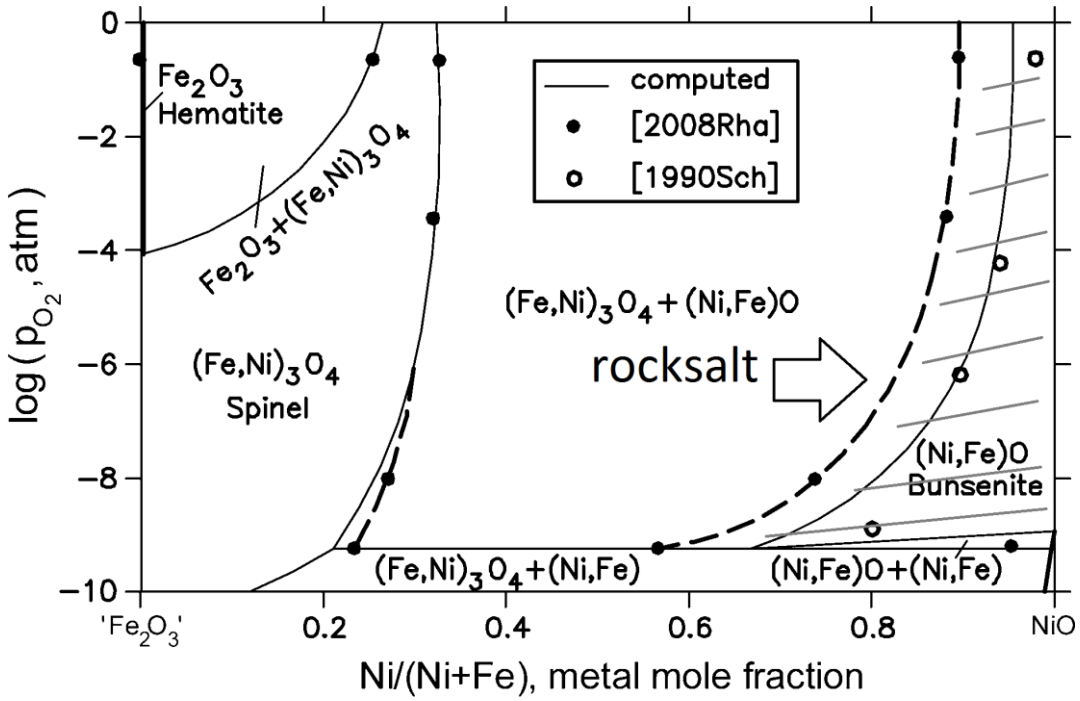

Fig. 21. Continued

The measured ellipsometric quantities of the bare substrates were analyzed in CompleteEase to determine the IR-optical properties of the SiO_2. Two different approaches were used to determine the optical dispersion of the SiO_2: a wavelength by wavelength fit and a fit consisting of 7 general oscillator peaks: 1 Lorentz and 2 Gaussian oscillators to describe the Si-O-Si rocking mode peak, 1 Gaussian oscillator to describe the Si-O-Si bending mode and three Gaussian oscillators to describe the Si-O-Si stretching mode. Both approaches gave similar results for the optical properties. The general oscillator model however results in small systematic errors near the base and top of the various phonon peaks. The oscillator model also creates a small shoulder on the low energy side of the lowest phonon peak. This existence of this shoulder is not justified by the raw data and was not observed in the data analyzed by a WvlByWvl fit. The wavelength by wavelength model resulted in a

noisier dispersion. Fig. 22 shows the ε_1 and ε_2 of the fused quartz substrate with phonon peaks at 453, 807 and 1073 cm^{-1}. This data is consistent with the literature. Kirk et al. measured phonon peaks at 457, 810, and 1076 cm^{-1} for dry SiO_2 on silicon wafers [35]. The Si/SiO_2 (103 nm) substrates used in this thesis show SiO_2 phonon peaks at 449, 807, and 1082 cm^{-1}. Note that the position of the low energy and high energy phonon peaks are slightly red, and blue shifted compared to the results of Kirk on dry oxide. Such shifts could be caused by stress or the technique used to growth the oxide. Pusep et al. found that wet oxide contains peak similar to crystalline SiO_2 [24].

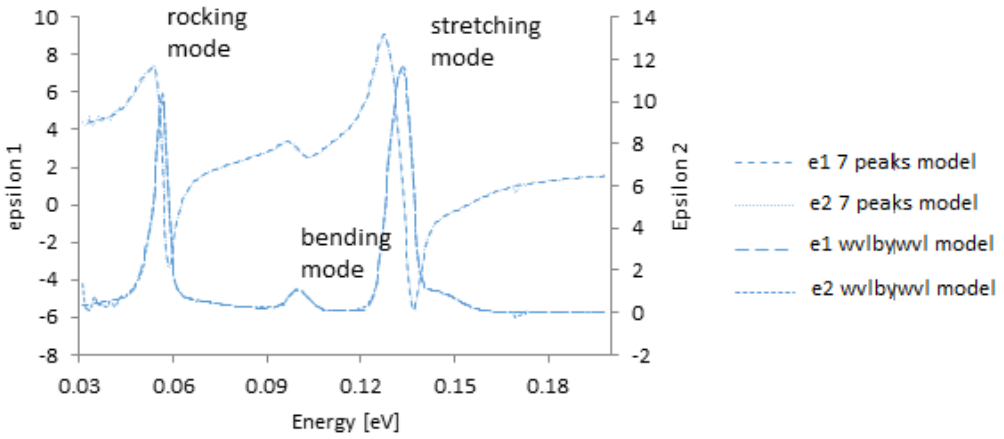

Fig. 22. The ε_1 and ε_2 spectra of the fused quartz substrate with three phonon peaks

The data analysis of the measured ellipsometric spectra was also done using CompleteEase. The result for the PYO samples sputtered at a substrate temperature of 588°C on the Si/SiO_2 wafer can be found in Fig. 23. The first two graphs show the pseudo dielectric constant for three different angles (green). The optical properties of the SiO_2 substrate (Fig. 22) and the film thickness determined from ellipsometric

measurements in the visible part of the spectrum (table 3.3) were used for the fit. The calculated spectra follow the measurement results closely through the infrared except below 500 cm^{-1}. The last two graphs show the measurement data again as well as a fit assuming the PyO contains a phonon described by a Lorentzian peak between 200 and 600 cm^{-1}. The Lorentzian peak was modeled according to the following equation:

$$\varepsilon(E) = \varepsilon_{\infty} + \frac{A_p Br_p E_p}{E_p^2 - E^2 - iBr_p E} \qquad \text{[Equation 3.1]}$$

Where ε_{inf} is the static dielectric constant, A_p is the peak height, Br_p is the peak width, and E_p is the peak position.

The one phonon (at around 381.5 cm^{-1}) fit has a small MSE. In addition, the same phonon was found in all the samples of both temperature series. Two different optical data sets for SiO_2 were used to analyze the data of the PyO samples. The details of the phonon peak calculated from the various samples are summarized in Table 6. The phonon peak position calculated from the SiO_2 optical properties derived from a 7 peak oscillator mode was slightly red shifted (column 2 at the top of Table 6). This shift is caused by the shoulder on the low energy side of the lowest SiO_2 phonon peak.

Table 6. Calculated PYO Phonon of RF sputtered PyO on fused silica

PyO on quartz (T in C)	SiO_2 modeled with WvlByWvl fit on quarts subst. (E_p, Br_p)	SiO_2 modeled by 7 peak general oscillator model on quartz subst. (E_p, Br_p, A_p, MSE, E_pBr_p)
588°C	376.7 cm^{-1}, 40 cm^{-1}	376 cm^{-1}, 60 cm^{-1}, 56, 23, 3360 cm^{-2}
433°C	384.7 cm^{-1}, 54 cm^{-1}	382 cm^{-1}, 77 cm^{-1}, 45, 33, 3465 cm^{-2}
366°C	384.6 cm^{-1}, 70.17 cm^{-1}	382 cm^{-1}, 86, cm^{-1}, 37, 18, 3182 cm^{-2}
330°C	381.3 cm^{-1}, 57 cm^{-1}	379 cm^{-1}, 74 cm^{-1}, 43, 17, 3182 cm^{-2}
166°C	377.46 cm^{-1}, 43 cm^{-1}	376 cm^{-1}, 92 cm^{-1}, 37, 16, 3404 cm^{-2}
24°C	382 cm^{-1}, 88 cm^{-1}	376 cm^{-1}, 115 cm^{-1}, 28, 14, 3220 cm^{-2}
average	381.12 cm^{-1}	378.5 cm^{-1}, 84 cm^{-1}, 41, xx, 3302 cm^{-2}
PyO on Si/SiO_2 (T in C)	SiO_2 modeled by 7 peak general oscillator model on quartz subst. (E_p, Br_p, A_p, MSE, E_pBr_p)	SiO_2 modeled by 7 peak general oscillator model on Si/SiO_2 subst. (ω_i, γ_i, A_i, MSE, $\omega_i\gamma_i$)
588°C	380.5 cm^{-1}, 112 cm^{-1}, 30, 15, 3371 cm^{-2}	381cm^{-1}, 110 cm^{-1}, 30.4, 10, 3344 cm^{-2}
366°C	386 cm^{-1}, 72 cm^{-1}, 44, 15, 3168 cm^{-2}	386 cm^{-1},71 cm^{-1}, 44, 7, 3124 cm^{-2}
391°C	384 cm^{-1}, 72 cm^{-1}, 43, 13, 3096 cm^{-2}	384 cm^{-1}, 72 cm^{-1}, 43, 5, 3096 cm^{-2}
166°C	383 cm^{-1}, 86 cm^{-1}, 37.6, 15, 3234 cm^{-2}	384 cm^{-1}, 85 cm^{-1}, 37.9, 7, 3222 cm^{-2}
11°C	378 cm^{-1}, 54 cm^{-1}, 17, XX, 3078 cm^{-2}	379 cm^{-1}, 59 cm^{-1}, 55, 9, 3245 cm^{-2}
average	382.3 cm^{-1}, 80 cm^{-1}, 42, xx, 3189 cm^{-2}	382.8 cm^{-1}, 79 cm^{-1}, 42, xx, 3206 cm^{-2}

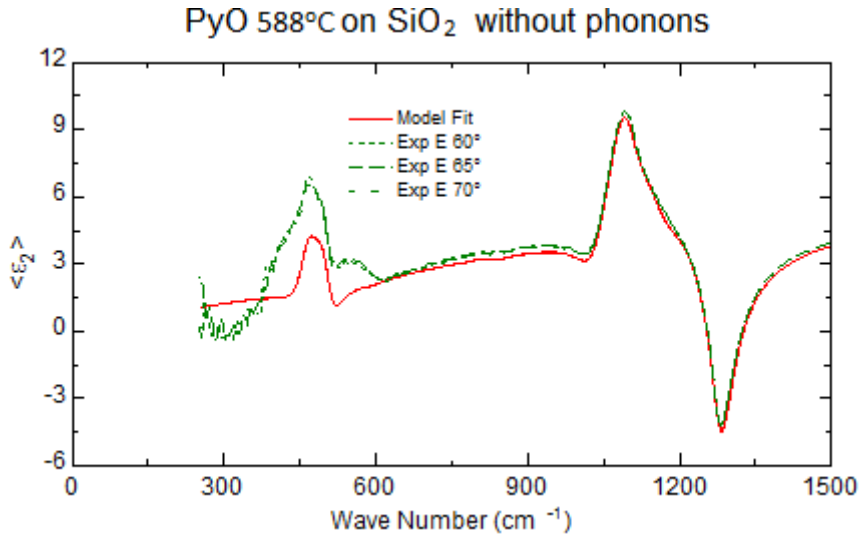

Fig. 23. $<\varepsilon_1>$ and $<\varepsilon_2>$ spectra of the quartz sample sputtered at 588°C assuming no phonon (top two) and assuming one phonon around 381.5 cm^{-1} (bottom two)

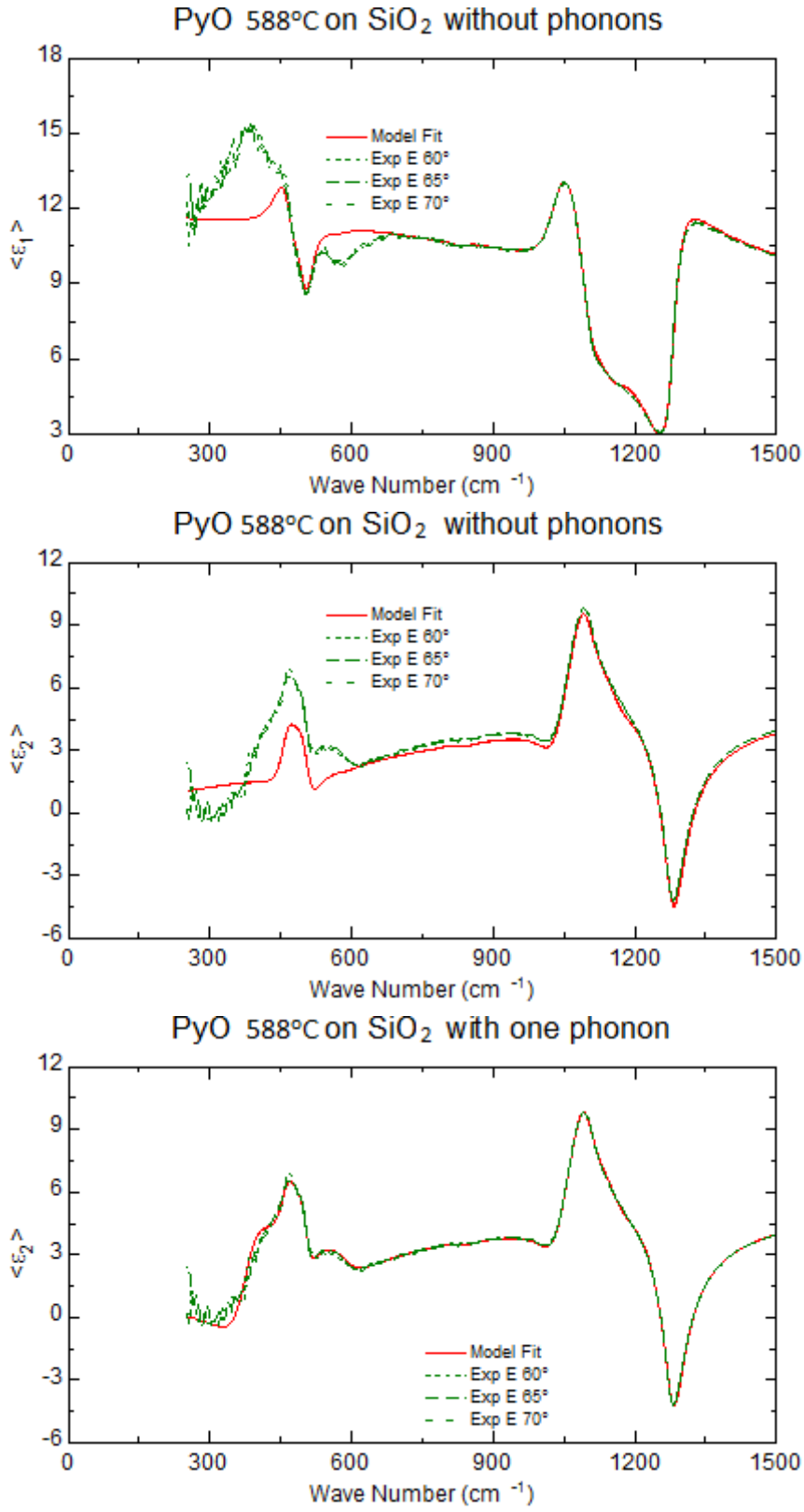

Fig. 23. Continued

In Table 3.5 the positions of the different FTIR active phonon peaks of other Fe phases are summarized and compared with the phonon peak position we found. There was not a phonon position that was similar to the position of the phonon we found. So we, therefore, conclude that the FTIR ellipsometry data confirms the rocksalt crystal structure of our PyO films. This is not a proof for the crystal structure but a confirmation. Taking a weighted average of the phonon peak of bunsenite and wustite, we expect the phonon peak of PyO to be located near 385-377 cm^{-1} which is consistent with our measurement results. The picture of a weighted average is consistent with the theoretical calculations of Fe-doped CoO by Wdowik et al. [36]. They used first principle methods to calculate the effect of Fe on the lattice dynamics and found Fe to introduce locally its own force constant splitting ω_{TO} into modes corresponding to oxygen vibrating around Co and Fe. The calculated vibration frequencies near Fe and Co are similar to the TO phonon frequencies in wustite and Co-II-oxide. A model assuming the PyO dispersion in the far-infrared as described by an effective medium approximation of two Lorentz oscillators at 390 and 325 cm^{-1} lowered the MSE of the fit, from 17 to 12 for the 588^{o}C sample on Si/SiO_2. At this moment, it is not clear whether or not this improvement is due to the large measurement noise in the IR or indicates evidence for the presence of both phonon peaks. Note that Raman spectroscopy is much more sensitive to other phases. So in the future, we should plan Raman spectroscopy on our films.

Table 7. FTIR active phonon peaks detected by others in different NiFe-oxide materials compared with PyO phonon peak detected in this work (s=strong, w=weak).

Material	Formula	Phonon [cm^{-1}]	Technique	reference
Magnetite	Fe_3O_4	340 (w), 450 (w), 560 (TO, T_{1u}, s)	FTIR	[37]
Hematite	α-Fe_2O_3	385 (A_{2u}, w),436 (TO, E_u, s)-459 (LO, E_u, w), 526 (TO, E_u, A_{2u}, s)	FTIR	[38]
Maghemite	γ-Fe_2O_3	440 (TO, T_{1u}, w), 546-547(TO, T_{1u}, s)	FTIR	[38]
Nickel Ferrite	$NiFe_2O_4$	438 (s), 676.2 (s), 339.4, 377	FTIR	[39]
Bunsenite	NiO	390-401 (TO, s)	FTIR	[40] [41]
Wustite	FeO	325 (TO, s), 534.7 (LO, w)	FTIR	[42]
PyO	$Ni_{0.81}Fe_{0.19}O_{1-\delta}$	381.5	ellipsometer	[32]

3.5 Summary

The cleaning process was studied in the temperature series using ellipsometry. The normal cleaning was not as good as the plasma clean and ozone clean. The roughing of the back of the substrates before deposition with a bead-blaster, resulted in better ellipsometry data, resulting in lower MSE values. Because of the roughening of the back of the substrates it was no longer possible to determine the transmission spectra. This leads to a big error when determining the optical properties from the ellipsometer measurement for the samples on fused quartz or glass substrates.

The crystal structure, size, orientation, and shape are very important for the RRAM application. Rocksalt FeO and NiO can be made to be non-stochiometric because both Ni and Fe atoms can exist in different valence states. Powder diffraction measurements on the samples show that PyO films sputtered at low pressure ($<10^{-3}$

mTorr) have a rocksalt crystal structure. According to the NiFe-oxide phase diagram PyO will have a rocksalt structure at elevated temperature in a low oxygen pressure atmosphere [32]. This suggests that our films might be meta-stable.

The films' thicknesses were determined from ellipsometric measurements in the NIRVISUV part of the spectrum. Three different models were used. The ellipsometry thickness of all three models was approximately the same and consistent with the thickness monitor and separate stylus profilometer measurements on test samples.

The optical properties in the visible part of the spectrum show peaks below the 4.5 eV bandgap peak. These low energy peaks were also observed by Gosh et al. on single crystalline NiO which was annealed in vacuum above 400^{o}C. The low energy peak suggests the presence of metallic atoms [41].

Ellipsometric measurements done in the IR part of the spectrum show a phonon peak around 381.5 cm^{-1}. The phonon peak measurements confirm that a rocksalt layer of PyO was made in our sample. It is similar to the phonon peak in NiO but red shifted [32].

IV. THICKNESS SERIES

4.1 Introduction.

Crystal size is important for RRAM application as filaments might form at the grain boundaries. Several studies have shown that RF sputtered NiO are not homogeneous through the film thickness [1]. To determine how PyO films are formed and the crystals grow, a thickness series was made. The structure was studied by AFM, SEM, 4pp and ellipsometry.

4.2 Sample preparation details

Four different substrates were used in this series, Si/SiO_2, $Si/SiO_2/Si_3N_4$, $Si/SiO_2/Al$, and standard microscope slides. The cleaning and other preparation of the substrates is the same as described in chapter 3 for the temperature series. Due to the equipment limitation, the longest deposition time for one continuous deposition run is 600s. The thickest film made is one for which the total deposition is 1200s. This sample was made using two sputter sessions of 600 seconds separated by a cool down period of 10 minutes. The thickness series was made with sputter gas consisting of 20% Oxygen and 80% Argon (total gas flow 10 SCCM. The flow rates measured by the mass flow controllers were used to determine the concentration (2 SCCM O_2 and 8 SCCM Ar). The 19% Fe target was used. The thickness monitor in the deposition system shows the deposition rate at this condition is about 1.2 Å per second. The details of the deposition including the parameters can be found in Table

4.1 shown below. The Woollam M2000 ellipsometer was used to determine the optical properties and measure the thickness of the samples. Also, the surface of the samples was studied by a scanning electron microscope (SEM) and an atomic force microscopy (AFM).

Table 8. Deposition parameters of thickness series all samples were sputtered with an Ar flow rate of 8 SCCM and an O_2 flow rate of 2 SCCM at room temperature the substrate was rotated during deposition

Sample number	Deposition time	Oxygen flow rate	Pressure	Power
0416	1200 s	20%	1.3E-3 Torr	240 W
0517	600 s	20%	1.3E-3 Torr	240 W
0553	300 s	20%	1.3E-3 Torr	240 W
1100	150 s	20%	1.3E-3 Torr	240 W
1132	75 s	20%	1.3E-3 Torr	240 W
1158	38 s	20%	1.3E-3 Torr	240 W

4.3 SEM measurement

4.3.1 Equipment and procedure

The samples were attached with a carbon tape to the holder of the SEM. SEM studies were performed on the PyO films deposited on $Si/SiO_2/Al$ substrates to reduce charging effects in the electron microscope. No attempt was made to cover the samples with a conductive Au layer to reduce charging effects. The thickness series were made in July 2014 and the SEM measurement was done in the summer of 2015.

4.3.2 Measurement on PyO samples deposited on Si/Al substrates

SEM measurements were challenging because of charging effects. The PyO has a

large resistivity and in particularly the obtained images of the thicker films was poor. The surface of the samples can be modified by the charging effect of the electron beam especially when zooming in (high magnification) the effect of charging effects is significant and modifies the surface in seconds. The best SEM image with the highest resolution was obtained on the thinnest sample (d=8.8 nm). The charging effect on that thinnest sample was not homogeneously, resulting in slight variations of the image brightness across the sample. On the other samples, the resolution was less good.

Features of the PyO films with a dimension less than 100 nm were observed, as shown in Fig. 24 below. Small insulating particles on the surface that get charged appeared as white dots. After initial charging of the particle, the particles will be more efficiently backscatter the incident electron beam. The dark lines across the images are believed grain boundaries of the Al substrate. The conducting path to the substrate is better for those areas of the thin film. AFM measurements on the aluminum substrate have shown that the aluminum film on top of the silicon is not smooth (see also below) and consist of larger grains typically 500 nm in diameter. The thin PyO film on top of the aluminum shows the same morphology. For some of the thinner films dark areas exists away from the grain boundaries. This could mean that the film is more conductive in those areas.

On the top left is the thickest sample (with 1200 s deposition time). At the bottom right is the thinnest sample. In general, the thicker samples showed the larger structures on the surface. The results show that the thinner the film the smaller the

structures on the surface or, the better the resolution of the SEM images. Thicker films have a higher resistance, which means that also charging effects will become more pronounced in thicker films.

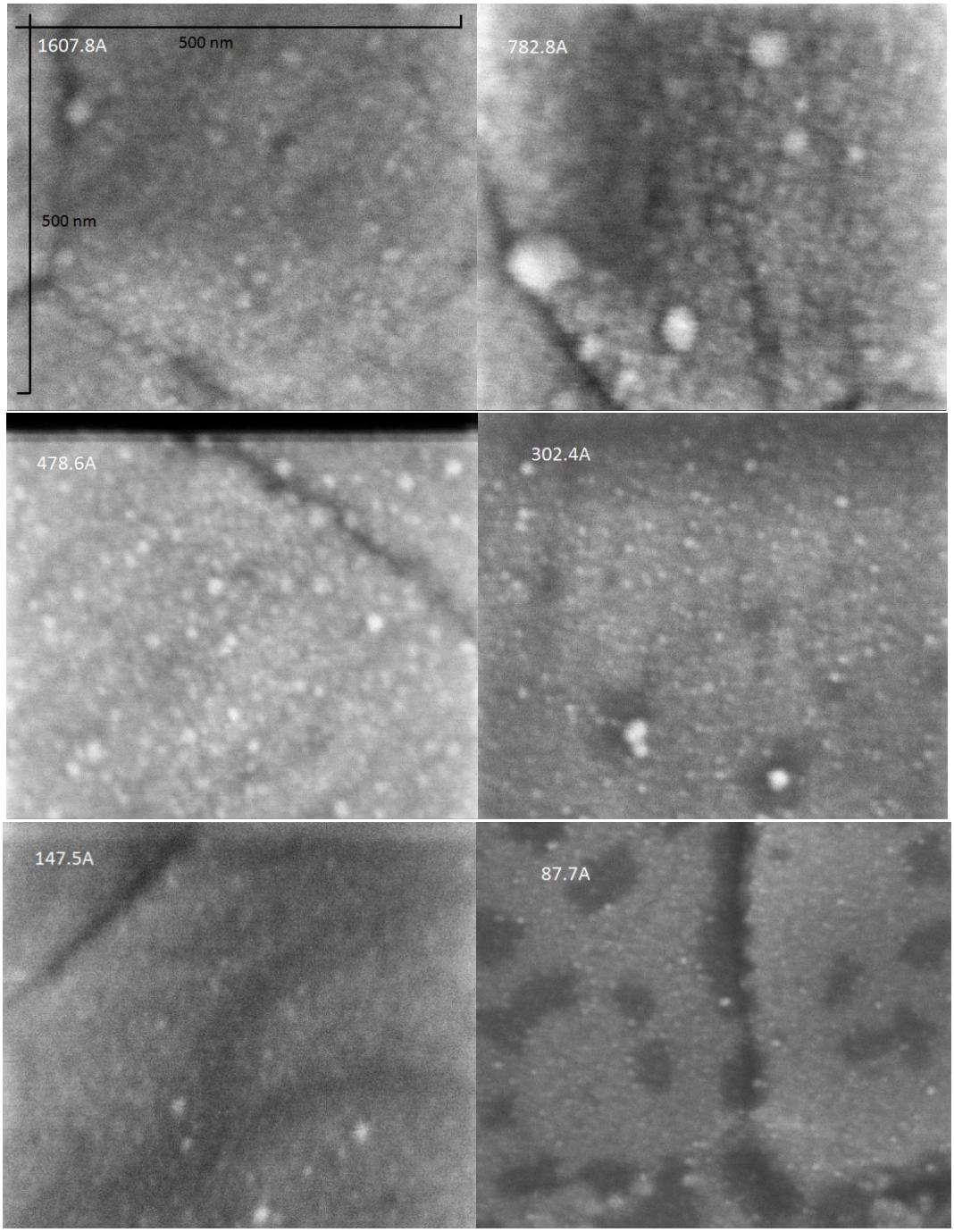

Fig. 24. SEM measurement on PyO thin films of different thickness on Al samples with 3KeV energy and 0.34 nA current, 160.7 nm (top left), 78.2 nm (top right), 47.9 nm (middle left), 30.2 nm (middle right), 14.8 nm (bottom left), and 8.8 nm (bottom right)

The Fig. 25 below shows the AFM measurement on the 150s (30.2 nm) deposition time PyO sample (Al substrate). Note that the observed area is a factor 10 larger than the area imaged in the SEM pictures of Fig. 25. The observed grain size is approximately 500 nm, and the sample has a relative large roughness. The large roughness of the samples deposited on $Si/SiO_2/Al$ had to be taken into account when determining the film thickness from the ellipsometer data.

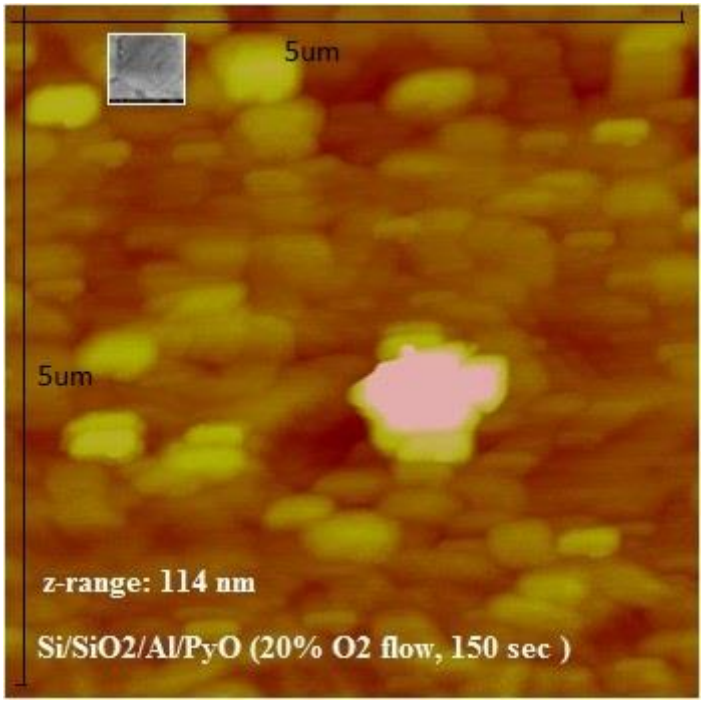

Fig. 25 AFM measurement of $Si/SiO_2/Al/PyO$ film of 30.2 nm thickness

4.4 Ellipsometry

4.4.1 Equipment and experimental procedure

A Woollam M2000 ellipsometer was used to determine the optical properties and the film thickness of the samples.

Two different fit recipes were used:

1. Optical properties of PyO were modeled with a one peak Cody Lorentz model in Complete Ease. No surface roughness was assumed, and no angle of incidence correction was applied. Fit parameters were the parameters of the Cody Lorentz model and the thickness.
2. Optical properties were modeled with a B-spline model (resolution is 0.3 eV, 16 pts). Again no surface roughness and angle correction were applied. Fit parameters were film thickness, refraction index, and extinction coefficient. The fitting technique will allow for more than one peak in the optical properties to be modeled. The results of the Cody-Lorentz fit were used as the starting point for a wavelength by wavelength fit. The result of the wavelength by wavelength fit was then used as a starting point for a B_spline fit.

The MSE of the B-spline fit was significantly lower than the MSE of the Cody-Lorentz fits. But the B-spline model itself has no physics meaning.

Most works of the ellipsometry research were on the samples sputtered on Si/SiO_2 substrates. These samples had a lower surface roughness and looked cleaner. The samples sputtered on $Si/SiO_2/Al$ were rougher as concluded from AFM measurements. The samples on glass showed a white haze 1 year after deposition. The roughness measurement of PyO films are discussed in more detail in chapter 5. The B_spline model fitting on the PyO samples on $Si/SiO_2/Si_3N_4$ substrates was not very smooth. Accurate values of the optical properties of Si_3N_4 were not available. Furthermore, the PyO samples on $Si/SiO_2/Si_3N_4$ have a complex structure with three

transparent layers on bulk silicon.

4.4.2 Measurement and fitting result

The fitting results are summarized in Table 9. The PyO samples on the $Si/SiO_2/Si_3N_4$ were only analyzed by recipe 1. For the samples on the other substrates, both recipes were used. The B_spline fitting gave a low MSE and a similar thickness result as the Cody-Lorentz model fit. The thickness differences between both models were smaller for the thicker films and became larger for the thinner films.

Table 9. Fitting result of thickness series

Sample number	deposition time(s)	Si_3N_4/PyO(Å)	MSE	SiO_2/PyO(Å)	MSE	B_spline(Å)	MSE
1158	38	43.3	14	46	27	61.26	10.58
1132	75	97.13	13.5	101.65	38.4	130.83	13.24
1100	150	224.18	17.8	223.28	31.8	230.64	10
553	300	380.96	18.3	385.8	24	387.4	12.12
517	600	772.09	26.7	756.47	31	759.42	8.6
416	1200	1467.61	27.1	1522.44	27.4	1594.79	15.53
	Dep. time(s)	Al/PyO(Å)	MSE	B_spline(Å)	MSE		
1158	38	64.58	5.5	87.66	2.49		
1132	75	104.67	15.8	147.5	3.03		
1100	150	250.87	69.5	302.36	5.08		
553	300	503.76	25	478.58	3.76		
517	600	761.44	28	782.79	5.47		
416	1200	1554.09	34.3	1607.84	4.11		
	Dep. time(s)	Microsc. Slide(Å)	MSE	B_spline(Å)	MSE		
1158	38	61.19	38.73	226.94	33.98		
1132	75	152.19	27.69	445.24	19.2		
1100	150	345.45	12.101	374.65	8.52		
553	300	402.39	13.61	474.34	7.1		
517	600	787.59	23.08	759.34	3.94		
416	1200	1582.37	37.68	1453.65	12.21		

4.4.3 Deposition rate

The deposition rate of the PyO layer on SiO_2 samples computed from the ellipsometry thickness and the deposition time is shown in Table 10. With the time increasing, the deposition rate decreased, and for the very thick film, the deposition rate became larger again. There is a large difference between the measured deposition rate between thinner and thicker films. The difference might be a modeling issue. The optical properties seem to change as a function of the film thickness as suggested by the spectra shown in Fig. 27. This effect has also been observed by others for RF sputtered NiO layers. RF deposited NiO films have a seedlayer of approximately 20 nm that has different optical properties from the rest of the film [1] [43]. As the model does not assume that the optical properties vary through the thickness of the film, large errors are expected between 10-30 nm where both the seed-layer and top layer are probed by ellipsometry. The decrease in the deposition rate for the thickest sample can be explained as the result of two deposition sessions. The deposition needs to be stopped every 600s to cool down the sputter gun. The waiting time between two sputter runs is at least 10 minutes. So the thick film consists of two films of 600 seconds stacked on top of each other. If the top film between the very thin and very thick is homogeneous, the deposition rate curve of PyO should be linear. As that is not the case, the optical properties of the material sputtered just after the shutter is opened is different from the optical properties of the material sputtered after the shutter has been open for a while. Fig.

26 shows the thickness vs deposition time curve. The relation has clearly two linear regions with each their own slope. The measured deposition rate was not independent of the film thickness. This could be caused by the change of the optical properties of the sputtered material during the deposition.

Table 10. Deposition rate of PyO on Si/SiO_2

Deposition time (sec)	Deposition rate (Å/s)
38	1.33
75	1.27
150	1.29
300	1.54
600	1.74
1200	1.61

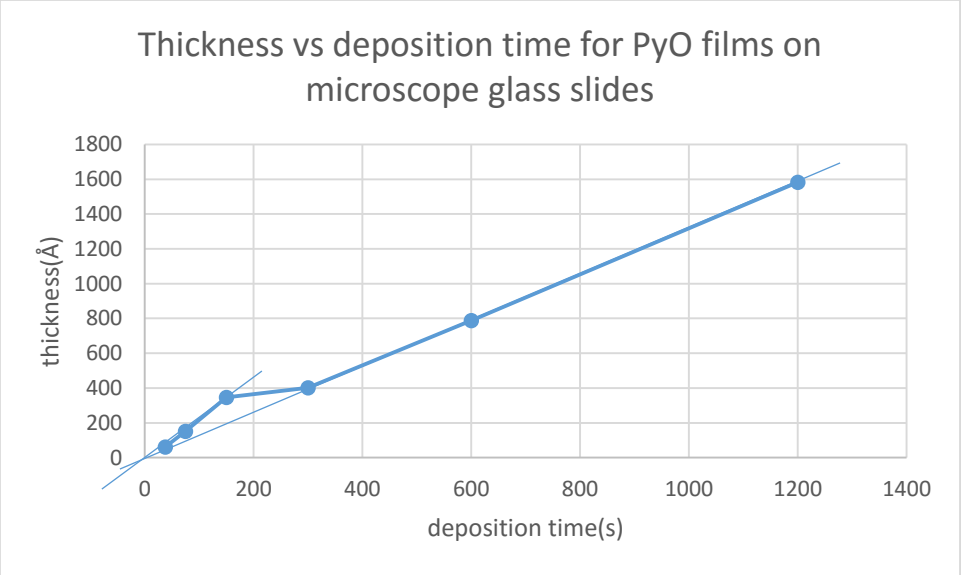

Fig. 26. Deposition thickness vs deposition time of PyO sputtered on Si/SiO_2

4.4.4 Optical Properties

The optical properties were determined at the same time as the thickness of the PyO films. Fig. 27 shows the ε_1 and ε_2 of the Si/SiO_2/PyO. . The optical properties change

as a function of the film thickness. The absorption, i.e. ε_2, increases for thicker films. The thicker films also appear to have a larger refraction index. The thickness dependence of the optical properties can have two reasons:

a. The thin films are stressed, and stress is relaxed in thicker films. This would mean that the optical properties of the thin films are anisotropic.

b. The optical properties vary through the film. This can be caused by (1) a change in the chemical composition of the film during sputtering; (2) a change of the crystal size and/or orientation during the sputtering process.

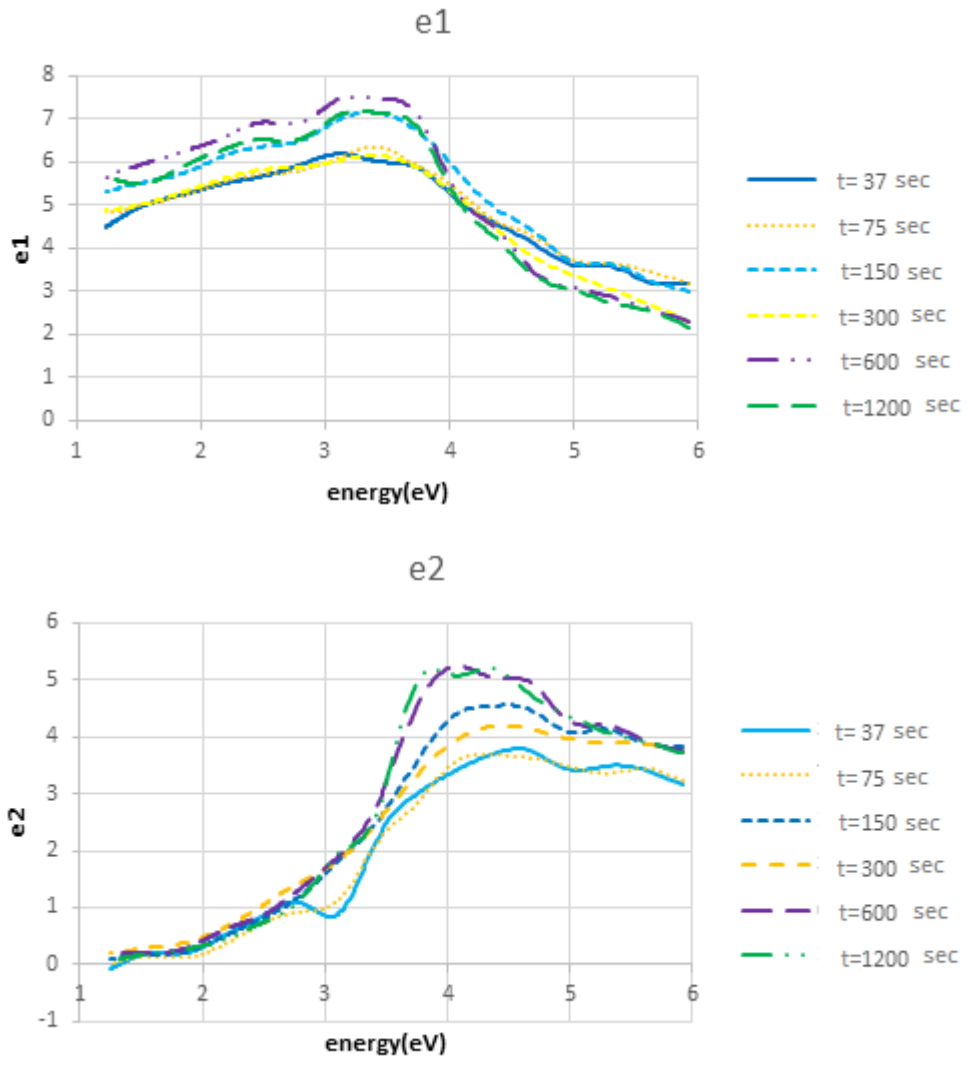

Fig. 27. ε_1 and ε_2 of Si/SiO_2/PyO samples of different thickness

4.4.5 Anisotropic Model

For all the fitting reported in this chapter, it was assumed that the PyO films made by our deposition system were isotropic. The next fitting used an anisotropic model and assumed that the optical properties for light polarized parallel to the substrate differs from the optical properties for light polarized perpendicular to the substrate. Fig. 28 shows the difference between the real and imaginary part of the dielectric constant for the isotropic and anisotropic model. Comparing the data in Fig. 27 with the data in Fig. 28, the differences are significant (more than 100% for the thinnest sample). Note that the anisotropic measurement and fitting is not expected to be very accurate. The angle of incidence variation in this study was from 55 degrees to 75 degrees. The refractive index measured on the PyO that was about 2.5 infor most of the visible part of the spectrum. The variation of the angle of refraction was calculated by the equation 4.1 below

$$n = \frac{\sin(\theta_i)}{\sin(\theta_r)} \qquad \text{[Equation 4.1]}$$

n ---refractive index

θ_i ---angle of incidence

θ_r ---angle of refraction

The calculated variation of the angle of refraction was from about 19 to 23 degrees. This small variation cannot give a very accurate estimatefor the anisotropic optical properties. The lower MSE of the anisotropic fit is caused by the larger number of fit parameters.

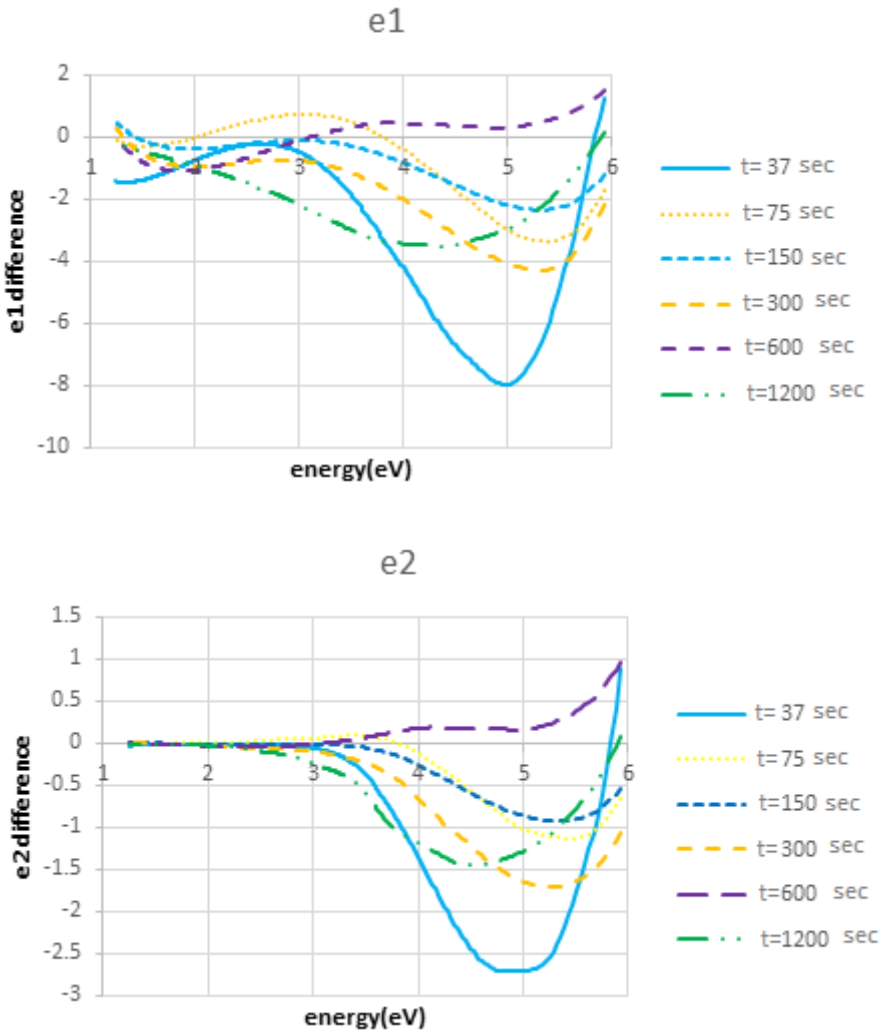

Fig. 28. Difference of optical properties between the normal and the anisotropic fitting of the thickness series

4.5 Electrical Characterization

The resistance was also measured on the thickness series. The electrical 4pp

characterization station was used to determine the resistance. Table 4.4 shows the measurement result of the resistance for different film thickness.

Table 11. Electrical measurement on thickness series

thickness by time, d_t (Å)	thickness by ellipsometer, d_e (Å)	$R_{measured}$ 4pp (Ω)	ρ_{sheet} (Ω/□)	Resistivity (Ω cm)	$1/\rho_{sheet}$ (□/Ω).	d_t/ρ_{sheet} (Å□/Ω)
1440	1529	4.45E+08	2.02E+09	3.08E+4	4.96E-10	7.14E-07
720	778	2.85E+09	1.29E+10	9.30E+4	7.75E-11	5.58E-08
360	440	7.59E+10	3.44E+11	1.24E+6	2.101E-12	1.05E-09
180	203	1.37E+10	6.23E+10	1.12E+5	1.61E-11	2.89E-09
90	90	8.65E+10	3.92E+11	3.52E+5	2.55E-12	2.30E-10
45.6	43.5	1.98E+11	8.98E+11	4.10E+5	1.11E-12	5.08E-11

In Fig. 29 the thickness vs resistivity curve is plotted. It shows a large variation of the resistivity of the samples with different film thickness. The resistivity decreases during the deposition (except for the 440 Å thickness sample). The resistivity of the thickest film was approximately a factor 10 smaller than the thinnest samples. The same behavior is also shown in Fig. 30 which shows the reciprocal value of the sheet resistance. A two sloped curve is observed. In addition, this figure looks similar to the curve in Fig. 28 which shows the deposition time versus the film thickness. The 360 Å film data deviates from the other samples. The optical properties curve also showed that this sample deviated from the other samples in the thickness series.

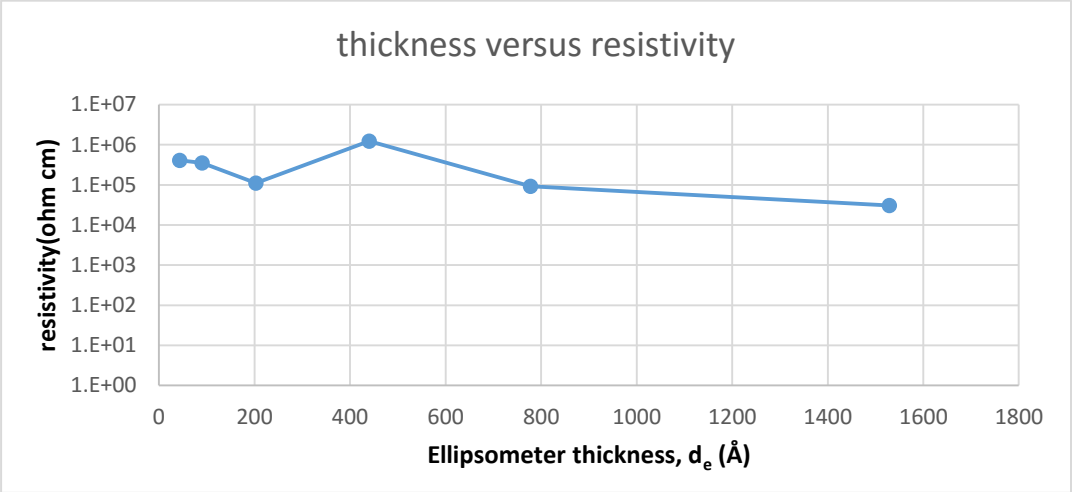

Fig. 29. Thickness vs resistivity

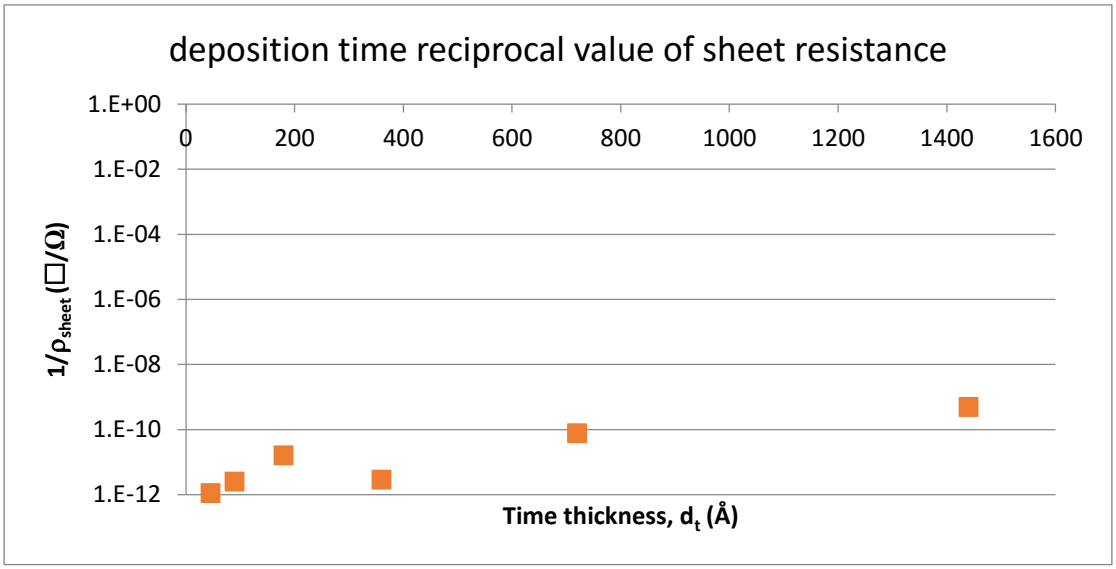

Fig. 30. Deposition time vs $1/\rho_{sheet}$

4.6 Summary

AFM measurements showed that the PyO films are smooth and that the roughness measured on our samples is mainly caused by the roughness of the substrates. Resistivity and optical properties of RF sputtered films change as a function of the film thickness. The initial PyO layer of approximately 200 Å had different properties than the thicker films. The very thick sample had a lower resistivity than the thin films. The optical absorption also increased with the film thickness. The thickness can

also change the crystal size of our PyO thin film. With increasing film thickness an increasing size of crystals were observed from SEM measurements. It is expected that crystal size can change the switching behavior as the switching can happen at the boundaries of the crystals. A future study needs to determine the switching behavior of the samples as a function of the film thickness. The thickness dependence of resistivity does not avoid this material to be successfully applied in RRAM devices.

V. EFFECT OF O_2 FLOW/CONCENTRATION IN PYO

5.1 Introduction

The concentration of different atoms in the thin film will change the optical properties and electrical properties a lot. The Oxide percentage is important for RRAM. Switching of the oxide material in the memory cell is based on Oxygen vacancy diffusion. The Fe concentration is expected to improve the switching properties of the memory cell, and change the resistance values of the low and high resistance states and the switching levels. So the effect of different Oxygen flow rates and Fe concentrations were studied in this chapter.

To detect the effect of O_2 concentration on the properties of PyO two O_2 flow rate series were made. The deposition parameters were similar to the study of the previous chapter but the percentage of oxygen gas in the sputter gas was varied among the various samples. The sputter power was 240 Watt and all samples were deposited at room temperature. The total gas flow was kept at 10 SCCM. The concentration of oxygen in the sputter gas was varied by the settings of the argon and oxygen mass flow controllers from 5% to 20%. Two film series were made using two different NiFe targets: a 10 at. % and 19 at. % Fe target. The detailed information of the O_2 series is shown in Table 12. The first series used the 19% Fe target and was on glass, $Si/SiO_2/Al$, Si/SiO_2, and $Si/SiO_2/Si_3N_4$ substrates. The samples of the 19%-Fe series were measured by the Woollam M2000 ellipsometer. The other O_2 series was made using the 10%-Fe target and deposited on Pella quartz instead of glass

microscope slides. The reason quartz was used was that quartz has a better transmission in the UV part of the spectrum [44]. The second series was measured by the Horiba ellipsometer. The samples were furthermore characterized by EDAX and 4pp.

Table 12. Deposition parameters of O_2 flow rate series with 10 SCCM total gas flow and 240 Watt power 10 minutes deposition time and pressure about 1.3E10^{-3} Torr

Sample number	target	O_2 flow	target	O_2 flow
0100	$Fe_{0.10}Ni_{0.90}$	5%	$Fe_{0.19}Ni_{0.81}$	5%
0144		7%		7%
1259		10%		10%
0349		14%		14%
0428		20%		20%

5.2 EDAX

The samples were measured by EDAX in the SEM to determine the concentration of elements in the PyO layer. The concentration was expected to vary with O_2 flow rate and target concentration. Measurements were done at different electron beam energies and different angles of incidence. For higher electron beam energies elements deeper in the samples were detected [45]. The PyO samples on Si/SiO_2/Al wafers were measured because these samples had a lower resistance. Furthermore, these samples do not have oxygen in the substrate. To obtain good quantitative results with EDAX, measurements are normally compared with standards. Since no standards were available for this study, a simulation was needed.

5.2.1 Experimental Procedure

The EDAX peaks of the elements that are present in the samples are listed in Table 13 below. The expected X-ray intensity depends on the beam energy. A small overvoltage would lead to less efficiency of X-ray excitations, and a large overvoltage will generate the X-rays too deep increasing their chance to be absorbed by the sample. It is common practice to use a minimum over-voltage of 2 keV and a maximum over-voltage ratio of 10-20. Note that at lower over-voltages the proportion of the interaction volume where the atoms can be excited becomes very small and not many X-rays will be generated for that particular element. For over-voltages in excess of the maximum, the proportion of the interaction volume for which the low energy X-rays can escape without being absorbed becomes small. For both cases, the corrections become large, magnifying statistical errors. For the investigation of thin films, the latter might not be so relevant since the oxygen, iron and nickel are only located at the top of the thin film system. It is clear from the data below that for 3 keV the penetration depth of the beam is less than the thickness of the NiFe-oxide sample and that for 5KeV or higher the beam also reaches the Aluminum.

The depth that X ray can detect depends on the measurement energy, angle, and target material and can be calculated by the Anderson and Hasler equation

$$R_x = \frac{0.064}{\rho}(E_0^{1.68} - E_c^{1.68}) \qquad \text{[Equation 5.1]}$$

R_x---measurement depth in μm

ρ---density in g/cm^3

E_0---measurement energy in keV

E_c---absorption edge in keV [46]

The information depths for the Al substrate (Si/SiO2/Al) were calculated using MCXray. The layer thickness, measurement current, and measurement energy were used to simulate the Al substrate. For incident beam energies of 5KeV and 10KeV. The information depth was 2400 Å and 8500 Å respectively. The thickness of the Al layer of the Al substrate was 3760 Å so at 5KeV the simulation result was not showing the peaks of the SiO_2 layer under the Al. The Si peak can be found in the 10KeV simulation results though.

Table 13. EDAX X ray peaks and recommended beam energies Ni, Fe, and O [47]

element	type	Energy	Min. Beam Energy	Max. Beam Energy
O	K-alpha	0.525 keV	2.525 keV	10.5 keV
Fe	L-alpha	0.705 keV	2.705 keV	14.1 keV
Ni	L-alpha	0.851 keV	2.851 keV	17.02 keV
Al	K-alpha	1.559 keV	3.559 keV	31.18 keV
Si	K-alpha	1.838 keV	3.838 keV	36.76 keV
Fe	K-alpha	6.398 keV	8.398 keV	127.96 keV
Fe	K-beta	7.057 keV	9.057 keV	141.14 keV
Ni	K-alpha	7.471 keV	9.471 keV	149.42 keV
Ni	K-beta	8.236 keV	10.236 keV	164.72 keV

To check the status of the EDAX system, the Table 5.3 below shows the K-alpha, K-

beta, and L-alpha peaks of Ni and Fe at a beam voltage of 18 kV together with the theoretical values.

Table 14. X-ray peaks of Ni and Fe and O at 18 kV energy

	literature	Experiment
O K-alpha	0.525 keV	0.52 keV
Fe K-alpha	6.398 keV	6.42 keV
Fe K-beta	7.057 keV	NA
Fe L-alpha	0.705 keV	0.76 keV
Ni K-alpha	7.471 keV	7.49 keV
Ni K-beta	8.236 keV	8.27 keV
Ni L-alpha	0.851 keV	0.82 keV
N K-alpha	0.393 keV	0.43 keV
Al K-alpha	1.487 keV	1.49 keV
Al K-beta	1.557 keV	NA
Si K-alpha	1.740 keV	1.75keV
Si K-beta	1.836 keV	NA

5.2.2 Data Analysis Procedure

It is not possible to determine the concentration and thickness of the thin film from the EDAX results using the SEM of Tx state University. The EDAX TEAM software assumes that the sample is bulk. Recent new developments, however, show that it should be possible to determine the film thickness and thin film concentration from EDAX measurement results. Oxford Instruments developed software, i.e. ThinFILMId and LayerProbe to calculate the film thickness and composition from EDAX measurements performed on thin film and multilayer samples. As Texas State, however, does not have an EDAX system from Oxford Instruments, McXRayLite was

used to simulate the result from the EDAX results gathered on the PyO samples. The Monte Carlo model (MC) is a widely used model to simulate the EDAX result of SEM equipment. The model has been used since the mid-1960s [48]. Several public-domain software programs have been developed to simulate the process of scattering of the electron beam in a solid material, including Casino, Win X-ray, and McXray [49][50][49][51]. Win X-ray and McXrayLite can also estimate the X-ray spectrum. The simulations in this chapter are done with McXrayLite. This software can calculate X-ray spectra (cps/nA) for a thin film or multilayer system from the model of the sample and the measurement conditions. The measurement conditions, include the beam energy, the beam angle, the beam current, and the detector configuration and type. The sample model includes the chemical composition of the layers, the layer's density, and the thickness of the layers. The software cannot fit EDAX measurement results automatically. So in this study, the software was used manually to generate a result from an assumed model of the sample which was then compared with the real measurement results. Model parameters of the sample such as concentration and film thickness were modified until a good agreement between calculated spectra and measured spectra was obtained. The approach is based on the work of Pouchou [52].

The following procedure was used:

1. First, a model of the sample that is going to be simulated was entered in the software. The first layer of the model is the substrate layer, and the thickness needs to be thick, so it looks like infinity for the electron beam. 20000000000 Å is

the defined thickness in that software. Then the other layers were entered in the software.

2. Second, the parameters of the microscope were entered into the system. Parameters entered include acceleration voltage, beam current, beam angle, and X-ray resolution that can be found in the Tables below.
3. Third, the concentration, film thickness, and beam current were changed until the simulated results were similar to the measurement results. Calculated and measured spectra were compared by eye. No attempt was made to calculate a mean square error.
4. Then the same model was used to determine the X-ray spectra at other electron beam energies to check if the model is consistent with all measurement results.

An example of the calculated and measured spectra is shown in Fig. 31.

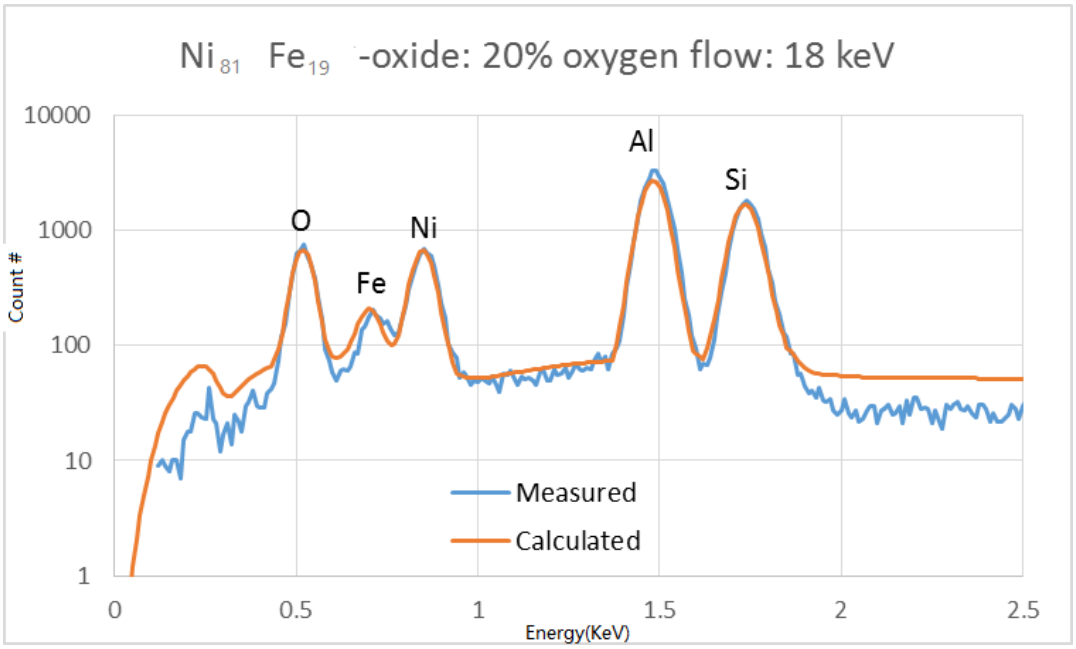

Fig. 31. Calculated and measured spectra of PyO sample with 20% Oxygen flow measured at 18 keV

5.2.3 Measurement results and data analysis of the $Si/SiO_2/Al$ substrate and the

Si/SiO_2/Si_3N_4/Al substrates

The 19% Fe samples were sputtered on Si/SiO2/Al substrates. The EDAX measurements and the fit for those substrates are presented in this section. Using the same model parameters, the simulations reproduced the measurement parameters done at all beam energies (3-18 kVolt) within 5%. Table 15 shows the detail of the model. Fig. 32 to 36 show the measured (left) and calculated spectra. The fitting is good for the fitting of the spectra measured at low energy (Fig. 32) was off. The same way as shown in the other study [48] [53].

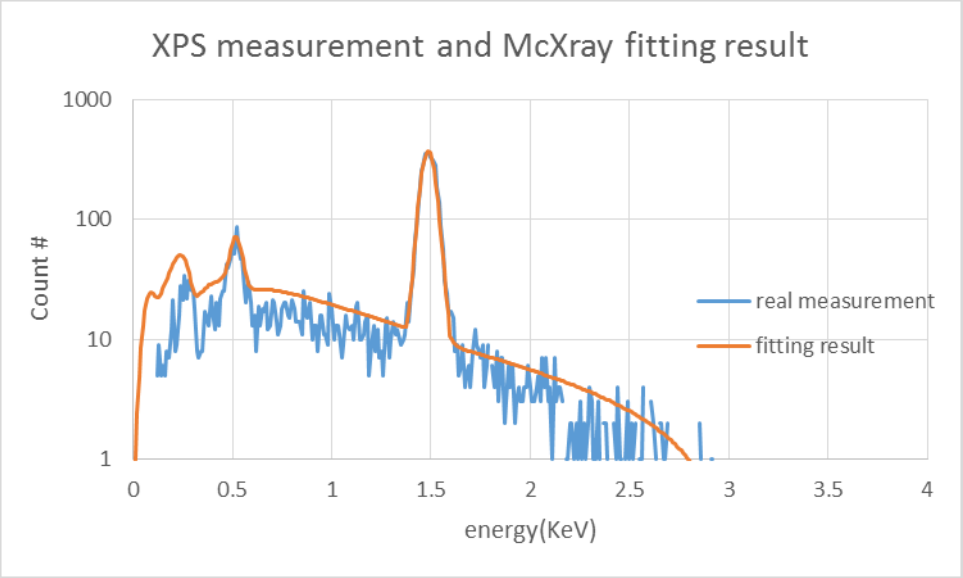

Fig. 32. Real measurement and fitting result compared at 3 keV energy

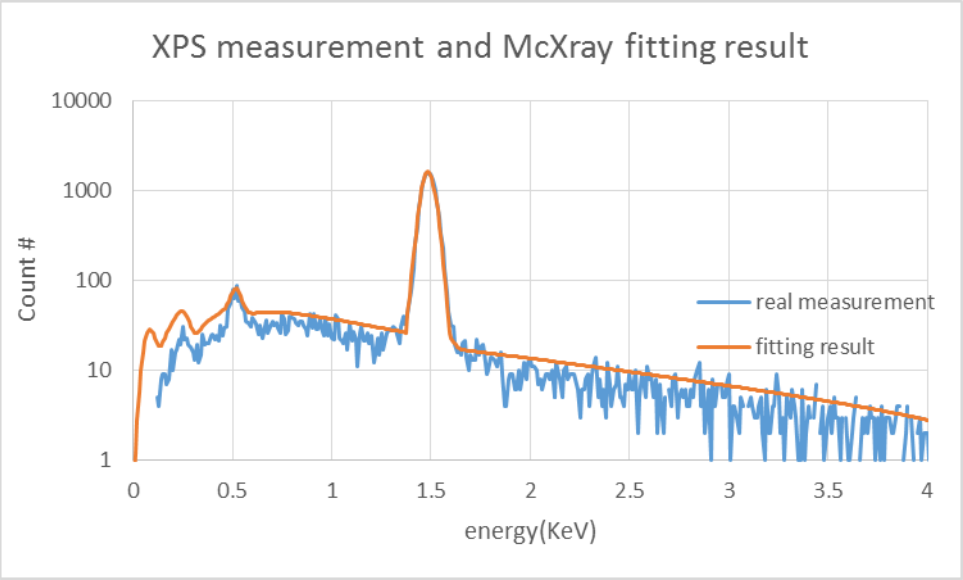

Fig. 33. Real measurement and fitting result compared at 5 keV energy

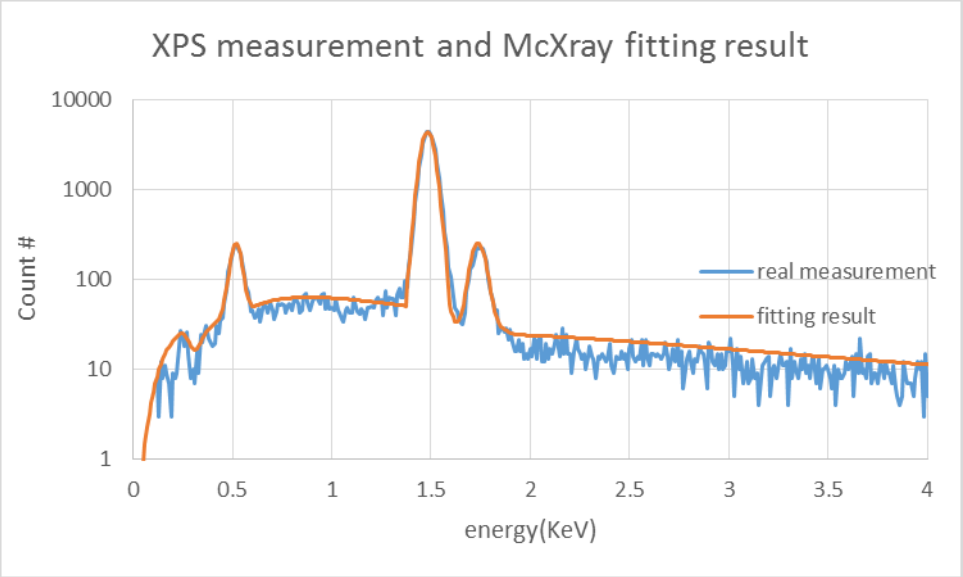

Fig. 34. Real measurement and fitting result compared at 10 keV energy

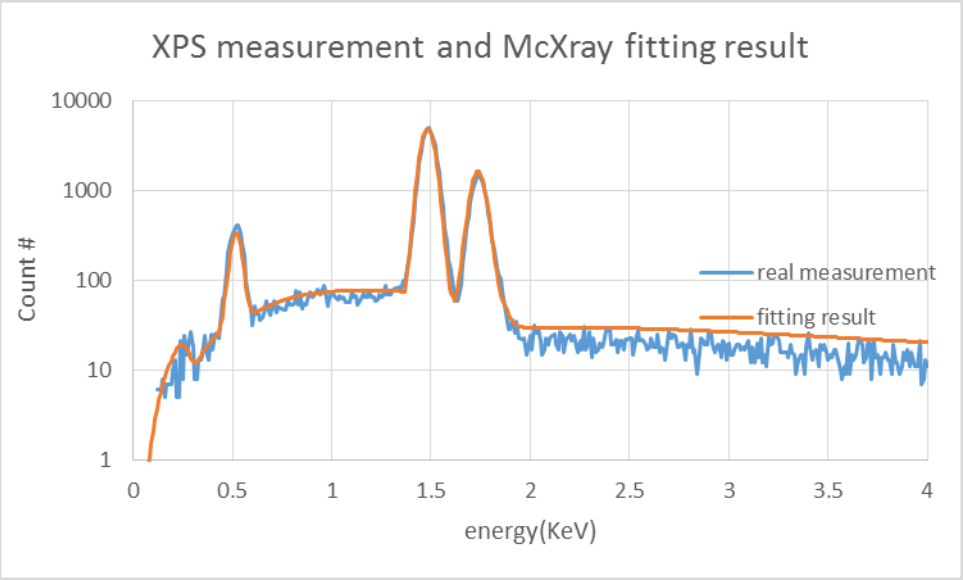

Fig. 35. Real measurement and fitting result compared at 15 keV energy

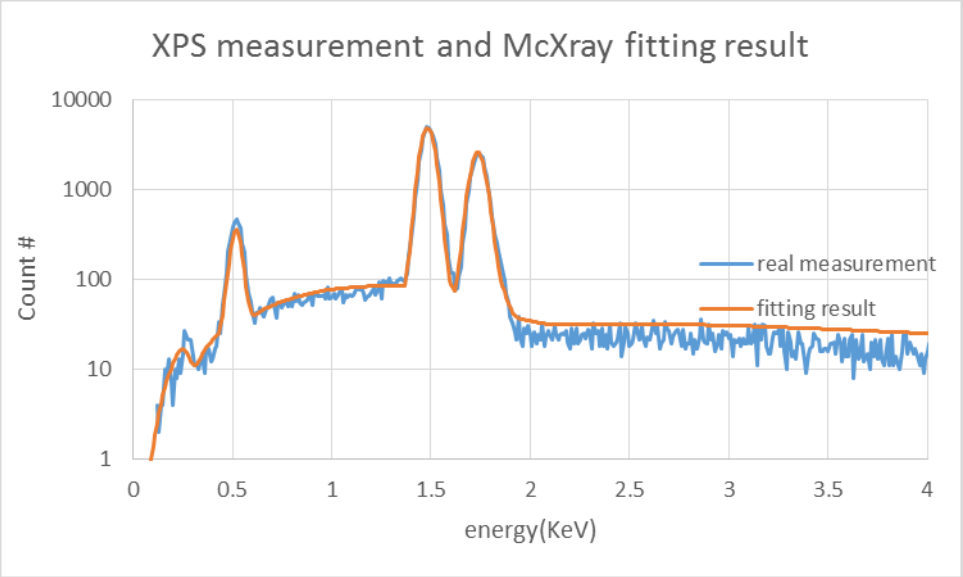

Fig. 36. Real measurement and fitting result compared at 18 keV energy

Table 15. Final model parameters of Si/SiO_2/Al substrate

First layer	Al_2O_3	40 Å
Second layer	Al	3760 Å
Third layer	SiO_2	5700 Å
Acquisition time	29.4 s	
Angle tilt	52 °	
current	8E-11 Amp	

The results presented above on the $Si/SiO_2/Al$ substrate suggests that the aluminum is covered by an Al_2O_3 layer. The Al oxide layer thickness is approximately 40A. The Al_2O_3 thickness determined from the EDAX spectra was the same for all spectra. Aluminum is known to form a thin passivation layer of approximately 30 A. [54] The thicker value we found might be due to the large roughness of our aluminum surface as observed by AFM. Below the Al layer a 570 nm thick SiO_2 layer is present.

The 10% Fe samples were deposited on $Si/SiO_2/Si_3N_4/Al$ substrates. EDAX measurements were performed on those substrates at different acceleration voltages. MCXray was used to determine the thickness of the various layers. The results are summarized in the table 16 below.

Table 16. Final model parameters of $Si/SiO_2/Si_3N_4/Al$ substrate

First layer	Al_2O_3	40 Å
Second layer	Al	1360 Å
Third layer	Si_3N_4	2500 Å
Fourth layer	SiO_2	900 Å
Acquisition time	29.4 s	
Angle tilt	52	
current	1.2E-10 Amp	

5.2.4 EDAX measurement data and data analysis of 20% O_2/19% Fe thin film

The model parameters of the substrate (Table 15) were used to model the PyO (20% O_2, 19% Fe). The parameters of the substrate were fixed, but the composition of the PyO layer, its density, and its thickness were varied. The calculated PyO thickness from the EDAX spectrum increases from 850 Å to 1550 Å when using the spectra measured at 15 kV instead of 3 kV. In additional the calculated background spectrum

is much larger than the measured background spectrum. In particularly at the very low energy side of the spectrum, the calculated and measured background spectra are very different. This difference is larger for lower acceleration voltages.

The measured concentration of Oxygen is larger for higher acceleration voltages. This suggests that the oxygen concentration varies through the film thickness and is lower near the surface of the PyO film. The detection depth increases with electron beam energy. Oxygen atoms may escape after sputtering from the top of the PyO layer. The observed density variation can be caused by the holes left behind by escaped Oxygen. This suggests that our PyO layer is not homogeneous. The measured and calculated spectra are compared in Fig. 37 to 41. The model parameters of the PyO film, i.e. thickness and concentration, are detailed in Table 17 to 20.

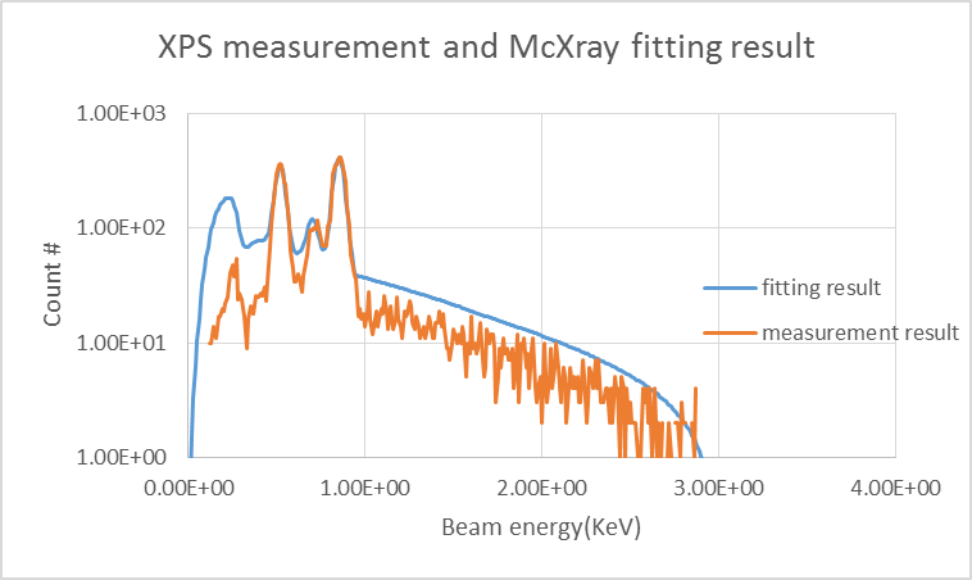

Fig. 37. Real measurement and fitting result compared at 3KeV energy

Table 17. Final model parameters of Si/SiO_2/Al/PyO sample at 3KeV beam energy

First layer: thickness, density	PyO (O/Fe/Ni 0.35/0.10/0.55)	973 Å /NA
Second layer	Al_2O_3	40 Å
Third layer	Al	3760 Å
Fourth layer	SiO_2	5700 Å
Acquisition time	29.4 s	
Angle tilt	52 °	
current	1.1E-10 Amp	

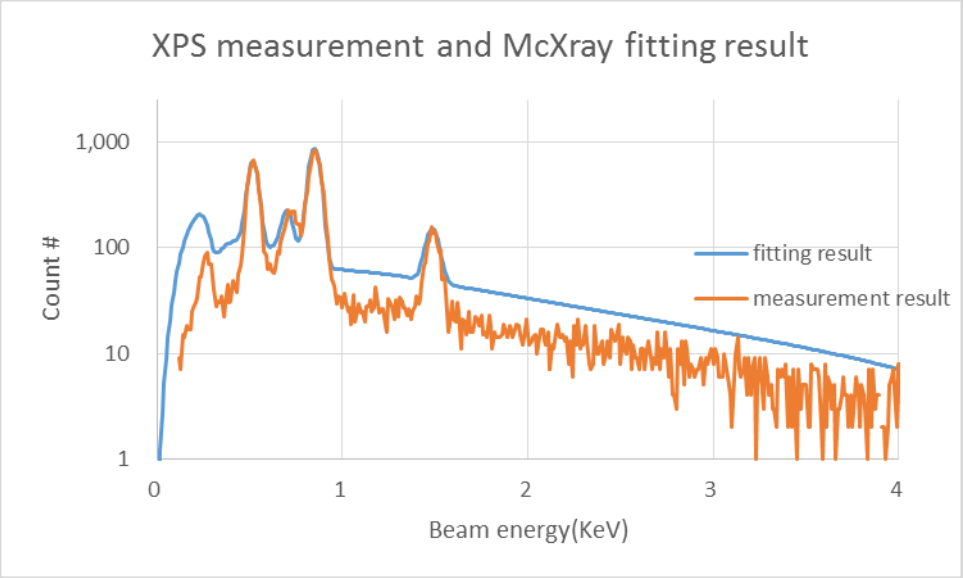

Fig. 38. Real measurement and fitting result compared at 5KeV energy

Table 18. Final model parameters of Si/SiO_2/Al/PyO sample at 5keV beam energy

First layer: thickness, density	PyO (O/Fe/Ni 0.35/0.1/0.55)	973 Å, 4.3 g/cm^3
Second layer	Al_2O_3	40 Å
Third layer	Al	3760 Å
Fourth layer	SiO_2	5700 Å
Acquisition time	29.4 s	
Angle tilt	52 °	
current	1.2E-10 Amp	

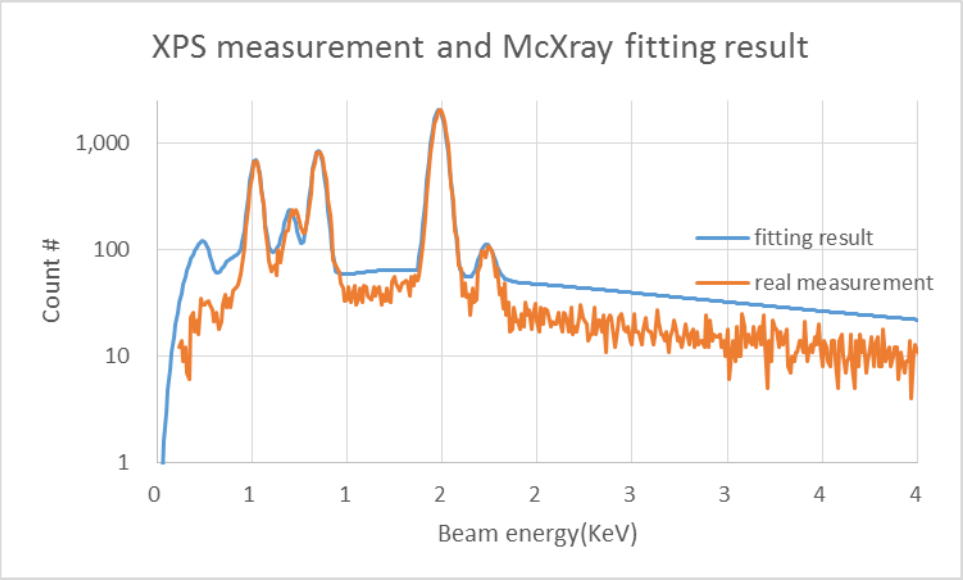

Fig. 39. Real measurement and fitting result compared at 10KeV energy

Table 19. The model detail of PyO on Si/SiO_2/Al substrate simulation at 10KeV energy

First layer: thickness, density	PyO (O/Fe/Ni 0.37/0.11/0.52)	973 Å, 5.5 g/cm^3
Second layer	Al_2O_3	40 Å
Third layer	Al	3760 Å
Fourth layer	SiO_2	5700 Å
Acquisition time	29.4 s	
Angle tilt	52 °	
current	1E-10 Amp	

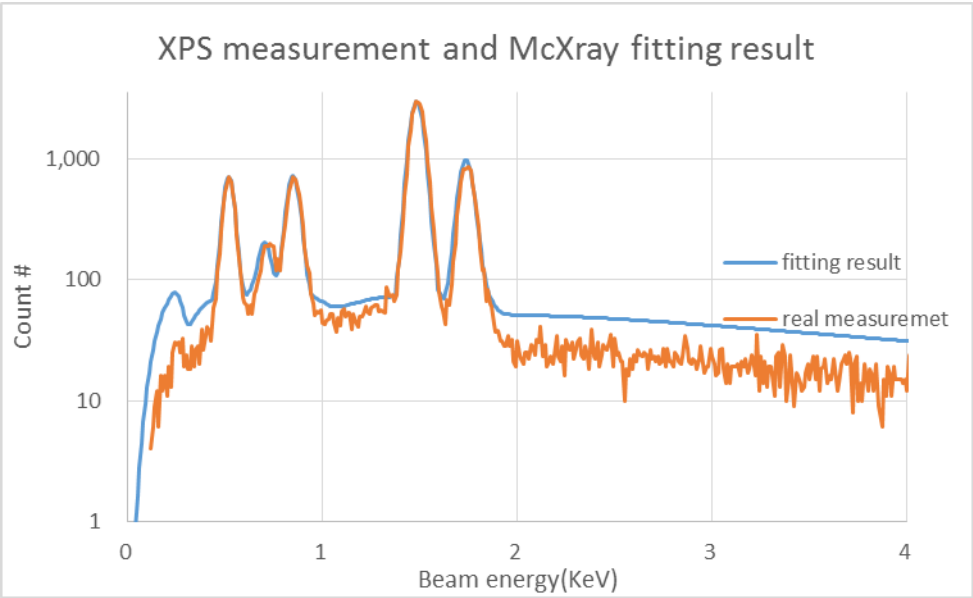

Fig. 40. Real measurement and fitting result compared at 15KeV energy

Table 20. The model detail of PyO on Si/SiO_2/Al substrate simulation at 15KeV energy

First layer: thickness, density	PyO(O/Fe/Ni 0.39/0.11/0.50)	973 Å, 5.9 g/cm^3
Second layer	Al_2O_3	40 Å
Third layer	Al	3760 Å
Fourth layer	SiO_2	5700 Å
Acquisition time	29.4 s	
Angle tilt	52 °	
current	1E-10 Amp	

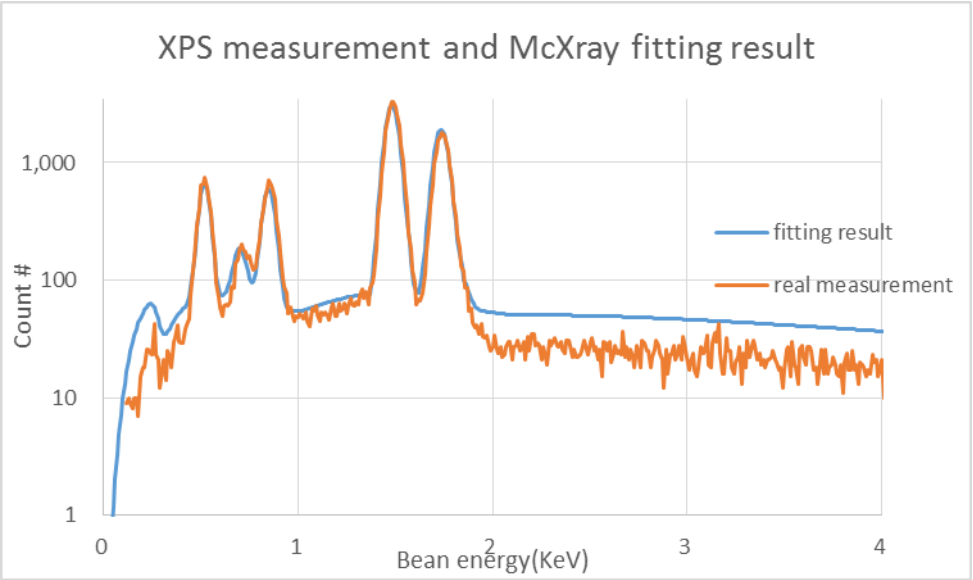

Fig. 41. Real measurement and fitting result compared at 18KeV energy

Table 21. The model detail of PyO on Al substrate simulation at 18KeV energy

First layer: thickness, density	PyO(O/Fe/Ni 0.39/0.12/0.49)	973 Å, 5.9 g/cm^3
Second layer	Al_2O_3	40 Å
Third layer	Al	3760 Å
Fourth layer	SiO_2	5700 Å
Acquisition time	29.4 s	
Angle tilt	52 °	
current	1E-10 Amp	

5.2.5 EDAX measurement Data and Data Analysis of 5% O_2/10% Fe thin film

The measured and calculated spectra of the 5% O_2 samples/ 10% Fe samples are presented in Appendix III. The estimated oxygen concentration is approximately 35%

showing that the PyO is not stoichiometric and suggesting that approximately 40-50% of the oxygen sites are empty. The standard deviation of the determined concentration was much smaller for this sample than for the 19% Fe sample. It may be because the 10% Fe concentration samples were made just before the SEM measurement and the 19% Fe series were deposited 6 months before they were measured in the SEM. The PyO film may not be stable during that time and or exposed to contamination. The top layer of the PyO shows approximately the same oxygen concentration for both Fe concentrations (measurement and simulation done at low energy). As we expected the Fe concentration changed with target concentration and the ratio of the Fe concentrations in the 19%-Fe and 10%-Fe samples are similar to the ratio of the Fe in the used targets. The spectra and detailed information can be found in Appendix III

5.2.6 EDAX measurement Data and Data Analysis of 5% O_2/19% Fe thin film

The oxygen concentration is similar to the 20% O_2 flow rate sample (0.343 to 0.35) at low beam energies. So the surface has the same concentration. We expect that the different O_2 percentage between the top and deeper parts of the films differ because of escaped O_2, so about 0.34 to 0.35 is the stable concentration of Oxygen in the deposited PyO film by our AJA system. Farther away from the surface the 5% O_2 sample has a lower oxygen concentration than the 20% O_2 sample (0.373 to 0.39). The difference is not large, but in the electrical measurement (see below) there is a significant resistance difference between them. For the spectra measured at a very

large beam energy (18KeV), the fitting is not good. The spectra and the detailed information can be found in Appendix IV

5.2.7 EDAX measurement Data and Data Analysis of 20% O_2/10% Fe thin film

The simulation of 20% O_2 samples of 10% Fe percentage. The Oxygen concentration has the same behavior as the 5% O_2 10% Fe sample: the oxygen concentration seems to be less near the PyO substrate interface. That is opposite to what was observed for the 19% Fe samples. The Oxygen concentration is higher than 5% samples only on the 5 and 10KeV energy. The Oxygen concentration changed very little with different O_2 flow rate between 5% and 20%. The spectra and the detailed information can be found in Appendix V.

5.2.8 Summary EDAX measurements

To summarize the EDAX measurements: The results for the four analyzed samples are summarized in Table 22 below. The first three columns show the percentage of Fe, Ni, and O atoms in the PyO film. The fourth column shows the number of oxygen vacancies calculated from the concentrations in the first three columns assuming that the ratio of metal atoms to oxygen atoms is 1:1. Note that according to this data only 66% of the oxygen sites is occupied by an atom [32]. Fig. 42 (left) shows the rocksalt PyO with about 33% Oxygen vacancy. The high Oxygen vacancy concentration, compared with the complete crystal structure, i.e. Fig. 42 (right), is clear from the figure. It is difficult to believe that the oxygen vacancy concentration

can be so large. Also the large Oxygen vacancy can cause a significant change of the PyO density especially for the low O_2 flow samples. The last column of Table 22 shows the percentage of metal atoms that are iron. The values in the table are the average of the values obtained from the 5, 10, 15, and 18 keV spectra. The working method of the samples made with different targets gave a different Fe-concentration in the PyO layer, as it should be. The Fe concentration was slightly lower than what we expected though in both target sample series. The Oxygen concentration increased slightly for the samples made at a larger oxygen flow rate. Calculated oxygen vacancies decrease for higher oxygen flow rates. The analysis of the EDAX data also suggests that the oxygen concentration is not constant through the thickness of the PyO. The 19% Fe samples showed more oxygen vacancies near the surface of the film and the 10% Fe samples showed fewer oxygen vacancies near the surface.

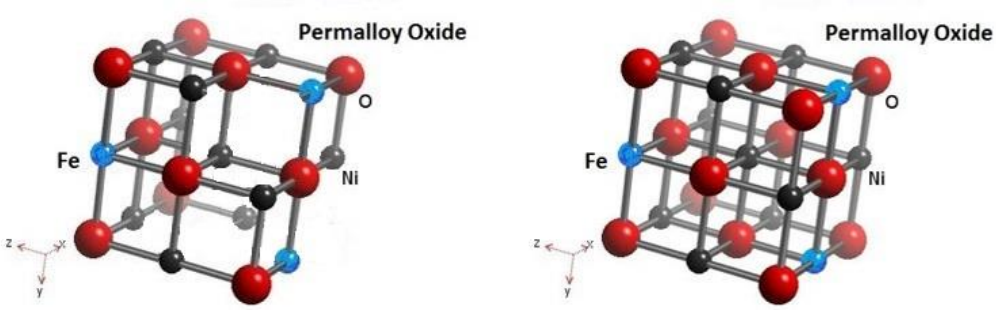

Fig. 42. Rocksalt PyO without 33% Oxygen (left), perfect Rocksalt PyO

Table 22. Summary of EDAX analysis.

	%Fe	%Ni	%O	$\%V_O$	Fe/(NiFe)
$5\%O_2$ 10% Fe	6.0	60.0	33.7	49.1	9.7
$20\%O_2$ 10%Fe	7.0	59.4	34.0	48.6	10.0
$5\%O_2$ 19%Fe	11.4	53.1	35.5	45.0	17.7
$20\%O_2$ 19%Fe	10.8	51.9	37.3	40.6	17.2

5.3 Ellipsometer measurements

The 19% Fe samples were measured by the M2000.

5.3.1 Multi-sample fit Method

A multi-sample fit technique was used to determine the PyO layer on the O_2 flow series. The optical properties of the top layer of the PyO film should be the same for all samples independent of the substrate material. Samples on different substrates were all made during the same sputter run. The multi-sample fit function in the Woollam software can be used to determine the optical properties of the same layer on different substrates from measurements performed on multiple samples. This fit technique is referred to as a multi-sample fit. Fig. 42 below shows the model used. Microscope glass, $Si/SiO_2/Al$, and Si/SiO_2 are the three substrates. Each type of substrate material is included in the model, see layer No.1, 3, 5, and 6. To simulate the interface of the PyO with the substrate, an oscillator model is included for each substrate material: layer No.2, 4, and 7. the top layer No.8 is the PyO film which optical properties are going to be determined from the fit. The thickness of different layers can be set and fitted separately for each data set as shown in the table at the bottom of Fig. 43. There are three data-set for each particular oxygen flow rate, corresponding to the data measured on the sample on microscope glass, on $Si/SiO_2/Al$, and on Si/SiO_2, i.e. data set No.1, 2, and 3. In addition, for each dataset, the thickness of the layers which are not in the corresponding sample, are set as to 0.

The following three steps were followed for the multi-sample fit:

- First, the optical properties and the thickness of different layers were roughly determined by the Cody-Lorentz oscillator model.
- Then, a wavelength by wavelength model is used to fit the optical properties with the data from the first step as the starting point.
- In the last step, the optical properties are determined by a bspline model, and the data from step two is used at the start point in the step. Also, in this step, the thickness of the mix layers are set to 0 to decrease the number of fit parameters.

Layer # 8 = Gen-Osc Thickness # 8 = 796.88 Å (MSA)
Layer # 7 = Gen-Osc Thickness # 7 = 0.00 Å (MSA)
Layer # 6 = SiO2_JAW Thickness # 6 = 0.00 Å (MSA)
Layer # 5 = Si_JAW Thickness # 5 = 0.00 Å (MSA)
Layer # 4 = Gen-Osc Thickness # 4 = 0.00 Å (MSA)
Layer # 3 = Al_nk Thickness # 3 = 0.00 Å (MSA)
Layer # 2 = Gen-Osc Thickness # 2 = 10.11 Å (MSA)
Layer # 1 = Glass Slide Thickness # 1 = 10000.00 Å (MSA)
Substrate = Glass Slide

Data Set	Thickness # 1	Thickness # 2	Thickness # 3	Thickness # 4	Thickness # 5	Thickness # 6	Thickness # 7	Thickness # 8
#1	10000.00 Å	10.11 Å	0.00 Å	0.00 Å	0.00 Å	0.00 Å	0.00 Å	796.88 Å
#2	0.00 Å	0.00 Å	10000.00 Å	22.15 Å	0.00 Å	0.00 Å	0.00 Å	789.10 Å
#3	0.00 Å	0.00 Å	0.00 Å	0.00 Å	100000000.00 Å	5056.19 Å	18.04 Å	764.41 Å

Fig. 43. Model for multi-sample fitting

5.3.2 Measurement Data and Data Analysis

The result of the fitting described in the previous section is shown below (Table 23 to Table 25). The Multi-Sample fitting for PyO on the Si/SiO_2 and the Si/SiO2/Al substrates resulted in similar thickness results for fitting with and without interface layer. The calculated thickness for the PyO on glass was very different for fitting with

or without interface layer though. The PyO thickness changed about 10% for some samples as the maximum. For the PyO sputtered at higher oxygen flow rates, the multiple-sample fit without interface layer results in similar thickness values for all substrate materials. Fig. 44. showed the ε_1 and ε_2 of the Oxygen flow rate series on the 19 at.% Fe samples. The large 2.3eV peak only showed up in the 5% O_2 flow sample. The peak may be because of the Oxygen vacancy. The SiO_2 layer thickness was also compared using multi-sample fitting, SiO_2 only fitting, and SiO_2 with PyO Horiba fitting. The result of these three fitting were similar. The result of the SiO_2 thickness and also PyO thickness can be found in the Table 25.

Table 23. B-spline Multi-Sample fit with interface layers, also fit on oxide thickness SiO_2

Sample	Glass top (Å)	Glass Middle (Å)	Al top (Å)	Al middle (Å)	Si/SiO_2 top (Å)	Si/SiO_2 Middle (Å)	MSE
0100 (5%)	799.3	10.1	793.1	22.2	756.4	18.8	17.1
0144 (7%)	781.4	21.6	794.4	14.0	798.4	14.7	24.5
1259 (10%)	699.7	19.7	783.2	27.9	773.6	43.8	20.6
0349 (14%)	706.4	10.3	771.3	22.2	771.1	29.2	22.7
0428 (20%)	728.0	11.6	777.8	9.3	779.5	27.2	13.7

Table 24. B-spline Multi-Sample fit without interface layers, and a 5100 Å oxide assumed for SiO_2.

Sample	Glass top (Å)	Al top (Å)	Si/SiO_2 top (Å)	MSE
0100 (5%)	840.1	791.2	763.7	28.7
0144 (7%)	836.7	791.8	812.10	32.10
1259 (10%)	788.6	744.7	748.3	31.3
0349 (14%)	785.0	760.3	769.4	30.3
0428 (20%)	779.9	771.8	770.6	18.1

Table 25. The thickness of SiO_2 compares with multi-sample fitting using CompleteEASE, SiO_2 fitting only and SiO_2 fitting with PyO using Horiba software

Sample	Multi-layer (Å)	PyO (Å)	MSE	SiO_2 only(Å)	MSE	SiO_2/PyO (Å)	PyO (Å)	MSE
0100 (5%)	5043.7	839.9	27.6	5074.3	65.9	5036.6	789.0	8.8
0144 (7%)	5122.7	803.7	32.7	5120.8	19.5	5115.9	782.1	17.4
1259 (10%)	5110.9	743.6	31.3	5097.1	22.8	5099.3	699.8	15.0
0349 (14%)	5110.4	765.3	30.3	5120.8	72.5	5113.0	727.3	15.9
0428 (20%)	5119.7	762.1	17.8	5111.5	27.6	5139.4	770.6	51.4

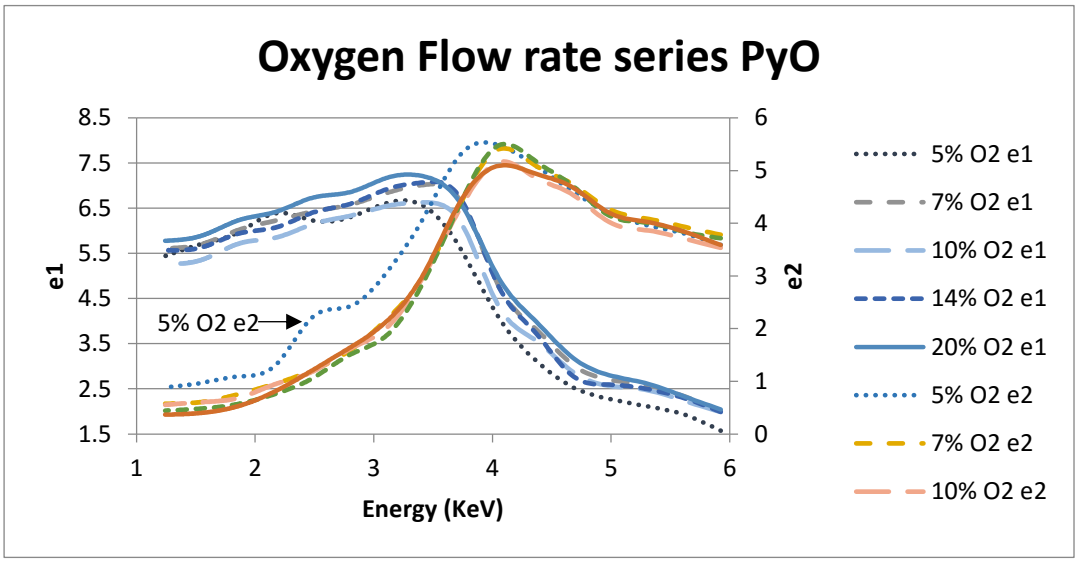

Fig. 44. Optical properties (ε_1 and ε_2) from non-interface fitting multi-sample fitting for different Oxygen flow rates

5.4 0349 AFM measurement and roughness report

5.4.1 Experimental Procedure

To determine the surface roughness of the PyO samples, a Veeco Dimension 3100 SPM/ AFM System was used. The measurement procedure and steps can be found in Chapter 2 and the Appendix VI.

5.4.2 Measurement Data / Data Analysis

All four samples (PyO on microscope glass, on $Si/SiO_2/Al$, on Si/SiO_2 and on $Si/SiO_2/Si_3N_4$ with 19% Fe 14% Oxygen flow rate) of sputter run 0349 were measured using the AFM. The roughness was determined from the AFM scans. Two functions from the software were used when analyzing the raw measurement data to get the roughness. Flatten was used to remove the offset between two scan lines. Usually, flatten was used as order 0 only to remove the Z direction offset and get a clear picture. Plane fit auto was used to level the plot and remove the tilt of the sample and the bow of the scanner by subtracting a polynomial fit of the scanned profile. The roughness was measured of the whole picture (5 μm*5 μm) and also of a small area on the left top of the picture. Fig. 44 shows the result of the PyO on a $Si/SiO_2/Si_3N_4$ substrate. Two different roughness values were determined: i.e. RMS roughness and R_a. The RMS roughness or root mean square roughness, is the square root of the average value of the square of the height difference between the real height and the average height. The R_a roughness is the average value of the absolute value of the height differences. The RMS roughness of the PyO is less than 2 nm, and the substrate's RMS roughness is about 1 nm (Fig. 44 right). The $Si/SiO_2/Al$ substrate, Fig. 45 right image, is much rougher and has an RMS roughness of 5.4 nm. The PyO on top of $Si/SiO_2/Al$ has an RMS roughness of 7 nm (see Fig. 45 on the left). Fig. 46 shows the results of the PyO on the microscope slide. About 11 months after deposition, a white layer was found on the top of PyO top layer on the microscope slide. The new layer made the sample look dull and not shiny. The RMS roughness

measured of that layer is very large, i.e. about 20 nm, see Fig. 47. After the white layer was removed with a cloth, the measured RMS roughness of substrate and PyO were respectively 6 nm and 2 nm (See also Fig. 47). Fig. 48 shows the data measured on the Si/SiO_2 sample. The left image was measured in an area covered with PyO. It has an RMS roughness smaller than 1 nm. The right image shows the surface of just the substrate. It is very smooth and has a smaller RMS roughness than the PyO film.

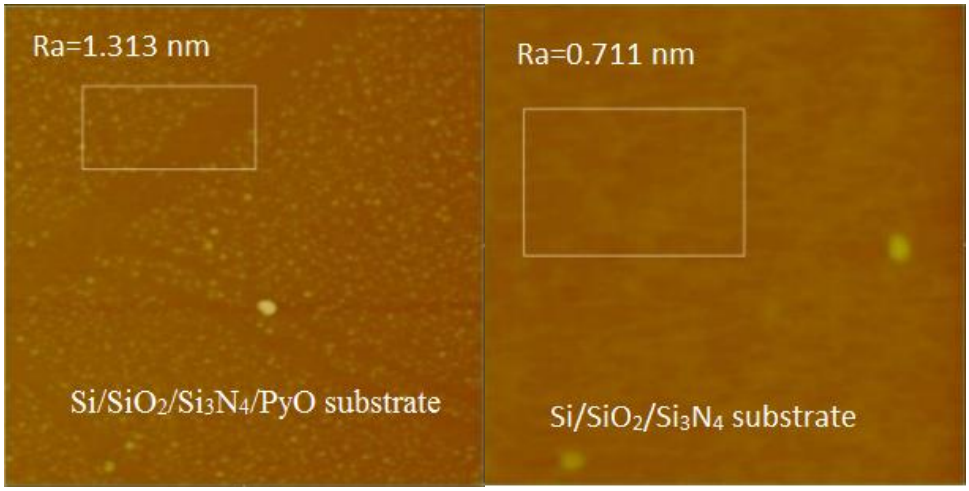

Fig. 45. $Si/SiO_2/Si_3N_4$/PyO 19% Fe film (left) and substrate (right)

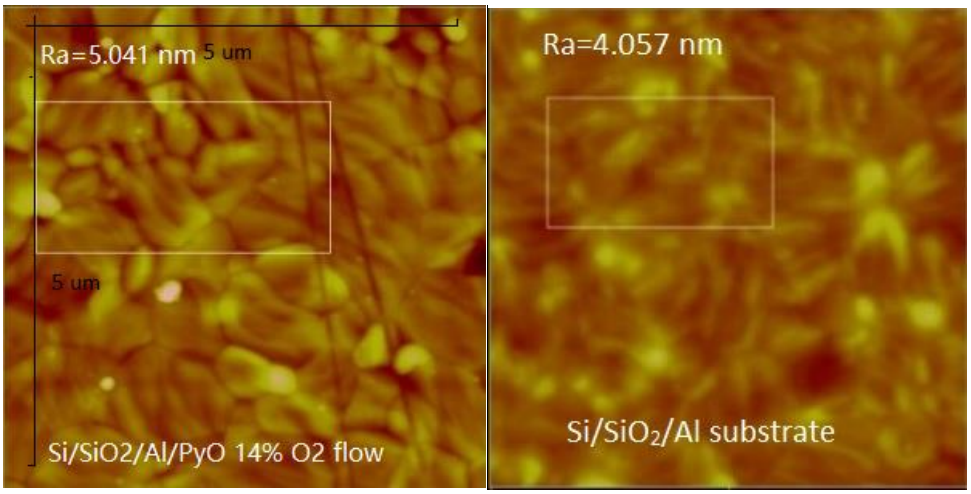

Fig. 46. Si/SiO_2/Al/PyO film (left) and substrate (right)

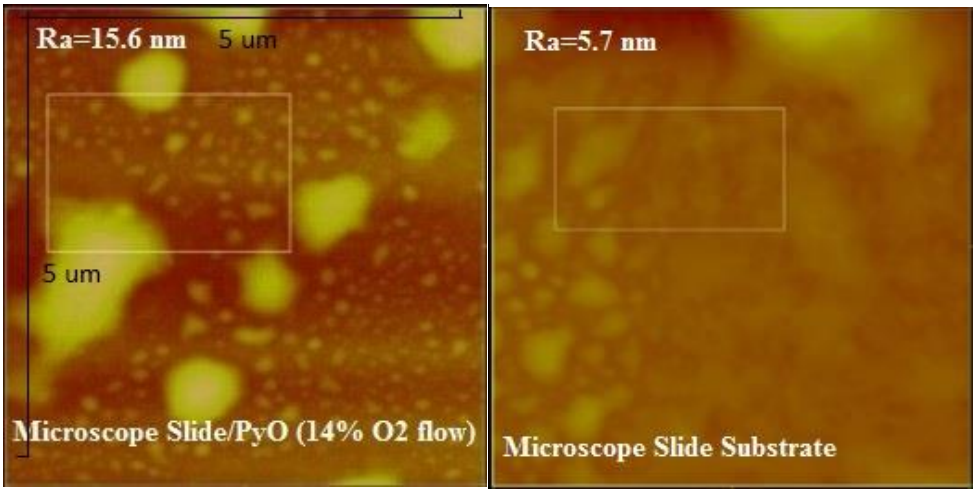

Fig. 47. Microscope slide/PyO before clean

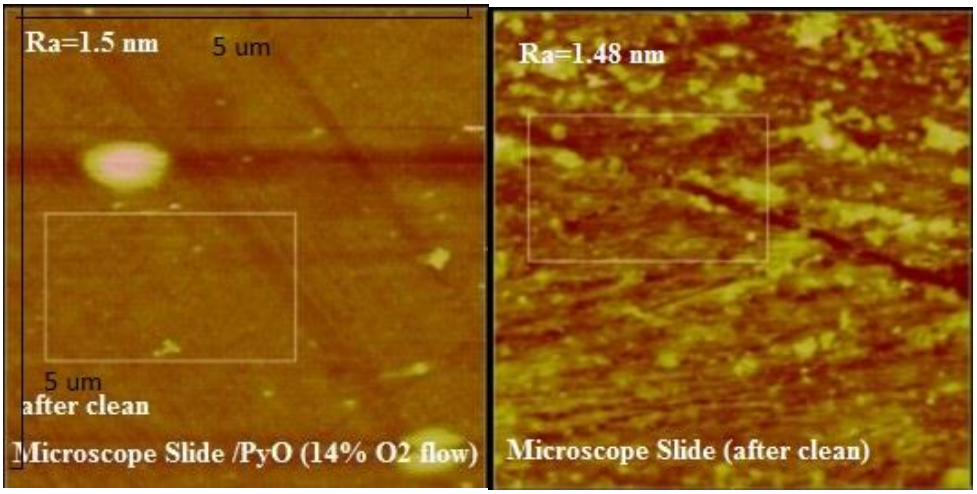

Fig. 48. Microscope slide/PyO film after clean (left) and substrate (right)

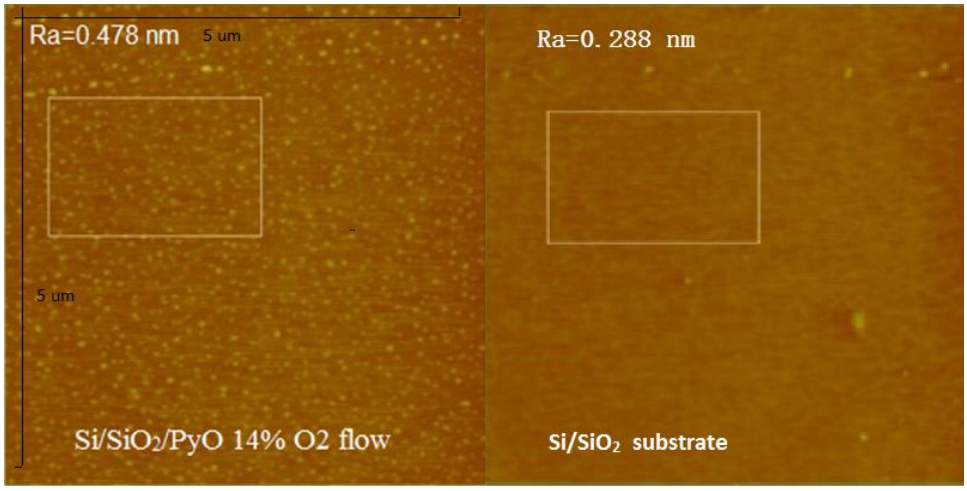

Fig. 49. Si/SiO_2/PyO film (left) and substrate (right)

5.4.3 Summary AFM measurements

Table 26 shows all of the RMS roughness values measured on the samples. The top layer, which is PyO, has a larger roughness than its substrate. The PyO on the microscope glass slide had a large roughness approximately 1.5 years after deposition. After cleaning, the roughness of those samples is smaller than the roughness of the PyO on the $Si/SiO_2/Al$ substrate. The PyO on $Si/SiO_2/Al$ substrates had the second largest roughness of these 4 samples. Both the Si/SiO_2 and $Si/SiO_2/Si_3N_4$ samples are very smooth. The PyO on Si/SiO_2 has half the RMS roughness of the PyO on $Si/SiO_2/Si_3N_4$. At this moment, it is not clear where the white layer is coming from. Chemical analysis in the SEM could reveal the composition of the particles.

Table 26. AFM roughness of PyO (19% Fe) samples with 14% O2 flow and substrates in nm (Rq and Ra)

Sample	$Si/SiO_2/SiN$		$Si/SiO_2/Al$		glass before clean		glass after clean		Si/SiO_2	
Roughness	R_q	R_a	R_q	R_a	R_q	R_a	R_q	R_a	R_q	R_a
Whole PyO	1.9	1.3	7.0	5.0	22.3	15.6	6.0	2.8	0.68	0.48
Small area PyO	1.6	1.1	6.6	4.9	19.1	14.3	2.4	1.5	0.62	0.44
Whole substrate	1.03	0.71	5.4	4.0	18.5	11.0	2.2	1.6	0.40	0.289
Small area	0.71	0.57	4.1	3.2	7.4	5.7	2.0	1.5	0.26	0.21

5.5 Electrical Properties

5.5.1 4pp measurement on the Oxygen flow rate sample

The resistivity of the samples was measured as a function of the oxygen flow rate using the linear 4pp setup.

5.5.2. Measurement Results and Data Analysis

The measured voltage and currents were converted into the sheet resistance. The film thickness measured by ellipsometry was used to convert the sheet resistance to a resistivity. The resistivity increased as a function of the Oxygen flow for the 19 at. % Fe samples. The 10 at. % Fe series had a similar behavior although the 14% O_2 flow sample behaved different. The results are summarized in Fig. 50. The resistivity of the 20% oxygen flow samples is similar to the resistivity of dual ion beam sputtered PyO samples [6].

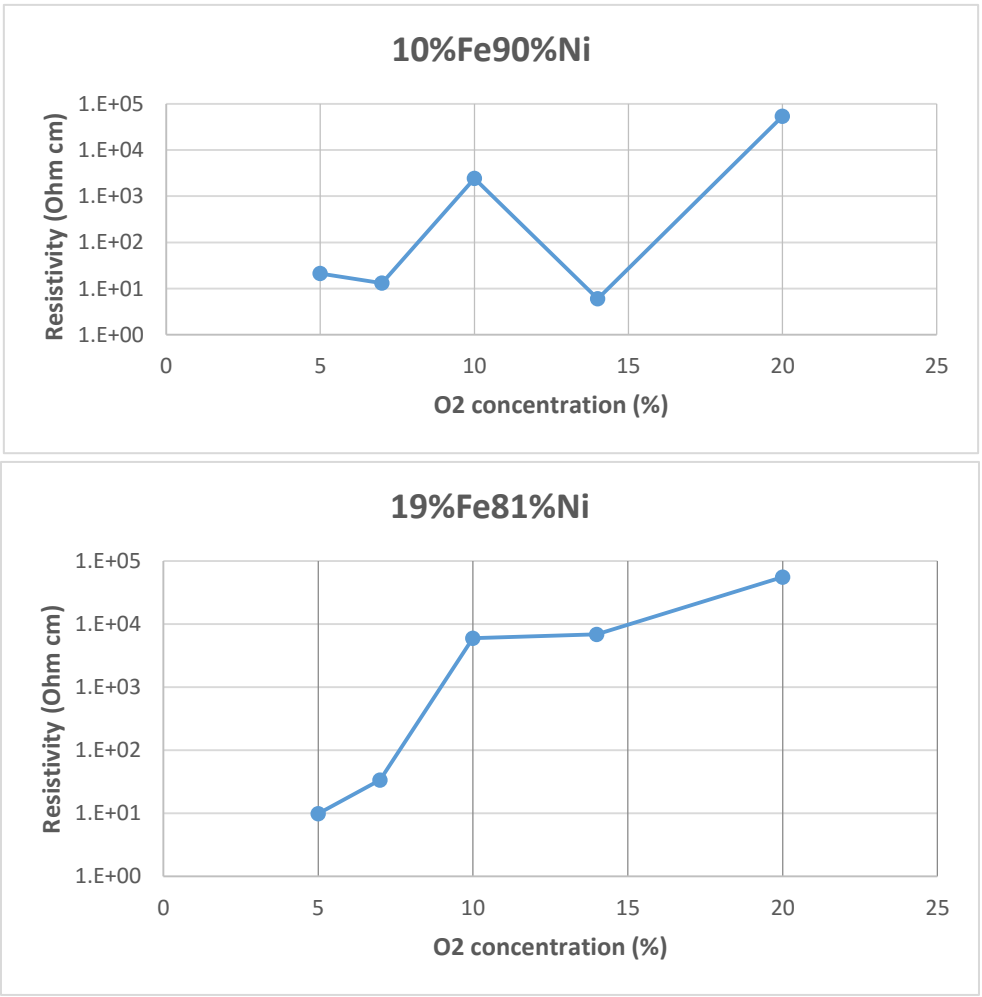

Fig. 50. Resistivity as a function of oxygen flow rate

Fig. 51 below shows the PyO structure with different O vacancy concentration. A represents a metal atom i.e. an Fe or Ni atom. O represents an Oxygen atom, and V represents an O vacancy. In the left figure only 3 out of 8 of the oxygen atoms is missing. If one assumes that one of the metal atoms that neighbors an oxygen vacancy, no conducting path is formed from the top to the bottom of the crystal. if half of O was missing a metal path can be formed. But if there were only 3 out of 8 O missing the metal conductive path cannot be formed. So a low O_2 flow rate can lead to a low resistivity in the PyO thin film. It is expected that above a certain oxygen vacancy concentration the resistivity suddenly drops significantly as a function of oxygen flow rate. This is exactly what is observed (see Fig. 50).

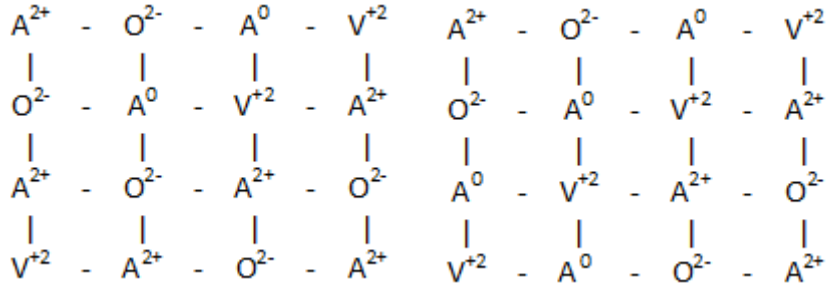

Fig. 51. PyO with different O_2 vacancy percentage

5.6 Summary

The composition of the films was determined from EDAX measurements. The ratio of Ni to Fe atoms in the films was close to the target values. The concentration of oxygen atoms was much lower than the expected value based on the rocksalt crystal

structure. From EDAX measurements it is estimated that roughly 60% of the oxygen sites is occupied [32]. This number is believed to be too low. The preferential absorption of low energy photons by the window of the EDAX detector and/or issues with not being able to correctly model the bremsstrahlung spectrum might be causing the large estimated oxygen vacancy concentration. Better results can be obtained if a stochiometric NiO calibration sample would be available.

Films deposited at higher oxygen flow rates have a higher oxygen concentration. The Oxygen concentration is expected to influence the switching behavior of RRAM Devices. The more oxide in the film, the larger the measured resistivity which confirms the low oxygen concentration in our films. It is expected that the switching will be impacted by the oxygen concentration. A low oxygen concentration will result in a lower resistivity of the high resistance state. On the other hand, a lower Oxygen vacancy concentration can also lower the resistivity of the low resistance state, and influence the RRAM performance. The model used to explain the switching behavior of RRAM is based on the vacancy free path, so oxygen vacancy concentration is important. A future study is needed to find out a good O_2 flow rate for the deposition of PyO. So switching properties of the flow rate devices are optimized. Such study should include measurement of the resistivity perpendicular to the film surface. Note that all resistivity values reported in this thesis are measured by linear 4pp, and indicate values parallel to the substrate.

The optical spectra of the films sputtered at lower oxygen flow rate show a more pronounced peak at low photon energy in the ε_2 spectrums. This is in agreement

with the measurements done on the temperature series. As the low energy peak was very large for the films made at low O_2 flow rate, this peak can be used to detect if a thin PyO layer is in a low resistance state or in a high resistance state. The ellipsometer measurement is very quickly and easily to determine the optical properties. This method might allow for a method to detect the resistance state of the film without needing an electrode layer on the top of the sample.

VI. SUMMARY

The growth and properties of RF-sputtered $Ni_xFe_{1-x}O_\delta$ deposited at low pressure were studied in this thesis for possible application in RRAM devices. The following conclusions are made:

1. The normal cleaning procedure for the substrates that is 5 minutes in a sonicator using water, acetone, and isopropyl alcohol is not perfect. A thin layer with a refraction index larger than fused silica was observed with ellipsometry. The cleaning procedure can be improved by implementing an ozone or plasma clean. Such step reduces the refraction index of the surface layer by a factor two. Heating the sample before deposition in the vacuum chamber can further improve the substrate preparation process. A study needs to be performed to see if those substrate preparation steps are compatible with the liftoff lithography process. Clean interfaces are very important when studying RRAM devices, in particularly RRAM devices that show bipolar switching.
2. The roughing of the back of the substrates with the sandblaster for 30 seconds allows for ellipsometric measurements without polarized back-reflection over a wide spectral range (0.03-6 eV). PyO films on a roughened substrate show a lower MSE than PyO films measured with a scotch tape on the back. The samples, however, can no longer be used for transmission measurements. We need a method to partly roughen the back of the substrates.
3. The optical properties of PyO in the infrared can be described by a Lorentzian

peak between 377-384 cm^{-1}. We assign this peak to the phonon of rocksalt PyO. This result confirms that RF-sputtered PyO has the rocksalt structure similar to NiO in agreement with Xray powder diffraction measurements of others. This is an important result as the rocksalt crystal structure in NiO and CoO has been shown to allow for reproducible resistive switching.

4. The EDAX simulation and measurements estimate the atomic concentration of oxygen in the RF-sputtered PyO is between 30-40% and can be varied by changing the flow rate during the deposition. Assuming rocksalt crystal structure only 50-60% of the oxygen sides is occupied. Similar results were obtained for $Ni_{90}Fe_{10}O_{\delta}$ films. The oxygen vacancy concentration estimated of the EDAX data is believed to be too high as X-ray 2θ scans show diffraction peaks. Future analysis should include measurements on stoichiometric NiO and FeO calibration samples. A better understanding of the Bremsstrahlung spectrum of our samples is necessary. Among the deposition parameters studied in this thesis, it is believed that the oxygen flow rate is most important for RRAM devices.
5. All our samples show peaks in the ε_2 spectra below 4.5 eV. The peak is very large for PyO films sputtered at 600^{o}Celsius on glass substrates but lower for similar PyO films sputtered on Si/SiO_2 wafers, suggesting the glass changes at such high temperatures. The low energy peak is also larger for samples made at low Oxygen flow rate. It is believed that the reduction of the oxide at the higher temperatures and/or incomplete oxidation are responsible for the low energy peak. This is consistent with the work of others [33]. This result suggests that we might be

able to determine the resistance state from the optical properties. This could be useful when studying switching behavior in devices. The behavior of the low energy peak is shown in Fig. 19 and Fig. 50 and was recently confirmed by DFT calculations [32].

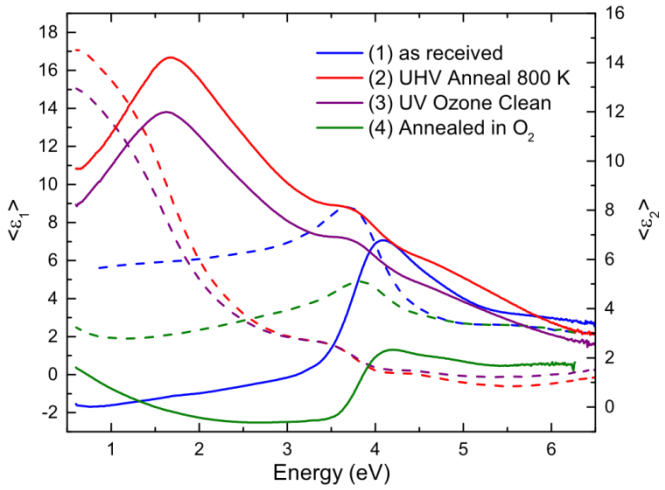

Fig. 52. NiO low energy peak with different conditions [33]

6. Fitting of only the ellipsometric data of PyO films on glass results in peaks that are not in agreement with the transmission spectra. A better understanding of this fit problem is necessary.
7. Measurements done on a thickness series of PyO samples showed that the PyO samples are not homogeneously through the film thickness. The resistivity and the optical properties vary as a function of the film thickness. In addition, the samples might be anisotropic as shown by the ellipsometer fitting result. This is consistent with the results of others on NiO. It is believed that this inhomogeneity is not a problem when applying PyO in RRAM devices.
8. RRAM device wafers were made for NiO, $Ni_{0.81}Fe_{0.19}O_{1-\delta}$, and $Ni_{0.9}Fe_{0.1}O_{1-\delta}$ using

20% oxygen flow during deposition. The results are summarized in appendix VI. The produced devices showed a non-linear IV relation with hysteresis. Although memory switching was observed, it is not clear whether the resistive switching originated from a charge effect at the electrode-oxide interface or was caused by the the oxidation/reduction of a conducting filament. Several points were found during the process of making RRAM devices that need to be improved. The first was the low deposition rate of TiN. A 0.1 Å/s deposition rate is not good enough to make a 100 nm layer. The second was that a rim was found at the edge of each layer of the RRAM memory cell. These so-called litho-ears are due to the deposition on the side walls of the photoresist. The thickness of the photoresist is too large making it difficult to remove the thin film material deposited on the side walls of the resist. The third problem identified was a large series resistance in the 2pp measurement on some of the test structures. Special probes with two electrodes need to be used in the future for the characterization of these test structures. These problems first need to be solved before the resistivity perpendicular to the substrates and the switching properties can be studied.

APPENDIX SECTION

I.Deposition procedure

II.The procedure of the AFM measurement

III.The simulation of 5% O2 samples of 10% Fe

IV.The simulation of 5% O2 samples of 19% Fe

V.The simulation of 20% O2 samples of 10% Fe

VI. RRAM DEVICE TEST WAFERS

VII.electrical measurement result detail on the real RRAM device

VIII.SiO2 optical properties and simulation fitting

I.Deposition procedure

A standard operating procedure below is how to use the system

1. Check if the spindle is in the load-lock system. If not transfer the spindle from the chamber to the load-lock system following the procedure outlined below.
2. Make sure the high vacuum valve is closed. The screw is not visible (turn clockwise to close). Switch off the ion gauge (high vacuum gauge).
3. Switch off the power to the pumps of the load-lock system. On the main rack at the top right.
4. Watch the pressure in the load-lock system. Double check that the pressure in the chamber does not rise. If it rises, make sure to stop the venting process (check with Casey). This means that the valve between the loadlock system and the vacuum chamber is not completely closed or has something in between its seal which prevents it from being vacuum tight.
5. One the load-lock system is at atmospheric pressure, lift the lit and place it on the three bumps under the load-lock system.
6. Remove the spindle and place it on a tissue. Mount your sample. Only use the provided screws. Do not use standard stainless steel screws since that will damage the Mo spindle.
7. Place the spindle with the samples upside down on the fork. Make sure that two of the screws are lined up between the teeth of the fork.
8. Clean the gasket and the lit with a wipe with IPA. Make sure no particles are on the lit and the vacuum ring.

9. Close and center the lit.

10. Switch on the pump of the load-lock at the right top of the rack. Monitor the pressure of the load-lock. It should go down to the 10^{-5} Torr range within a couple of minutes. If not, readjust the lit.

11. Once the load-lock is back in the 10^{-6} Torr range switch on the ion gauge in the main chamber.

12. Once the load-lock pressure is within a factor 10 of the vacuum chamber pressure, you can open the high vacuum valve and load the sample. Before you do so make sure that the claw is raised, i.e. the mechanical translator on top of the vacuum system is below position 25 (sputter and transfer position). Slide the rod/fork carefully into the vacuum chamber. Move it all the way to the stop (black ring).

13. Lower the claw by moving the mechanical translation stage to position 40. Make sure that the fork/rod does not move away from the stop. The claw needs to get into the hole in the middle of the spindle. Look through the window as the claw approaches the spindle. Once in place, lock the claw in place by rotating the sample-rotator at the top of the vacuum system clockwise.

14. If locked move the mechanical translator back to a position below 25. Now remove the fork/rod carefully, and close the high vacuum valve.

15. Pump down the chamber until the pressure in the chamber is back to the $3*10^{-7}$ Torr range before starting the sputtering process.

DC deposition:

1. Switch off the ion gauge. Set the substrate temperature following the direction provided below if you decide to sputter above room temperature. Set the rotation of the spindle to 60 rotations per minute (at least one rotation per monolayer). Switch on the throttle. Set the Ar flow to 10-80 sccm, and turn the gas on. Check the capacitance gauge until chamber pressure is constant. You should be able to start a dc-gun with 4-5 mTorr.
2. Set time to 0 and power to 10%, but don't turn the gun on.
3. Turn the gun on in the software. Once the plasma is started, a purple indicator will light up on the program.
4. Check through the vacuum window if the gun is indeed on. Now set the power to what you need for deposition, make sure to set the total ramp time first so that the power increase per second is not more than 1 watt per second.
5. When the set-point power is reached, pre-sputter for 30 seconds.
6. Open the shutter to start the deposition process by clicking the big button in the program. Time your deposition. Do not deposit for more than 600 seconds.
7. Click the big button again to stop the sputtering.
8. Reduce the power of the gun by setting first the time interval to the used power and then setting the power to 0%.
9. Turn off the gas after this step.
10. If you want to make a thicker film, cool the gun for 5 minutes and restart the deposition process.

11. Once you are done, stop the sample rotation, and switch off the substrate heater.

12. If the sample temperature is back to room temperature, remove the sample from the sputter chamber following the opposite of the loading process described above.

RF deposition:

1. Switch off the ion gauge. Set the substrate temperature following the direction provided below if you decide to sputter above room temperature. Set the rotation of the spindle to 60 rotations per minute (at least one rotation per monolayer).

2. Set Ar flow to 5 sccm and turn the gas on. Set time to 0 and power to 10%, but don't switch the gun on.

3. Close the high vacuum valve to the turbo pump, and check the gauge. Wait until the chamber pressure reaches up to $2.5*10^{-2}$ Torr. Turn the gun on and switch back to throttle. Check if there is a plasma in the gun, i.e. a purple light glow is visible when looking through the vacuum chamber window. If not repeat step 2 at a little higher pressure. Under no condition let the chamber pressure rise above 50 mTorr.

4. When the gun is lighted and the chamber is throttled the change the gas flow to the desired values in small steps. The plasma should stay on. Check through the vacuum window that the gun is indeed on.

5. Now set the power to what you need for deposition, make sure to set the ramp time first, so the rate increase of power to the gun is not more than 1 watt per

second. Then set the power to its end point value.

6. When the set-point power is reached, pre-sputter for 30 seconds.

7. Open the shutter to start the deposition process by clicking the big button in the program. Time your deposition. Do not deposit for more than 600 seconds.

8. Click the big button again to stop the sputtering.

9. Reduce the power of the gun to 10% of the max power by first setting the ramp down time interval, so the rate with which the power is decreased to the gun is not more than 1Watt/second. During the ramp down change the gas flow to 5 sccm in steps.

10. Turn off the gas after this step.

11. If you want to make a thicker film, cool the gun for 5 minutes and restart the deposition process.

12. Once you are done, stop the sample rotation, and switch off the substrate heater.

13. If the sample temperature is back to room temperature, remove the sample from the sputter chamber following the opposite of the loading process.

<u>Unload:</u>

1. Turn the ion gauge on to check chamber pressure. If it in the same range (within a factor 10) as load-lock, open the high vacuum valve between chamber and sample load-lock holder.

2. Make sure that the claw and spindle are up, i.e. below position 25. Slide the

rod/fork carefully into the vacuum chamber. Move the rod/fork all the way to the stop, i.e. black ring on the rod.

3. Once the fork is at the position of the sample-holder, lower the spindle onto the fork (position 40). Turn it counter-clockwise to unlock the spindle from the claw.

16. Once in place lift the claw up by moving the mechanical translator to a position below 25. Carefully remove the fork, and close the high vacuum valve.

17. Switch off the power to the pumps of the load-lock system.

18. Watch the pressure in the load-lock system go up.

19. When the load-lock system is at atmospheric pressure, lift the lit and place it on the three bumps under the load-lock system.

20. Remove the sample from the sample-holder.

<u>The main chamber open and pump down:</u>

The procedure to vent or pump-down the chamber is used when opening the main chamber which is required if one wants to change the targets or clean the guns or if one needs to replace the quartz crystal sensor of the thickness monitor on the top of the chamber.

<u>Venting process:</u> The ion gauge needs to be switched off during the venting process. Before switching off both turbo pumps the high vacuum valve between the main chamber and turbo pump needs to be opened and the high vacuum valve between the main chamber and load-lock needs to be closed. Then turn off both turbo-pump by turning the power switch off. The pumps will slow down, and the pressure of the

main chamber will slowly rise. Release the screw that locks the top lit of the main chamber. Vent the main chamber with Ar gas by opening the Ar valve on the left of the main chamber (near on bottom). The top gate of the main chamber will pop up automatically after the vent processing.

Pump down the process of the main chamber: after maintenance is performed inside the vacuum chamber, the main chamber needs to be pumped down. Before closing the vacuum chamber, the surface of the main chamber needs to be wiped with isopropyl alcohol. Then the lit of the vacuum chamber needs to be closed. Before doing so wipe the flanges on the lit and the chamber and inspect they are clean. Then close the lit and tighten it with the screw. To pump down the main chamber and load-lock turn the power on. Both pumping units will pump down both the main chamber and the load-lock automatically. The process usually takes several hours before the main chamber reaches a pressure in the 10^{-7} Torr range. The load-lock will pump-down fast, so the high vacuum valve between the load-lock and the vacuum chamber needs to stay closed during the process.

II.The procedure of the AFM measurement

1. A tip was loaded in the instrument. The following tips were used: NSC14/AL BS tip.
2. For the scanning mode, the tapping mode was selected.
3. The screws on the top of the scanner were used to align the laser. Alignment is obtained by maximizing the sum signal. A zig-zag approach towards the tip as indicated in Fig. 51 below was followed. After maximizing, the signal is lowered to 2V by rotating the most right knob counter clockwise.

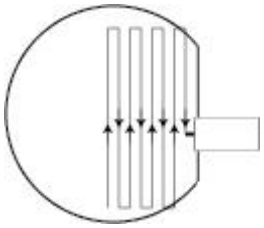

Fig. 53. Scanning path of AFM to find right tip position

4. The screws on the left side of the scanner were used to adjust the position of the reflected laser beam on the four quadrant detector. For the tapping mode, the vertical deflection was decreased to 0.
5. In order to teach the system, the position of the tip relative to the surface of the sample one needs first to focus on the tip and then focus on the surface of the sample. The tip was located from the tip location menu. The tip was brought in focus by holding down the left trackball button and rolling the trackball. Prior to doing the zoom out, feature was used. The knobs on the far left were used to center the position of the tip in the field of view of the camera.

6. The cantilever was tuned by pushing the tune icon, adjusting the tune parameters, and selecting auto tune. For our tips, the resonance frequency should be around 170 Hz. A peak offset of 5% is used.
7. The surface of the sample was found under the microscope by clicking the focus surface icon. First, a zoom out was performed, and the illumination was adjusted. Then the z-stage was adjusted by pushing the left trackball button and rolling the trackball. The trackball was moved to the stage, and the distance between the sample and the tip stage was observed while adjusting the z-stage height. At the same time, the image on the screen was monitored. Once focus was obtained in the zoom out state, a zoom in was performed, and the focus was optimized.
8. The measurements parameters were decided and entered before the tip was engaged: the integral gain was set to 0.5, and the proportional gain to 0.7. Then the engage icon was clicked. The setpoint was decreased 20% after the tip had approached the surface. During the scanning, the four parameters, i.e. integral gain, proportional gain, scan speed, and setpoint were changed to make two scanning results from a different direction close to each other.

III.The simulation of 5% O_2 samples of 10% Fe

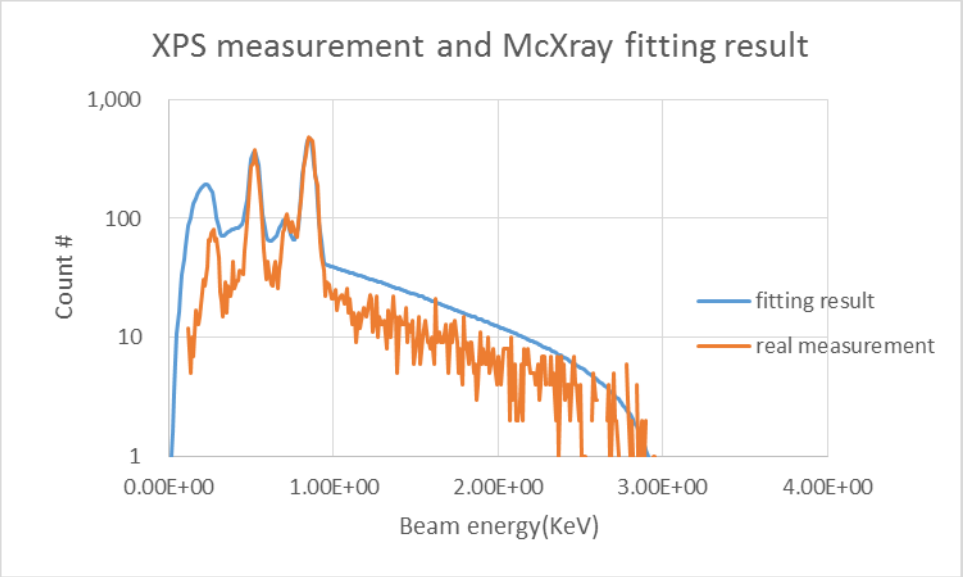

Fig. 54. Real measurement and fitting result compared at 3 keV energy

Table 27. The model detail of PyO on Si/SiO_2/Si_3N_4/Al substrate simulation at 3 keV energy

First layer: thickness, density	PyO (O/Fe/Ni 0.34/0.06/0.6)	1122 Å, NA
Second layer	Al_2O_3	40 Å
Third layer	Al	1360 Å
Forth layer	Si_3N_4	2500 Å
Fifth layer	SiO_2	900 Å
Acquisition time	29.4 s	
Angle tilt	52 °	
current	1.2E-10 Amp	

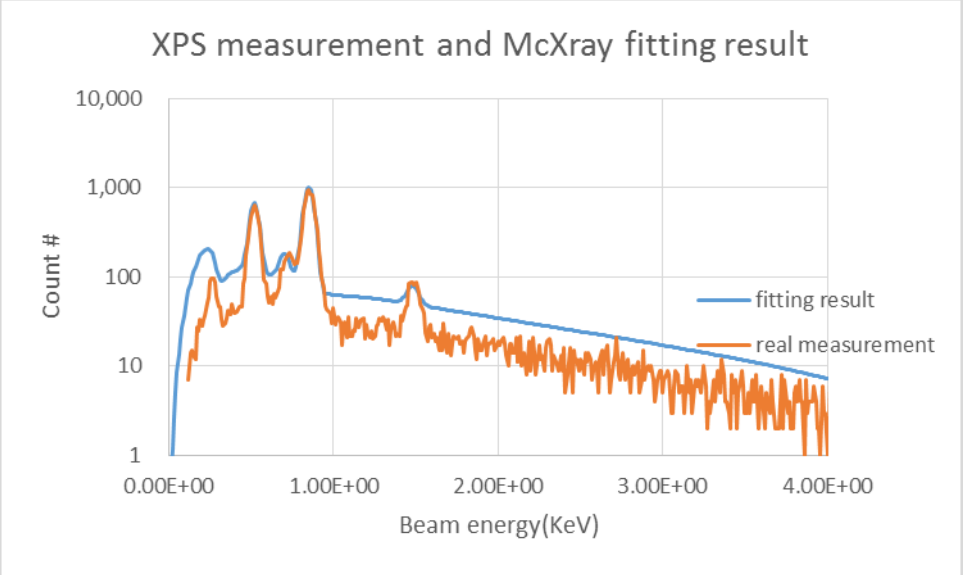

Fig. 55. Real measurement and fitting result compared at 5 keV energy

Table 28. The model detail of PyO on Si/SiO_2/Si_3N_4/Al substrate simulation at 5 keV energy

First layer: thickness, density	PyO (O/Fe/Ni 0.34/0.06/0.6)	1122 Å, 4.7 g/cm^3
Second layer	Al_2O_3	40 Å
Third layer	Al	1360 Å
Fourth layer	Si_3N_4	2500 Å
Fifth layer	SiO_2	900 Å
Acquisition time	29.4 s	
Angle tilt	52 °	
current	1.2E-10 Amp	

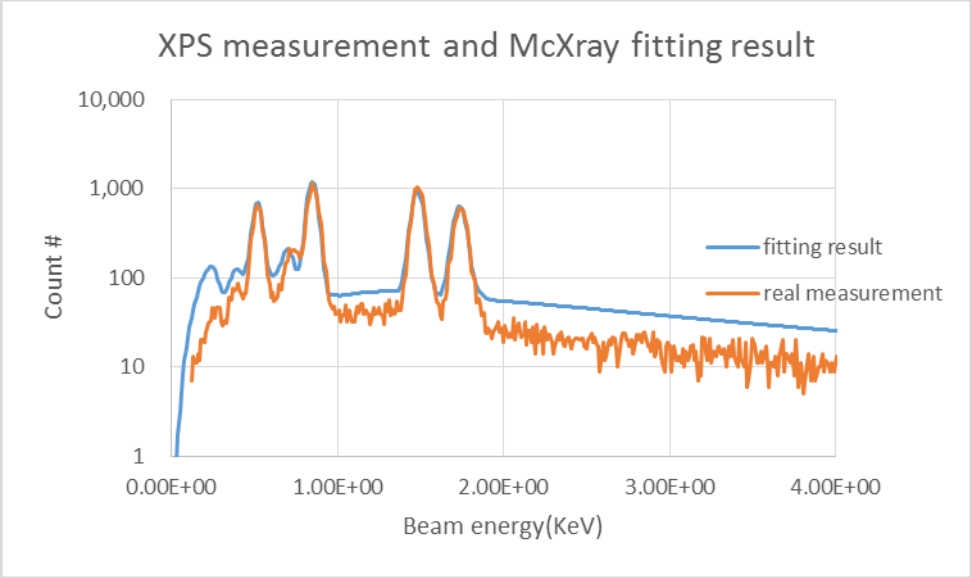

Fig. 56. Real measurement and fitting result compared at 10 keV energy

Table 29. The model detail of PyO on Si/SiO_2/Si_3N_4/Al substrate simulation at 10 keV energy

First layer: thickness, density	PyO (O/Fe/Ni 0.334/0.063/0.603)	1122 Å, 5.6 g/cm^3
Second layer	Al_2O_3	40 Å
Third layer	Al	1360 Å
Fourth layer	Si_3N_4	2500 Å
Fifth layer	SiO_2	900 Å
Acquisition time	29.4 s	
Angle tilt	52 °	
current	1.2E-10 Amp	

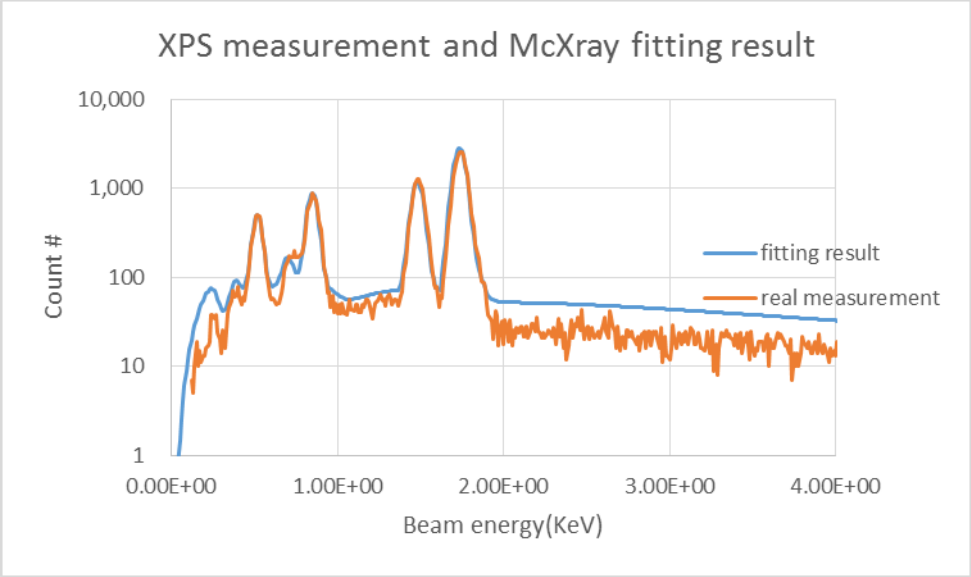

Fig. 57. Real measurement and fitting result compared at 15 keV energy

Table 30. The model detail of PyO on Si/SiO_2/Si_3N_4/Al substrate simulation at 15 keV energy

First layer: thickness, density	PyO (O/Fe/Ni 0.33/0.07/0.6)	1122 5.9g/cm^3
Second layer	Al_2O_3	40 Å
Third layer	Al	1360 Å
Fourth layer	Si_3N_4	2500 Å
Fifth layer	SiO_2	900 Å
Acquisition time	29.4 s	
Angle tilt	52 °	
current	1.2E-10 Amp	

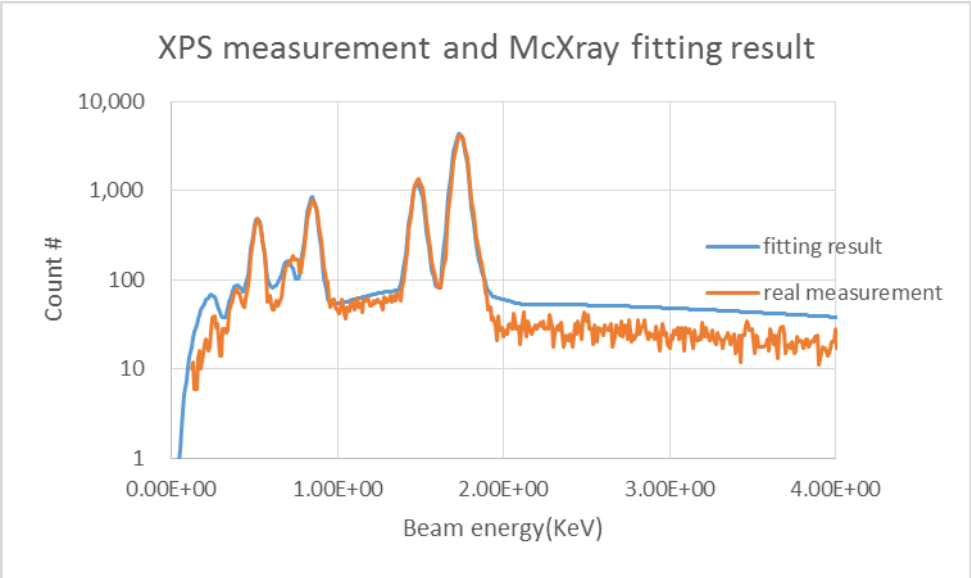

Fig. 58. Real measurement and fitting result compared at 18 keV energy

Table 31. The model detail of PyO on Si/SiO_2/Si_3N_4/Al substrate simulation at 18 keV energy

First layer: thickness, density	PyO (O/Fe/Ni 0.33/0.07/0.6)	1122 Å, 6.0 g/cm^3
Second layer	Al_2O_3	40 Å
Third layer	Al	1360 Å
Fourth layer	Si_3N_4	2500 Å
Fifth layer	SiO_2	900 Å
Acquisition time	29.4 s	
Angle tilt	52 ^{o}	
current	1.2E-10 Amp	

IV.The simulation of 5% O_2 samples of 19% Fe

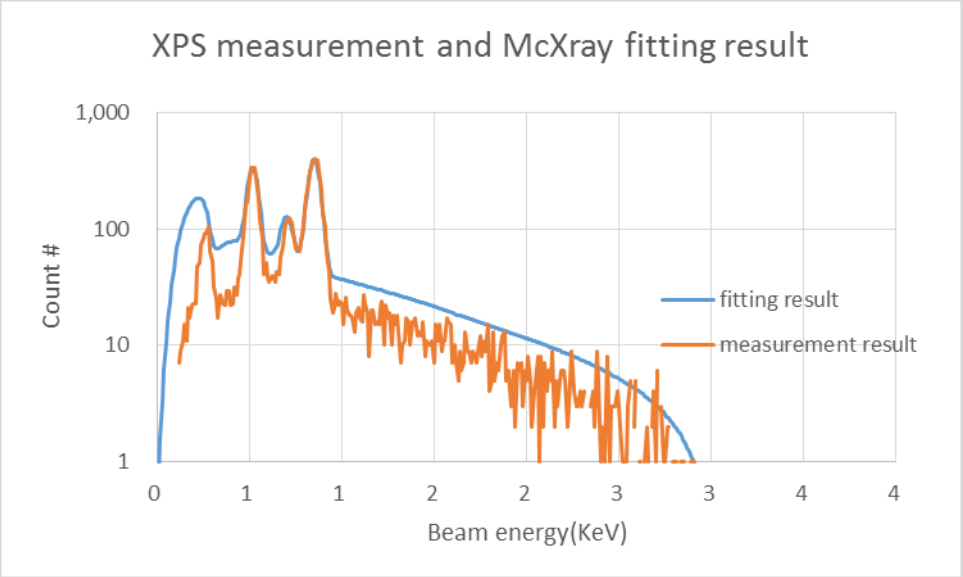

Fig. 59. Real measurement and fitting result compared at 3 keV energy

Table 32. The model detail of PyO on Si/SiO_2/Al substrate simulation at 3 keV energy

First layer: thickness, density	PyO (O/Fe/Ni 0.34/0.11/0.54)	973 Å, NA
Second layer	Al_2O_3	40 Å
Third layer	Al	3760 Å
Fourth layer	SiO_2	5700 Å
Acquisition time	29.4 s	
Angle tilt	52 °	
current	1.08E-10 Amp	

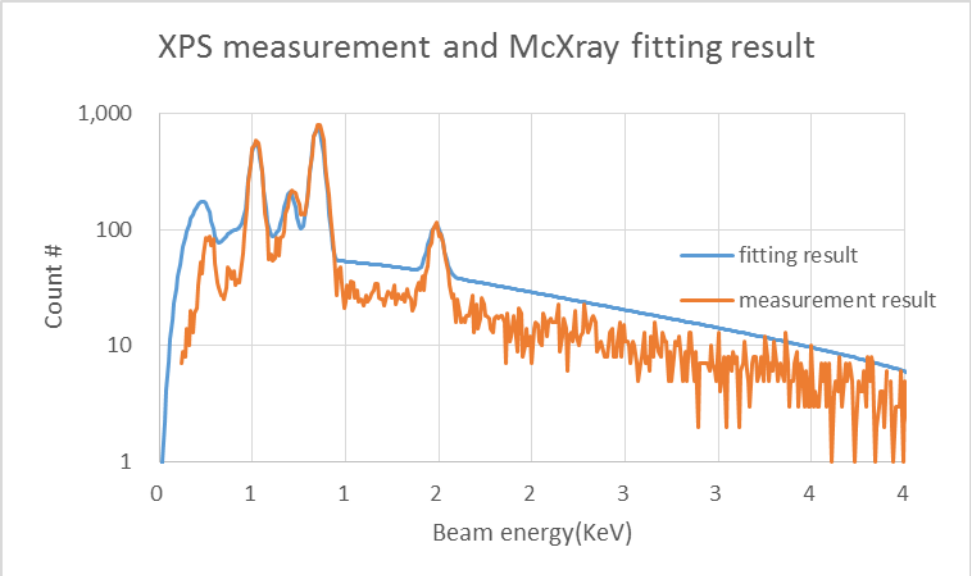

Fig. 60. Real measurement and fitting result compared at 5 keV energy

Table 33. The model detail of PyO on Si/SiO_2/Al substrate simulation at 5 keV energy

First layer: thickness, density	PyO (O/Fe/Ni 0.34/0.11/0.54)	973 Å, 4.5 g/cm^3
Second layer	Al_2O_3	40 Å
Third layer	Al	3760 Å
Fourth layer	SiO_2	5700 Å
Acquisition time	29.4 s	
Angle tilt	52 °	
current	1.1E-10 Amp	

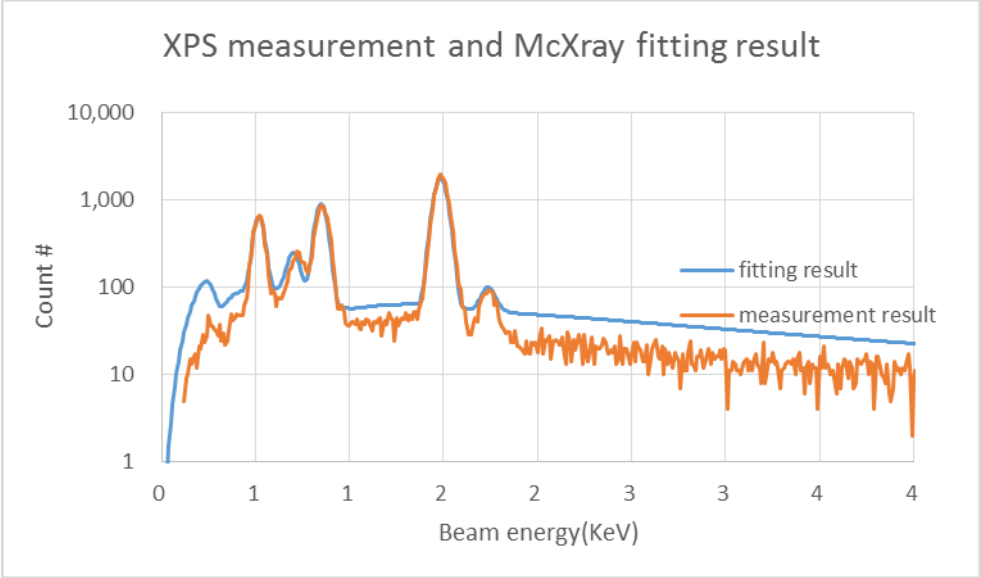

Fig. 61. Real measurement and fitting result compared at 10 keV energy

Table 34. The model detail of PyO on Si/SiO_2/Al substrate simulation at 10 keV energy

First layer: thickness, density	PyO (O/Fe/Ni 0.34/0.11/0.54)	973 Å, 5.7 g/cm^3
Second layer	Al_2O_3	40 Å
Third layer	Al	3760 Å
Fourth layer	SiO_2	5700 Å
Acquisition time	29.4 s	
Angle tilt	52 °	
current	1.05E-10 Amp	

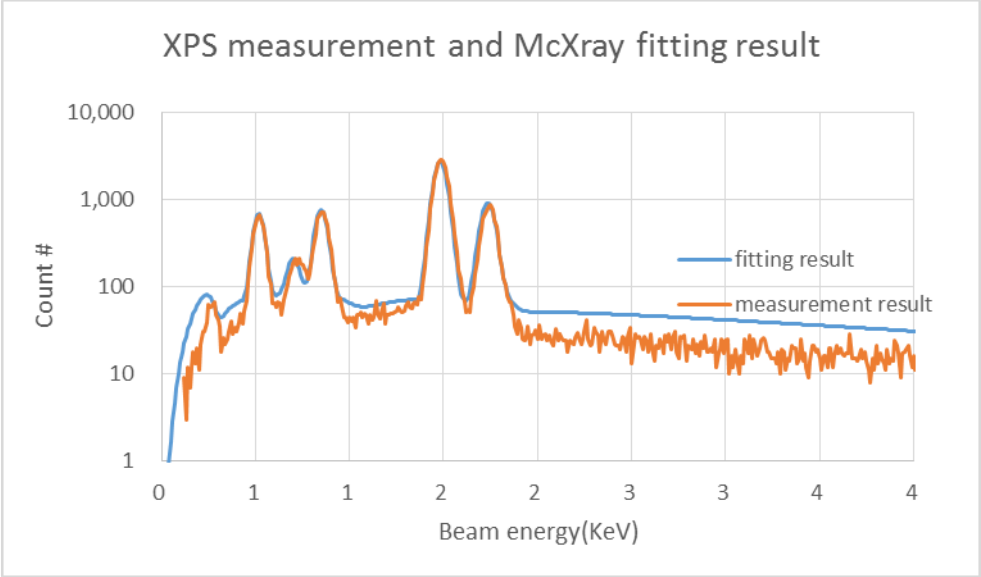

Fig. 62. Real measurement and fitting result compared at 15 keV energy

Table 35. The model detail of PyO on Si/SiO_2/Al substrate simulation at 15 keV energy

First layer: thickness, density	PyO (O/Fe/Ni 0.373/0.114/0.513)	973 Å, 5.9 g/cm^3
Second layer	Al_2O_3	40 Å
Third layer	Al	3760 Å
Fourth layer	SiO_2	5700 Å
Acquisition time	29.4 s	
Angle tilt	52 °	
current	1.05E-10 Amp	

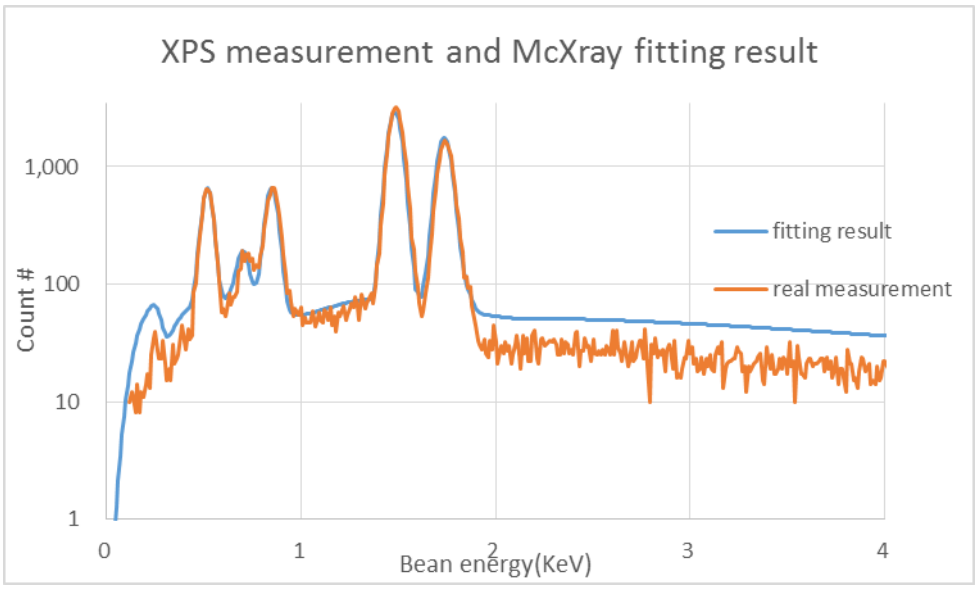

Fig. 63. Real measurement and fitting result compared at 18 keV energy

Table 36. The model detail of PyO on $Si/SiO_2/Al$ substrate simulation at 18 keV energy

First layer: thickness, density	PyO (O/Fe/Ni 0.373/0.114/0.513)	973 Å, 5.9 g/cm^3
Second layer	Al_2O_3	40 Å
Third layer	Al	3760 Å
Fourth layer	SiO_2	5700 Å
Acquisition time	29.4 s	
Angle tilt	52 ^{o}	
current	1E-10 Amp	

V.The simulation of 20% O_2 samples of 10% Fe

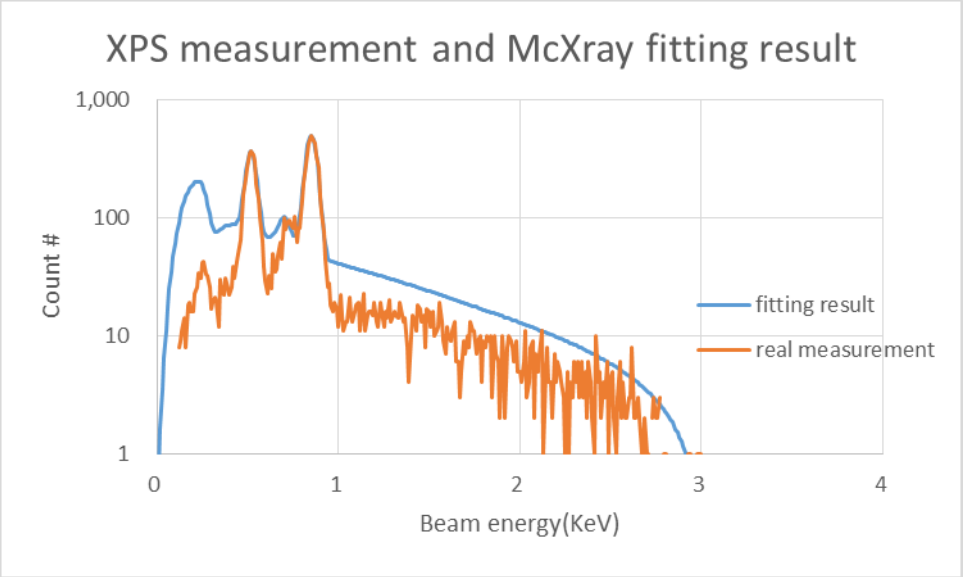

Fig. 64. Real measurement and fitting result compared at 3 keV energy

Table 37. The model detail of PyO on Al substrate simulation at 3 keV energy

First layer: thickness, density	PyO (O/Fe/Ni 0.33/0.06/0.61)	1122 Å, NA
Second layer	Al_2O_3	40 Å
Third layer	Al	1360 Å
Fourth layer	SiN	2500 Å
Fifth layer	SiO_2	900 Å
Acquisition time	29.4 s	
Angle tilt	52 °	
current	1.2E-10 Amp	

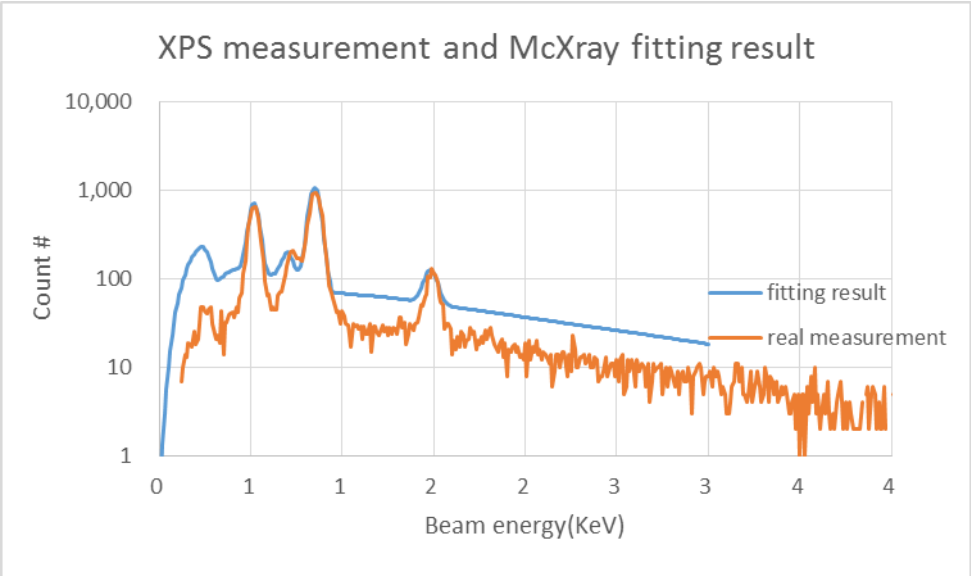

Fig. 65. Real measurement and fitting result compared at 5 keV energy

Table 38. The model detail of PyO on Al substrate simulation at 5 keV energy

First layer: thickness, density	PyO (O/Fe/Ni 0.344/0.063/0.593)	1122 Å, 4.7 g/cm^3
Second layer	Al_2O_3	40 Å
Third layer	Al	1360 Å
Fourth layer	SiN	2500 Å
Fifth layer	SiO_2	900 Å
Acquisition time	29.4 s	
Angle tilt	52 °	
current	1.2E-10 Amp	

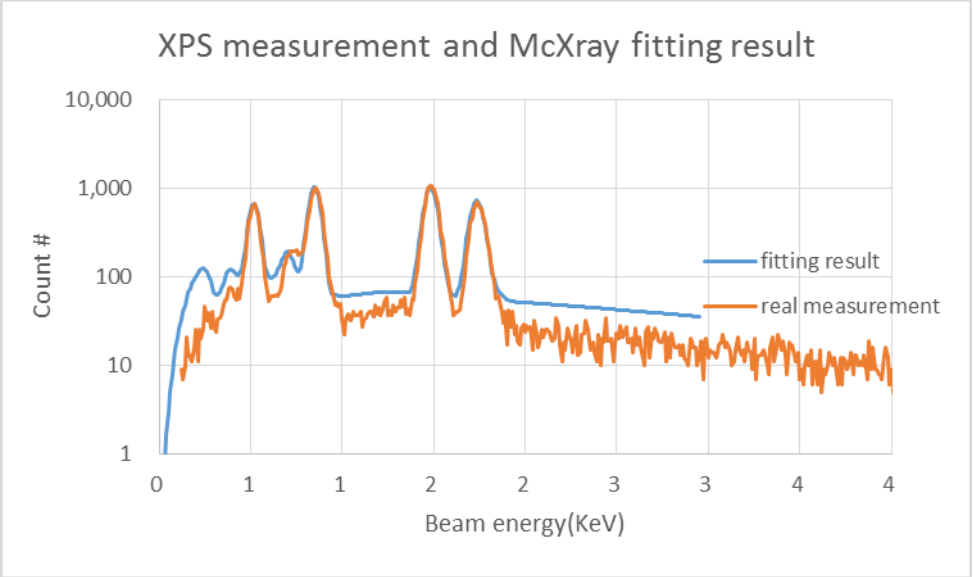

Fig. 66. Real measurement and fitting result compared at 10 keV energy

Table 39. The model detail of PyO on Al substrate simulation at 10 keV energy

First layer: thickness, density	PyO (O/Fe/Ni 0.354/0.062/0.584)	1122 Å, 5.9 g/cm^3
Second layer	Al_2O_3	40 Å
Third layer	Al	1360 Å
Fourth layer	SiN	2500 Å
Fifth layer	SiO_2	900 Å
Acquisition time	29.4 s	
Angle tilt	52 °	
current	1E-10 Amp	

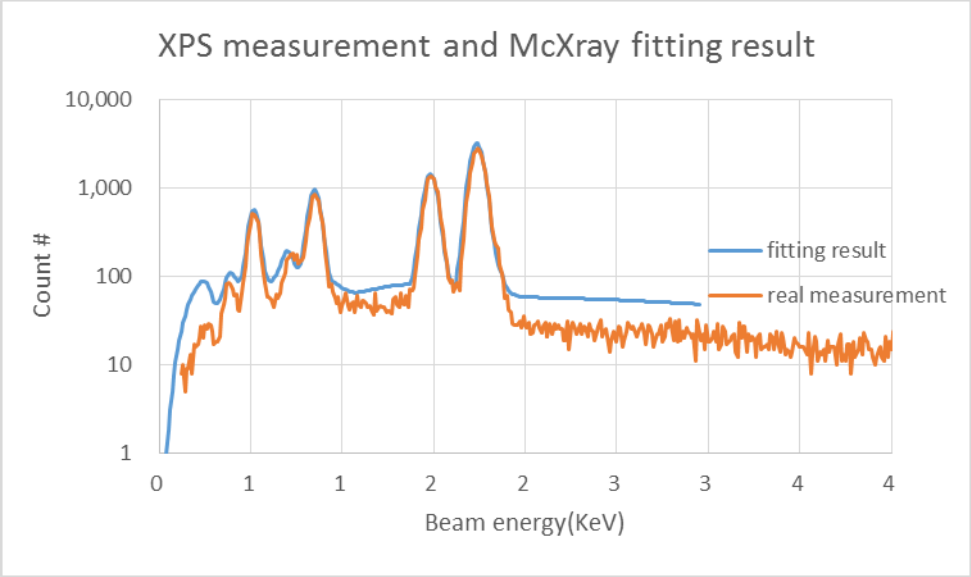

Fig. 67. Real measurement and fitting result compared at 15 keV energy

Table 40. The model detail of PyO on Al substrate simulation at 15 keV energy

First layer: thickness, density	PyO (O/Fe/Ni 0.33/0.08/0.59)	1122 Å, 6.3 g/cm^3
Second layer	Al2O3	40 Å
Third layer	Al	1360 Å
Fourth layer	SiN	2500 Å
Fifth layer	SiO_2	900 Å
Acquisition time	29.4 s	
Angle tilt	52 °	
current	1.2E-10 Amp	

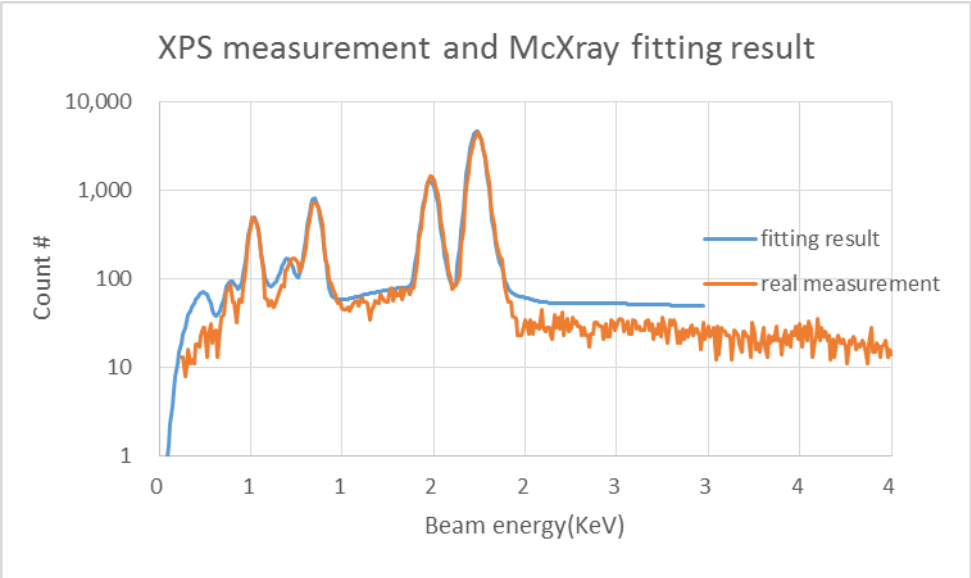

Fig. 68. Real measurement and fitting result compared at 18 keV energy

Table 41. The model detail of PyO on Al substrate simulation at 18 meV energy

First layer: thickness, density	PyO (O/Fe/Ni 0.33/0.07/0.6)	1122 Å, 6.3 g/cm^3
Second layer	Al_2O_3	40 Å
Third layer	Al	1360 Å
Fourth layer	SiN	2500 Å
Fifth layer	SiO_2	900 Å
Acquisition time	29.4 s	
Angle tilt	52 ^{o}	
current	1E-10 Amp	

VI. RRAM DEVICE TEST WAFERS

6.1 Real device of RRAM

To confirm that PyO can work the same way as NiO in an RRAM memory cell, a real device is required. In this study, three device wafers were made in the Tx state cleanroom, including two wafers using NiFe-oxide with 10% and 19% Fe concentration and one wafer using pure NiO. The device wafers contain several test structures including memory cells. The memory cell is made of three different layers, the memory layer made of the transition metal oxide, and two electrodes, one on the top and one under the transition metal oxide. The shape of the structure is shown in Fig. 69. The bottom electrode consists of a 150 nm Co layer on top of a 2 nm Ti layer. The square identified as isolation is the NiFe-oxide or NiO. The top layer is made of 75 nm of Co deposited on top of 20 nm of TiN. TiN acts as a diffusion barrier and prevents the oxygen from diffusing into the top electrode keeping the RRAM memory cell stable and the switching repeatable. In addition, an electrode configuration was chosen that had not been reported on in literature. The bottom electrode was intended to be the positive electrode during the forming soft breakdown step where oxygen is removed from the transition metal oxide layer.

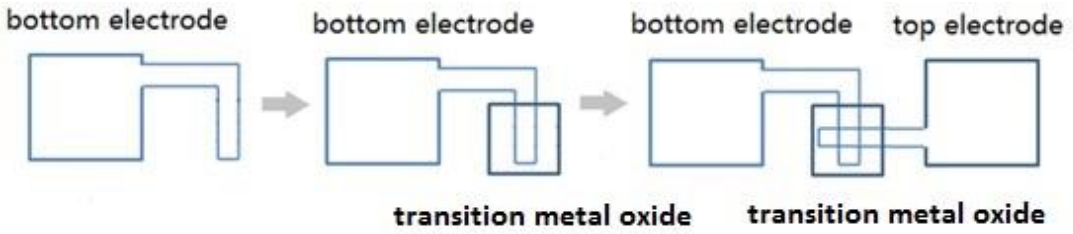

Fig. 69. The three different layer of the real RRAM memory cell

All the electric measurement reported on in this chapter including the characterization of the electrode material and the measurements were on the Van der Pauw structures refer to the $Ni_{0.9}Fe_{0.1}$-oxide wafer. No electrical measurements were done on the other two wafers.

6.2 Fabrication Process of the device wafers

6.2.1 Substrates

Three full 4" Silicon Wafers were used for the device test wafers. The details of the three wafers are provided in Table 42. A SiO_2 isolation layer was grown on the silicon wafers by wet oxidation. First, the native oxide on the wafers was removed by a hydrofluoric acid 49% dip. Immediately after this step, a wet oxide was grown on the wafers. The wet oxidation furnace in the cleanroom was used for this purpose. The process parameters for the oxidation process are shown in Table 42 below. The thickness of the oxide layer was determined from the ellipsometric spectra measured on the completed wafers using the Horiba ellipsometer. The following model was used: the model with 2 layers that were Si/SiO_2. The optical properties were measured from 1.5eV to 5eV with a fixed angle of incidence of 65^o. The

measurement data was used to determine the thickness. An oxide thickness of about 2300 Å thickness was found on each wafer.

Table 42. Information on the substrate used for devices

Diameter (mm)	Orientation	dopant	Thickness (μm)	Resistivity (ohm cm)
100	1-0-0	p-type	525 +/-20	10-15

6.2.2 Thin Film Deposition Process

The AJA sputtering system was used to make all the thin films of the wafers. As the transition metal oxide is transparent, the Horiba ellipsometer was used to determine the thickness of it. A stylus profilometer was used to measure the thickness of the electrodes. Measurements were not performed on the completed wafer but on thin films made under similar conditions.

6.2.3 Processing of a real device

As shown in Fig. 69, the top and bottom electrodes each consisted of two layers. The bottom electrode consisted of a 150 nm Co layer on top of a 2 nm Ti seed layer. The purpose of the Ti seedlayer is to improve the adhesion of the electrode to the substrate and to make it more stable during the microstructure process following its deposition. Before applying the photoresist, the substrates were cleaned with an O_2 plasma etch step (30 Watt power for I min 30 sec) to get a clean surface. More details on the lift-off lithography process are provided below. The first mask was used to pattern the bottom electrode. There was no extra cleaning before the metals were deposited on top of the patterned photoresist. Ti and Co were deposited using the

AJA deposition system with 350 Watt power from the DC gun. The deposition time was decided by the deposition rate monitor inside the chamber and a test run on a substrate wafer. Before the test wafer was loaded into the system the crystal monitor was moved just under the sample holder position and the deposition rate was measured. Then a deposition was performed on the test layer, and its film thickness was measured by the stylus profilometer, to confirm the deposition rate measured by the deposition monitor. All of the deposition condition's details can be found in Table 43 below. For the electrode a large Ar flow rate was used, 50 SCCM, to get a higher deposition rate. But 20mins deposition time was still needed to deposit a 150 nm thick electrode layer. As the equipment requires a cooling down period for the sputter gun for every 10mins of deposition time, the total time to deposit the bottom electrode was approximately 1 hour. The thickness of the different layers is summarized in Table 43.

Table 43. Summary of deposition parameters of oxide and electrode layers and the process parameters for the isolation oxidization layer

layer	target	Power type	Power (Watt)	Ar flow rate (SCCM)	O flow rate (SCCM)	Pressure (Torr)	Deposition time (s)
Ti/Co	Ti	DC	250	50		1.3E-3	10
	Co	DC	250	50		1.3E-3	1200
NiO	Ni	RF	240	8	2	NA	381
PyO(10%Fe)	Py(10%Fe)	RF	240	8	2	1.3E-3	353
PyO(19%Fe)	Py(19%Fe)	RF	240	8	2	1.3E-3	500
TiN/Co	TiN	RF	150	70		1.0E-3	1200
	Co	DC	360	70		1.0E-3	600
layer	Temperature (^oC)		N_2 flow rate (liter/min)		O_2 flow rate (liter/min)		time
Oxidization	1000		2		2		2h 30min

The transition metal oxide layer is made by reactive RF magnetron sputtering. The deposition rate was also determined by the deposition rate monitor and a test sample similar as for the bottom electrode. The test sample, a small square sample, was loaded with the whole 4” wafer, though. So test sample and wafer were deposited at the same time. A lower Ar flow rate was used similarly to the flow rate of the study in previous chapters. The thickness of oxide was determined by the Horiba ellipsometer as it is a transparent layer. Also, these deposition parameters are summarized in Table 43. The planned oxide thickness was 50 nm. But for the 19% Fe concentration wafer the oxide was i.e. 78 nm. The top electrode was made by RF magnetron sputtering. The deposition rate of TiN was very low. It would take hours until a 100 nm layer is made. To increase the conductivity of the top electrode, a Co layer was deposited on the top of the 20 nm thick TiN by using DC magnetron sputtering. The thickness of the top electrode was also measured by the profilometer.

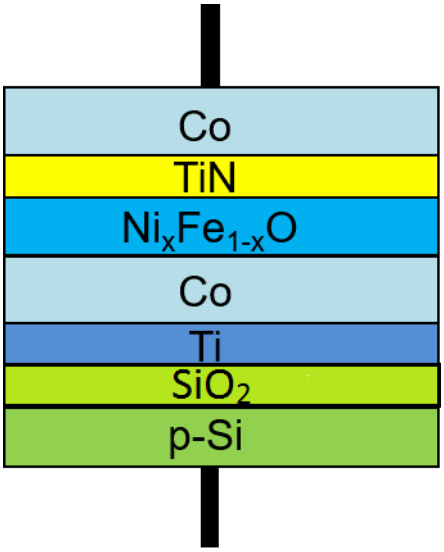

Fig. 70. The memory cell structure

Table 44. Film thickness data for device wafers

layer	material	NiO (nm)	$Fe_{0.1}Ni_{0.9}O_{1-\delta}$ (nm)	$Fe_{0.19}Ni_{0.81}O_{1-\delta}$ (nm)
Ti/Co	Ti	2	2	2
	Co	150	150	150
NiO	Ni	50		
PyO (10%Fe)	Py (10%Fe)		50	
PyO (19%Fe)	Py (19%Fe)			87
TiN/Co	TiN	20	20	20
	Co	78	78	78
SiO_2 isolation layer	Si	2391		2307

6.2.3 Lithography process

The various layers of the wafers were patterned using a lift-off process. A SuSS MJB4 mask aligner was used to expose the photoresist. As shown in Fig. 69 the system is also in the cleanroom. Additional equipment that was used for the patterning were a spinner, a sonicator and also an O_2 plasma cleaner. The spinner in this study was WS-650MZ-23NPP/LITE model from Laurell, and the sonicator was a Branson 2800. The

cleaner was the plasma etch equipment of Unitronics

Fig. 71. Equipment used in cleanroom

AZ 5214E photoresist was used to make the pattern in the different layers of the memory cell. Before the photoresist was applied to the sample was cleaned in an O_2 plasma. The equipment of the plasma cleaner is also in the cleanroom and with 30w power and 1 min 30 seconds cleaning time the surface of the samples is good to be covered by the photoresist. The AZ 5214E photoresist was applied on the wafer using

a spinner. With a three step-spin process, the photoresist will cover the sample evenly across its surface. The spin parameter is summarized in Table 45. The soft bake as the next step was needed to remove the solvent. The sample was baked for 1min at 100^{o}C on a hot plate in the cleanroom. The thickness was measured after the soft bake. A 1.64 μm thickness was found using the Horiba ellipsometer. The materials file used to calculate the thickness of the photoresist from the ellipsometric spectra was the original photoresist layer data file from the Horiba ellipsometer database library. The expected thickness of the photoresist estimated from the spin speed and the photoresist datasheet is 1.14 μm. The difference might originate from a change of the viscosity of the photoresist after the bottle was opened. A SuSS MJB4 mask aligner was used for the exposure. The exposure time was 1.6s, and the power used in this study was 30w. After the exposure process, the development step was needed to form the pattern on the sample. The AZ 300 MIF developer was used in this process. The areas that were not exposed to light were removed by the developer. The result after development using this condition looks good under an optical microscope. After development, the wafers were loaded into the sputtering system for deposition of the specific layer. Details on the lithographic process parameters are summarized in Table 45

After deposition, an additional liftoff step was required to remove the photoresist and film in the areas that were exposed to light. Acetone was used to remove them. After 5 minutes in the sonicator, the sample was also cleaned in the spinner with an acetone drop. The lithography process was the same for all three wafers and for each

layer. After liftoff, the sample was cleaned in the plasma cleaner before new photoresist was applied for the next microstructuring step. Three different masks were used to make the test wafers.

Table 45. The spin-parameters for the photoresist and liftoff processes

photoresist			
step	Duration (s)	RPM	Accel (RPM/s)
1	10	1000	500
2	10	2000	1000
3	30	6000	3000
liftoff			
step	Duration (s)	RPM	Accel
1	10	100	100
2	40	0	100
3	30	4000	4000

6. 3. Characterization of the Device Wafers

6.3.1 Device Wafer

The device wafers were made using a mask set for 4'' wafers developed by Casey Smith. Each wafer contained 36 dies each 155x120 mm^2. In order to be able to identify each device unambiguously, the following syntax was used: (a,b)Qc,d,e. The number between the brackets is the id number of the die and gives the position of the die with respect to the center of the wafer. The c defines the quadrant of the die. Each die contains four quadrants that is labeled on the wafer. The last two numbers identify the row and the column of the specific test structure in the device group under study counted from the bottom left of the block of test structures. Fig. 70 below explains the meaning of (a,b) and d,e in more detail.

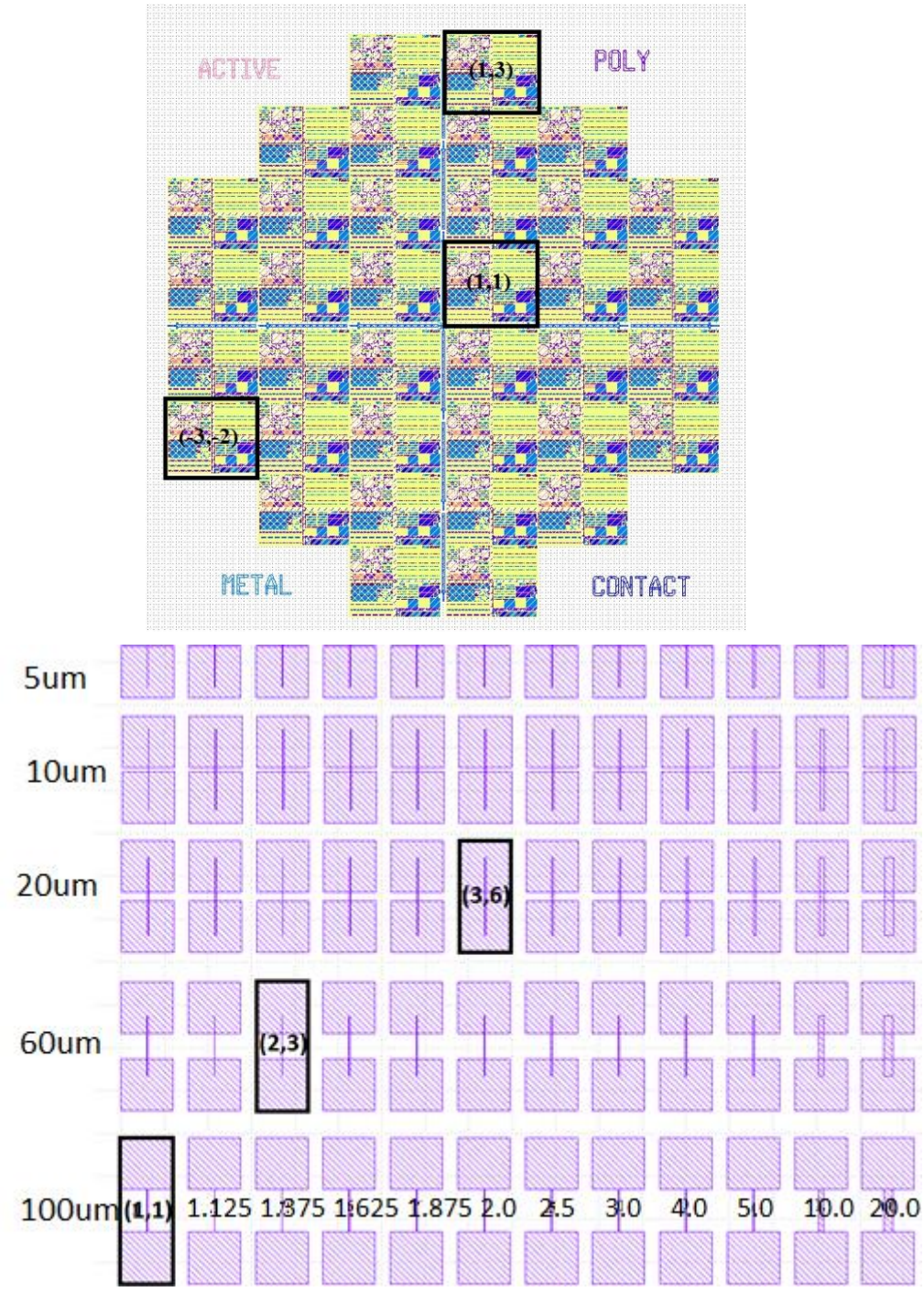

Fig. 72. Id number of the die on the wafer (top) and id number of the device in the device group (bottom)

In addition to the RRAM devices of Fig. 67 other test structures are present on the device wafers that were formed by the three masks. Although some of them do not work as more mask steps are needed, others are functional and can be used to

determine the electrical properties of the electrodes and oxide layers. Measurements on those test structures can provide information on the process and identify defects. Fig. 71 shows the four different test structures that were used for electrical characterization of the patterned layers.

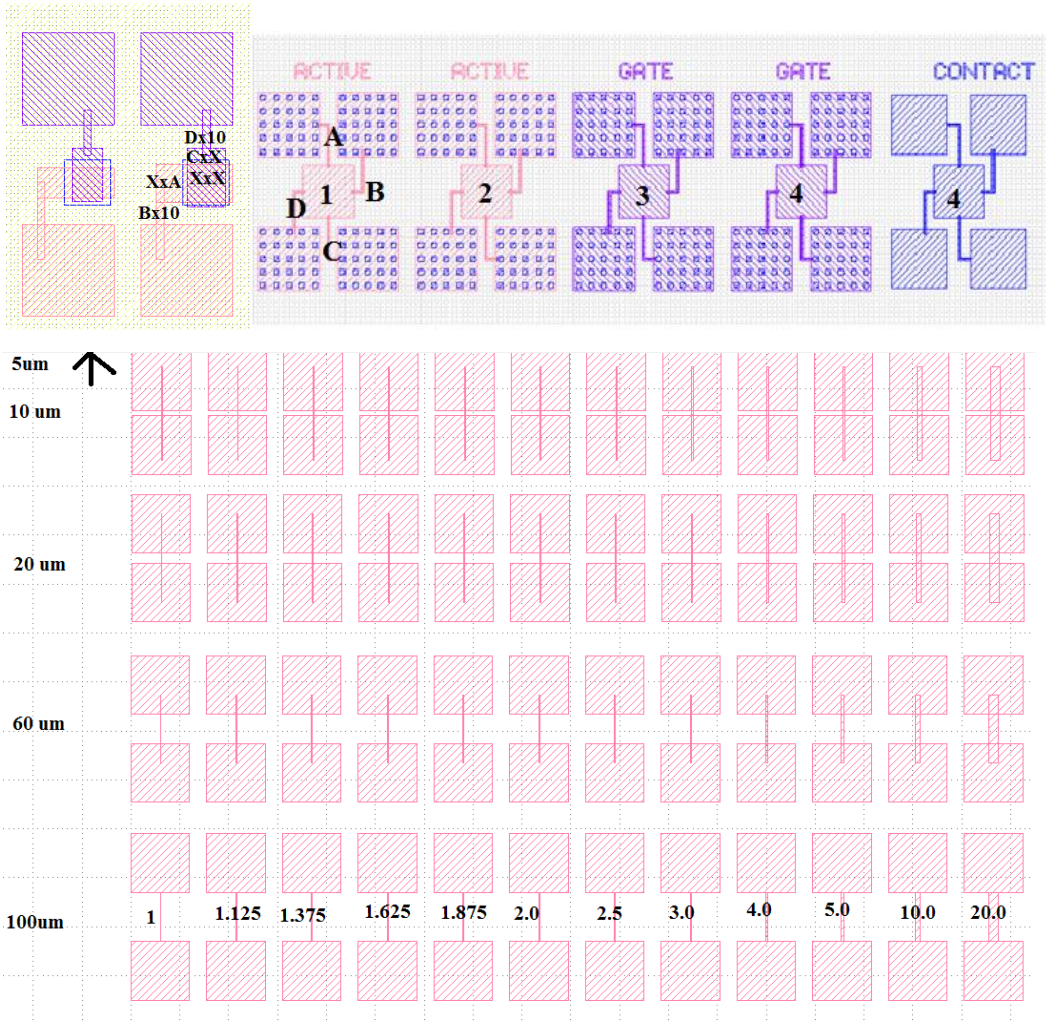

Fig. 73. Characterized test structures on device wafers (pink=bottom electrode, purple is top electrode, and blue is oxide layer): (a) Capacitance devices (top left); (b) Van der Pauw structures (top right); (c) 2pp resistance structures with different line width and length for bottom electrode (middle) and (d) top electrode (bottom)

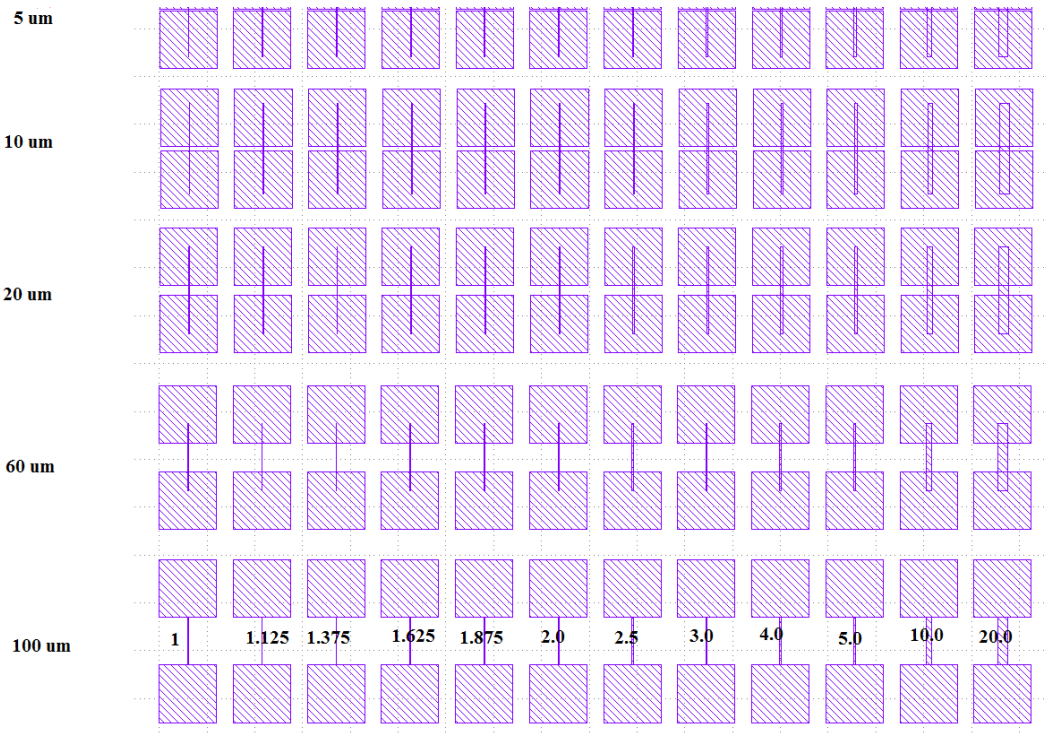

Fig. 71. Continued

6.3.2 Electric characterization of the bottom electrode from 2pp device block

The Semiconductor Parameter Analyzer (SPA) was used in a two point probe (2pp) configuration to determine the I-V relation of the bottom electrode from the 2pp device block (Fig. 71c). The IV-relation was linear over the measured range.

The resistance vs line width curve was measured on all 60 μm pad spaced devices and the resistance vs pad separation curve was on 20 μm line width devices. The results are summarized in Table 49 in Appendix VII.

The sheet resistance was calculated to find out whether or not the resistivity was changing with different test structures. The sheet resistance is the resistance per unit square area. As shown by Schroeder, the resistance of a square thin film that has

electrodes lined up along two opposite sides is independent of the size of the square and equal to:

$$R_{sheet} = \frac{\rho W}{Wd} = \frac{\rho}{d} \qquad \text{[Equation 6.1]}$$

Where ρ is the resistivity, d is the film thickness, and W is the width of the square. This resistance is called the sheet resistance and is proportional to the resistivity of a certain film thickness. The sheet resistance was calculated from the measured resistance using the following relation:

$$R_{sheet} = \frac{R}{L} W^2 \qquad \text{[Equation 6.2]}$$

Where L is the length of the 2pp device, R is the measured resistance, and the other parameters are the same as above.

The sheet resistance curve for the bottom electrode is shown in Fig. 72 below.

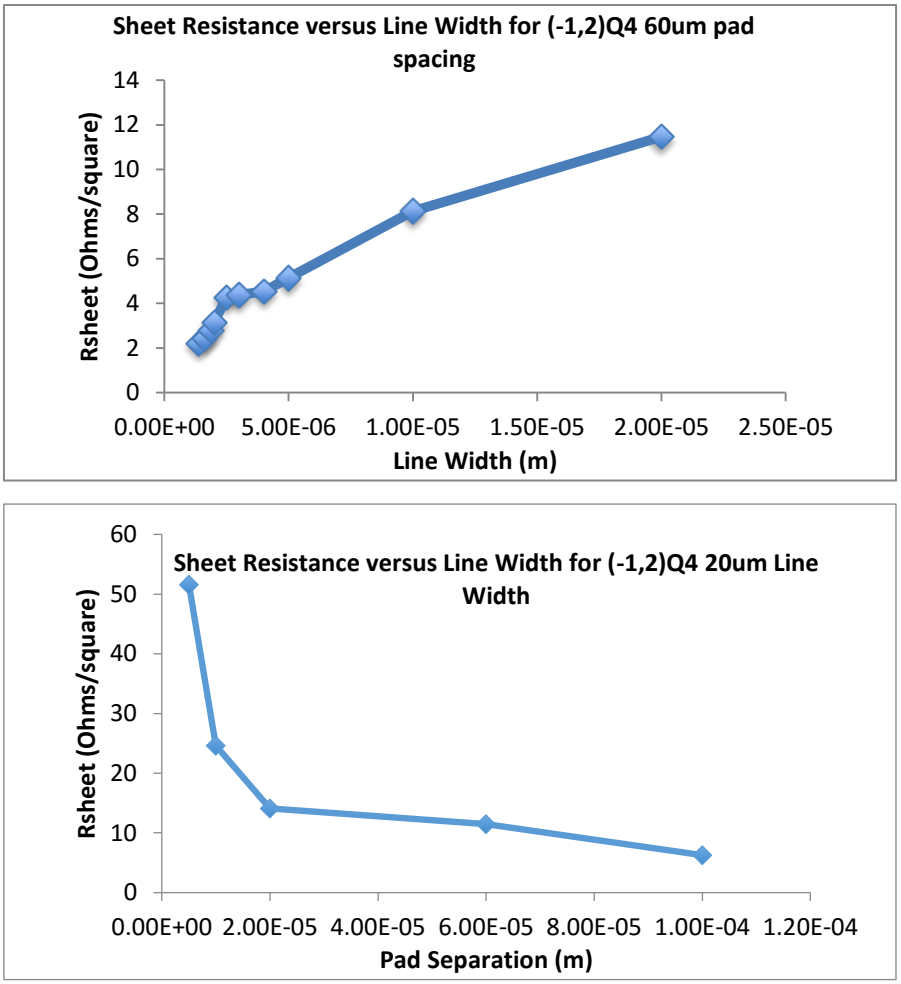

Fig. 74. Sheet resistance versus line width for 60 μm pad spaced resistance devices at (-1,2) Q4 (top) Resistance versus pad separation for 20 μm line width resistance devices at (-1,2) Q4 (bottom)

The sheet resistance is not constant with the length of the wires but increases for shorter wires. The device with the shortest length, i.e. 5 μm still had a resistance of 12 Ω while one would expect a much lower value for a device with a width of 20 μm and a length of 5 μm. After 10 Ω was subtracted from all measured resistances, the measured sheet resistance varies much less as a function of the device length (see Fig. 73 blow). That 10 Ω can come from the spreading resistance in the bonding pads, or from the contacts resistance between the electrodes and the bonding pads.

The sheet resistance (R_s) as a function of the line width is also not constant but

increases with the line width. This could indicate that the edges of the lines/wires have a lower resistivity than the center of the wires. So the test structure can be thought of as being shunned by a smaller resistance. If a constant offset (6 μm) is added to the mask line width, the sheet resistance versus line width graph is flattened (see Fig. 73 on the left).

With both series resistance and parallel resistance correction, the line length and line width series got a similar resistance range. The sheet resistance is about 10 Ω/□. The longer test structures are expected to provide more accurate sheet resistance information than the shorter test structures. For test structures with a small line width there will be a large error in the line width and for test structures with a large line width, there will be a large error in the measured resistance.

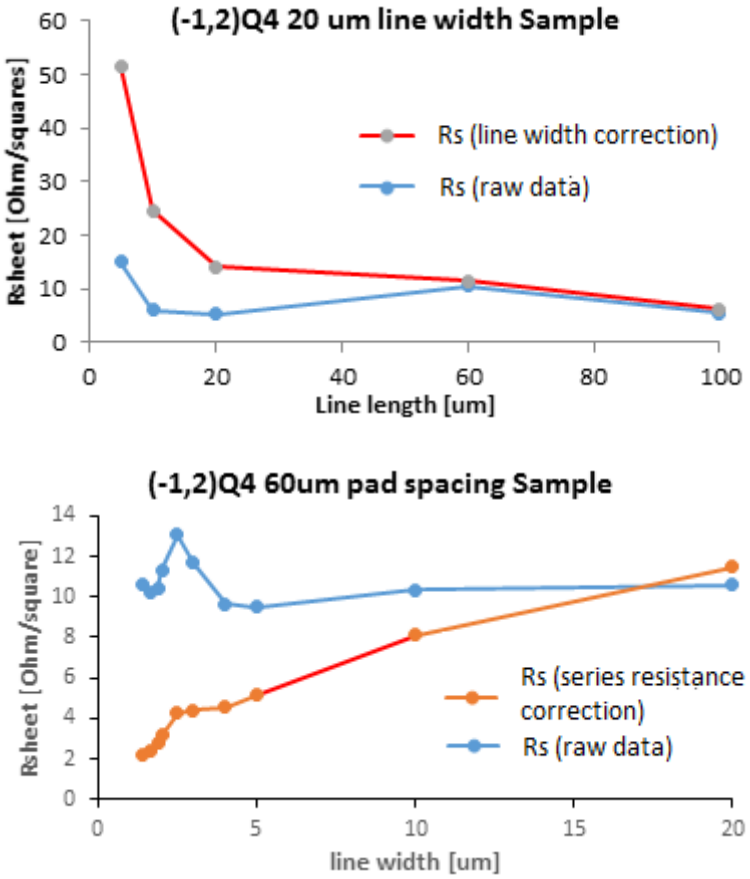

Fig. 75. Calculated sheet resistance as a function of device length (left) and line width (right). Each graph shows the Rsheet calculated from the measured 2pp resistance and the mask data (raw) and the Rsheet calculated from the corrected measured 2pp resistance (10 ohms subtracted) and the corrected mask line width (6 μm added to line width)

6.3.3 Electric Characterization of top electrode from 2pp device block

A similar measurement and analysis as for the bottom electrode were also done for the top electrode. The IV relation of the 2pp test structures of the top electrode was also linear. The measured resistances were larger than for the bottom electrode, as the thickness of the top electrode was significantly less compared to the bottom electrode. The work is only done on the 20 μm Line width series, and data is in Table 50 of appendix VII.

The sheet resistance was calculated from the measured resistance and the mask line

width and similar as for the bottom electrode the sheet resistance was not constant. As the resistance of the shortest (6 μm) device was 52 Ω, 45 Ω was subtracted from all measured resistances. Also, this graph flattened. The curve is shown in Fig. 74 below. The average sheet resistance is 25 Ω/□ a little more than twice the sheet resistance of the bottom electrode. This is consistent with the thickness difference between the top and the bottom electrode.

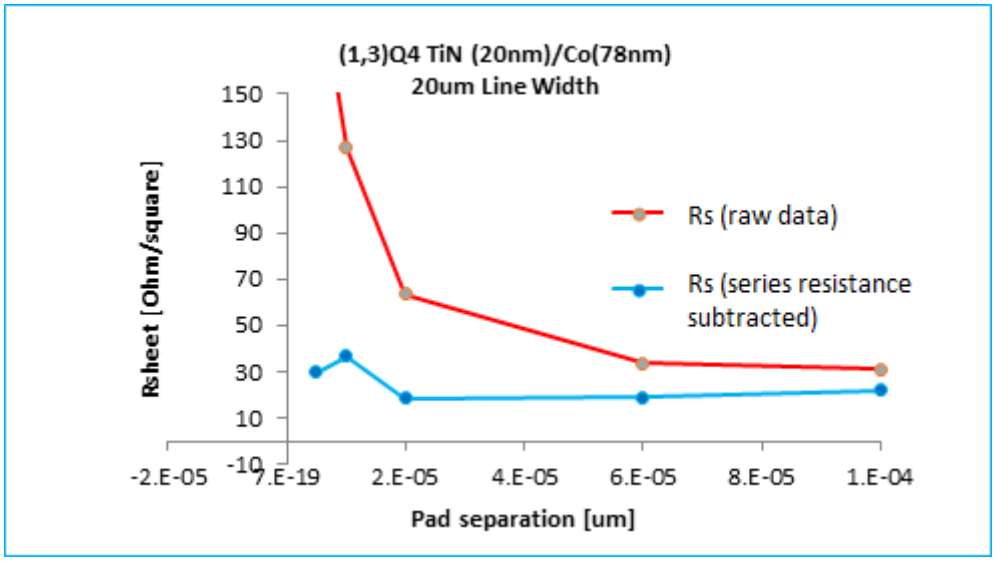

Fig. 76. Sheet resistance as a function of the line width for the raw data (blue curve) and the data corrected for the series resistance (red)

The measured sheet resistances are also consistent with resistivity values found in the literature. $\rho_{\text{Cobalt sputtered}}$ is 4.5E-6ohm meter, and TiN is 1E-5 ohm meter [55] [56]. In addition, the subtracted resistance that flattened the sheet resistance versus pad separation graph for the bottom electrode is smaller than that for the top electrode. They are approximately a factor 4 apart. So the additional resistance can be originating from the spreading resistance in the bonding pad or from the contact resistance between the electrode and the bonding pad.

6.3.4 Electric characterization of the oxide layer from measurements on the van der Pauw structure device group

To determine the resistivity of the microstructured oxide, measurements were done on the van der Pauw structures. The PyO with 10% concentration of Fe sample was measured on Van der Pauw structures. The structure is shown in the top right of Fig. 73. The dimensions of the leads between the bonding pads and the actual test structures are listed in Table 46((-1,2) Q1.Contact (PyO)). The corner squares were counted half. Both four-point probe (4pp) and two-point probe (2pp) measurements were performed.

Table 46. Dimensions of the leads between bonding pads and test structure for the van der Pauw test device. For the definition of A, B, C, and D see Fig. 73.

	size	Number of squares
A	72.5x5; 5x20 μm	18.5 squares
B	67.5x5; 5x16.5 μm	16.5 squares
C	72.5x5; 5x20 μm	18.5 squares
D	67.5x5; 5x16.5 μm	16.5 squares

Every possible 2pp configuration was measured by 2pp measurement with a voltage source and a current monitor. The conditions and result of both 4pp and 2pp measurement are in the Table 51 of appendix VII.

To do the calculation of 4pp result, for the square structure the sheet resistance is proportional to the ratio of the measured voltage and the measured current. The Equation 2.10 was used to get the sheet resistance from measured voltage and current

A 1E9+/-0.2E9 Ω/□ sheet resistance of PyO was found from the 4pp measurement, and the large error is caused by the digital resolution of the voltage meter of the SMUs. The 2pp measurements resulted in a sheet resistance of 1.2E9 Ω/□. A linear IV curve was also found on the 2pp configuration. The slightly higher value found for 2pp can be due to the high contact resistance between the electrode and the oxide observed in continuous films that were deposited under similar conditions. The sheet resistance was also measured on the quartz sample on chapter 3 with a sheet resistance map on the surface. The 4pp result shows the resistance about 1.42E9 average. The quartz sample was made under the same conditions as the oxidization layer measured in this chapter and the deposition time was 600s other than 353s here. A 41% different deposition time made a resistance of sheet different about 30%. The different of deposition time and the sheet resistance can be from the different crystal size of the deposition time. The conclusion from the previous chapter shows that the crystal cell size can be different from different deposition time with same parameters deposition. The linear IV relation and the absence of hysteresis in the IV graph suggest that there is no soft breakdown when the current is applied parallel to the substrate. We expected soft breakdown only to occur for IV measurements perpendicular to the thin film.

6.3.5 Electrical Characterization of RRAM devices

The capacitance devices shown in Fig. 71a were characterized with the Semiconductor Parameter Analyzer. A voltage ramp of -4 to 4 volt was applied to

determine the switching behavior. The bottom electrode was connected to SMU1, and the top electrode was kept at 0 volt. The measurement started by applying -4 volt to the Co bottom electrode followed by a voltage ramp from -4 to 4 volt and then ramped back to -4 volt. For NiO, the scanning speed was 1 second per point. Other two were 0.1 seconds per point. The voltage difference between two points was 0.1V. The ramps were repeated several times until the IV curves are no longer changed. Then the ascending and descending IV curves were recorded. The ascending (blue) and the descending (orange) curves in the IV graph were different, so the graph shows hysteresis. Also, notice that the IV curves are non-linear. The measurements were done on a device with a size of 40*40 μm^2 on both the NiO and the $Ni_{0.9}Fe_{0.1}O_{1-\delta}$ device wafers. The alignment of 19% Fe PyO samples was not good, and there was a short between the top and bottom electrodes on the large RRAM memory cells. So for the $Ni_{0.81}Fe_{0.19}O_{1-\delta}$ device wafer the measurement were done on a capacitance device with a size of 6*6 μm^2. The VI curves are shown in the Fig. 77.

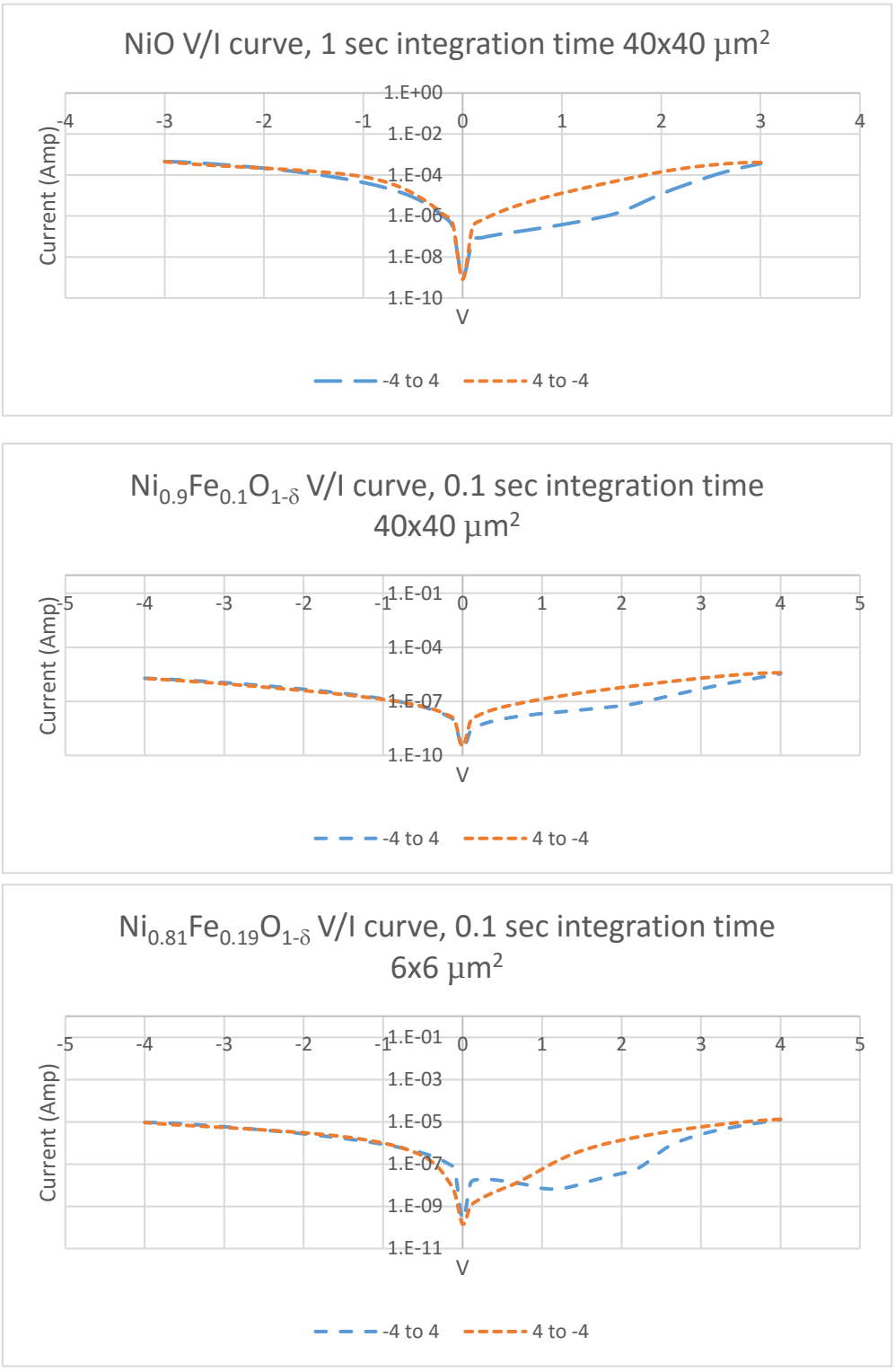

Fig. 77. VI curve of the real devices measured between -4 and 4 volts

For all three devices, a similar IV characteristic was observed. The IV curve is nonlinear, asymmetric and shows hysteresis, i.e., different behavior for ascending

and descending voltages. The maximum current was the largest for the NiO capacitance device, i.e. almost a factor 100 larger than for the other iron doped NiO devices. With the significant smaller area size of the 19% Fe device the maximum current density of the $Ni_{0.81}Fe0._{19}O_{1-\delta}$ and the NiO devices is of the same order of magnitude. The slope of the IV curve at zero volt is not the same for the ascending and descending voltage ramps. The IV curve around zero volt is shown in the 6E of the appendix.The measured values are listed in columns 8 and 9 below. Using the measured in-plane resistivities on continuous films and the dimensions of the test structures, the resistance perpendicular to the film substrate was calculated (see column 6 in Table 47).

Table 47. Resistance determined from IV curve at V=0

	ρ (Ω cm)	ρ_{meas} (Ω cm)	t [m]	A [m^2]	R_{calc} (Ω)
NiO			5.00E-08	1.60E-09	
$Ni_{0.9}Fe_{0.1}O_{1-\delta}$	5.00E+02	6.00E+01	5.00E-08	1.60E-09	1.56E+04
$Ni_{0.81}Fe_{0.19}O_{1-\delta}$	5.50E+02		8.70E-08	3.60E-11	1.33E+06
	Rcalc 2	Rmeas(high)	Rmeas(low)	Rhigh/Rlow	Rmeas/Rcalc
NiO		7.25E+05	493306.5	1.47	
$Ni_{0.9}Fe_{0.1}O_{1-\delta}$	1.88E+03	6.25E+05	2.102E+05	2.14	29.33
$Ni_{0.81}Fe_{0.19}O_{1-\delta}$		5.00E+08	3.00E+06	167	189.22

The measured resistance values are considerably larger than the resistance values estimated from resistivity and film thickness. The resistance difference can be caused by the presence of a significant contact resistance between the metal electrodes and the oxide thin film as was also observed in measurements on continuous films by linear 4pp and 2pp probe. The nonlinear IV behavior suggests the presence from at

least one Schottky contact between the electrodes and the oxide. There can be a capacitor formed in this three-layer structure resulting in charging effects that change the zero-voltage resistance value for ascending and descending voltage ramps. So the resistivity difference may not be caused the soft breakdown. The next study need focus on the determination of the cause of the here observed switching behavior.

6.4 AFM measurement of the device wafers

The AFM measurement was made on the RRAM memory cells to determine the condition of the surface and the quality of the microstructuring at different positions within a RRAM device on the PyO wafer. A 512*512 points scan was made with a scan length of 50 μm. The quarter of RRAM memory cell with two perpendicular edges of the transition metal oxide layer and two electrodes was in the scanning area. The parameter of the AFM measurements are summarized in Table 48, and the AFM result is shown in Fig. 76 below.

Table 48. AFM measurement parameters for the scan shown in Fig. 69.

sample	Scan Size(μm)	Sample/line	Scan speed(μm/s)	Integral gain	Prop. gain	Amp setp.(V)	Drive Freq.(kHz)	Drive amp.
PyO (10% Fe concent.)	50	512	10	0.2933	0.3376	1.377	158.869	373.6

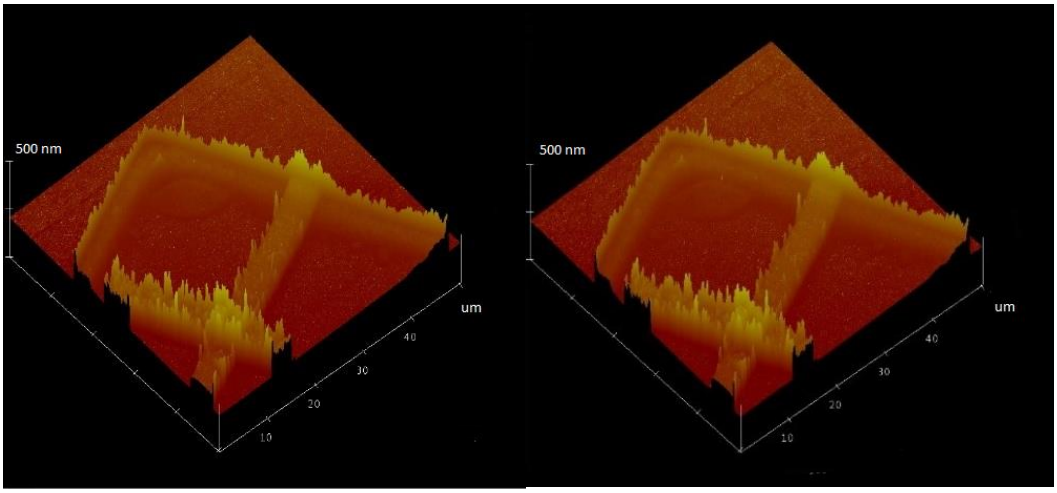

Fig. 78. AFM image of the NiO memory cell for the left to right scan lines (left) and for the right to left scan lines (right)

The AFM picture shows that at the edges of the microstructures a rim exists. The images created from the left to right scans and from the right to left scans have the same features and are similar. The rims observed near the edges of the structures unlikely originate from overshoot of the tip while scanning. Detailed analysis shows that this rim is several μm wide. It is believed that the rim is caused by the lift of photolithography process. The material is deposited on the sidewalls of the windows created in the photoresist. After the lift-off process, the photoresist is removed and the material originally covering the side wall of the windows in the photoresist remain as rims at the edges of the microstructures. The thicker areas close to the rims are currently not understood. The thick area is much higher than the other points on that isolation. Note that the scale in the z direction is 500 nm. The presence of the rim is consistent with the electrical characterization of the line width series. It confirms that actual line width is larger than the mask width which has a similar effect as a low resistivity near the edges of the structures. This effect can be

significant with a very narrow deposition structure. A good way to avoid this it is to use a photoresist with a lower viscosity or use higher spin speeds. Other methods to avoid the rim is use image reversal or use an intermediate layer between the photoresist and the substrate that is not photo sensitive with soluble in the developer.

6.5 The result and conclusion

The measurement results on the real devices show a lot of parts that need to be improved. The photoresist processing need be modified to minimize or avoid the rim at the edge of the microstructures. The thickness of the transition metal oxide needs to be controlled better. The third is the TiN electrode material. Recent maintenance has shown issues with the RF-gun used for the deposition of the TiN. A study needs to be performed to find how to sputter low resistive TiNi films. Some others materials with a low diffusion coefficient for oxygen may need to be looked for as well in the next research. It is recommended to use Platinum for the other electrode as it will allow for a reversible transfer of oxygen in and from the 2^{nd} electrode. As a Pt target is expensive, it was not available for this research study.

VII.electrical measurement result detail on the real RRAM device

Table 49. Pad separation, line width, measured voltage, measured current, calculated resistance, number of squares, and sheet resistance for measured Ti resistance devices at (-1,2)Q4

Electrode Device:	Pad separation (m)	Line width (m)	Meas. Voltage (V)	Meas. Current (Amp)	Calc. Resistance (Ω)	No. squares	Rsheet (Ω/□)
(-1,2)Q4,2,3	6.00E-05	1.38E-06	0.964	1.000E-02	9.639E+01	43.6	2.2
(-1,2)Q4,2,4	6.00E-05	1.63E-06	0.901	1.000E-02	9.010E+01	36.9	2.4
(-1,2)Q4,2,5	6.00E-05	1.88E-06	0.894	1.000E-02	8.939E+01	3.2	2.8
(-1,2)Q4,2,6	6.00E-05	2.00E-06	0.948	1.000E-02	9.480E+01	30	3.2
(-1,2)Q4,2,7	6.00E-05	2.50E-06	1.022	1.000E-02	1.022E+02	24	4.3
(-1,2)Q4,2,8	6.00E-05	3.00E-06	0.877	1.000E-02	8.769E+01	20	4.4
(-1,2)Q4,2,9	6.00E-05	4.00E-06	0.680	1.000E-02	6.799E+01	15	4.5
(-1,2)Q4,2,10	6.00E-05	5.00E-06	0.617	1.000E-02	6.170E+01	12	5.1
(-1,2)Q4,2,11	6.00E-05	1.00E-05	0.488	1.000E-02	4.879E+01	6	8.1
(-1,2)Q4,2,12	6.00E-05	2.00E-05	0.344	1.000E-02	3.439E+01	3	11.5
(-1,2)Q4,1,12	1.00E-04	2.00E-05	3.132	1.000E-01	3.132E+01	5	6.3
(-1,2)Q4,3,12	2.00E-05	2.00E-05	0.141	1.000E-02	1.410E+01	1	14.1
(-1,2)Q4,4,12	1.00E-05	2.00E-05	0.123	1.000E-02	1.230E+01	0.5	24.6
(-1,2)Q4,5,12	5.00E-06	2.00E-05	0.129	1.000E-02	1.290E+01	0.25	51.6

Table 50. Pad separation, line width, measured voltage, measured current, calculated resistance, number of squares, and sheet resistance for measured TiN resistance devices at (1,3)Q4

Electrode Device:	Pad separation (m)	Line width (m)	Meas. Voltage (V)	Meas. Current (Amp)	Calc. Resistance (Ω)	No. squares	Rsheet (Ω/□)
(1,3)Q4,1,24	1.00E-04	2.00E-05	0.778	5.000E-03	1.556E+02	5	31.1
(1,3)Q4,2,24	6.00E-05	2.00E-05	0.505	5.000E-03	1.010E+02	3	33.7
(1,3)Q4,3,24	2.00E-05	2.00E-05	0.317	5.000E-03	6.340E+01	1	63.4
(1,3)Q4,4,24	1.00E-05	2.00E-05	0.317	5.000E-03	6.340E+01	0.5	126.8
(1,3)Q4,5,24	5.00E-06	2.00E-05	0.262	5.000E-03	5.240E+01	0.25	209.6

Table 51. Measured current, voltages, and calculated resistances of the device (-1, 2) Q1.Contact (PyO) using 4pp and 2pp technique

4pp							
Channel Definitions:							
SMU		Name	Definition				
1	Upper-Right	V1	0-1 V, 0.01 V Step				
2	Upper-Left	COMM	0 V, 105 mAmp Compliance				
3	Lower-Left	I3	Const. 0 Amp, 1 V Compliance				
4	Lower-Right	I4	Const. 0 Amp, 1 V Compliance				
Hold Time:	100 s	Delay Time:	6.5 s	Integration Time:	Long	Auto Cal.:	On
V3max (V)	V4max (V)	I1drawn (Amp)	**Sheet Resistance (Ω/☐)**				
4.79E-01	4.84E-01	2.21E-11	**1.02E+09 +/-0.2E9 Ω/☐**				
2pp							
Channel Definitions:							
SMU	Position	Name	Definition				
1	Upper-Right	V1	0-1 V, 0.01 V Step				
2	Upper-Left	COMM	0 V, 105 mAmp Compliance				
Hold Time:	100 s	Delay Time:	6.5 s	Integration Time:	Long	Auto Cal.:	On
V1 (V)	I2min (Amp)	I2max (Amp)	**Resistance (Ω)**	Sheet resistance			
1	6.00E-13	2.58E-11	**3.976E+10**	1.17E9 Ω/☐			
Hold Time:	0 s	Delay Time:	0 s	Integration Time:	Long	Auto Cal.:	On
V1 (V)	I1min (Amp)	I1max (Amp)	**Resistance1 (Ω)**	I2min (Amp)	I2max (Amp)		**Resistance2 (Ω)**
1	0.00E+00	2.47E-11	**4.049E+10**	4.00E-13	2.49E-11		**4.082E+10**
Hold Time:	0 s	Delay Time:	0.1 s	Integration Time:	Long	Auto Cal.:	On
V1 (V)	I1min (Amp)	I1max (Amp)	**Resistance1 (Ω)**	I2min (Amp)	I2max (Amp)		**Resistance2 (Ω)**
1	0.00E+00	2.50E-11	**4.008E+10**	4.50E-13	2.50E-11		**4.073E+10**
Hold Time:	0 s	Delay Time:	1 s	Integration Time:	Long	Auto Cal.:	On
V1 (V)	I1min (Amp)	I1max (Amp)	**Resistance1 (Ω)**	I2min (Amp)	I2max (Amp)		**Resistance2 (Ω)**
1	0.00E+00	2.47E-11	**4.049E+10**	7.00E-13	2.50E-11		**4.124E+10**
SMU	Position	Name	Definition				
1	Upper-Right	V1	0-1 V, 0.01 V Step				
4	Lower-Right	COMM	0 V, 105 mAmp Compliance				
Hold Time:	0 s	Delay Time:	0.1 s	Integration Time:	Long	Auto Cal.:	On
V1 (V)	I1min (Am[)	I1max (Am[)	**Resistance1 (Ω)**	I4min (Am[)	I4max (Am[)		**Resistance4 (Ω)**
1	0.00E+00	2.46E-11	**4.065E+10**	1.00E-13	2.43E-11		**4.132E+10**
SMU	Position	Name	Definition				
3	Lower-Left	V3	0-1 V, 0.01 V Step				
4	Lower-Right	COMM	0 V, 105 mAmp Compliance				
Hold Time:	0 s	Delay Time:	0.1 s	Integration Time:	Long	Auto Cal.:	On
V1 (V)	I3min (Amp)	I3max (Amp)	**Resistance3 (Ω)**	I4min (Amp)	I4max (Amp)		**Resistance4 (Ω)**

Table 51. Continued

1	0.00E+00	2.64E-11	**3.795E+10**	5.00E-14	2.56E-11	**3.915E+10**	
SMU	Position	Name	Definition				
1	Upper-Left	V1	0-1 V, 0.01 V Step				
3	Lower-Left	COMM	0 V, 105 mAmp Compliance				
Hold Time:	0 s	Delay Time:	0.1 s	Integration Time:	Long	Auto Cal.:	On
V1 (V)	I1min (Amp)	I1max (Amp)	**Resistance1 (Ω)**	I3min (Amp)	I3max (Amp)	**Resistance3 (Ω)**	
1	0.00E+00	2.63E-11	**3.810E+10**	0.00E+00	2.59E-11	**3.861E+10**	
SMU	Position	Name	Definition				
1	Upper-Right	V1	0-1 V, 0.01V Step				
3	Lower-Left	COMM	0V, 105 mAmp Compliance				
Hold Time:	0 s	Delay Time:	0.1 s	Integration Time:	Long	Auto Cal.:	On
V1 (V)	I1min (Amp)	I1max (Amp)	**Resistance1 (Ω)**	I3min (Amp)	I3max (Amp)	**Resistance3 (Ω)**	
1	UNK	UNK	**4.120E+10**	UNK	UNK	**4.000E+10**	
SMU	Position	Name	Definition				
1	Upper-Left	V1	0-1 V, 0.01 V Step				
3	Lower-Right	COMM	0 V, 105 mAmp Compliance				
Hold Time:	0 s	Delay Time:	0.1 s	Integration Time:	Long	Auto Cal.:	On
V1 (V)	I1min (Amp)	I1max (Amp)	**Resistance1 (Ω)**	I3min (Amp)	I3max (Amp)	**Resistance3 (Ω)**	
1	0.00E+00	2.60E-11	**3.854E+10**	5.00E-14	2.53E-11	**3.968E+10**	

VIII.SiO_2 optical properties and simulation fitting

At times the Woollam ellipsometer was not available to us, the Horiba ellipsometer was used to determine the optical properties of the thin films made in this study. To model the optical properties of SiO_2 at the Si/SiO_2 interface in the Horiba software, a Gauchy model was used. The parameters of the Gauchy model for the Si/SiO_2 interface layer were determined from the interface SiO_2 properties in the Woollam software, i.e. intr_JAW.MAT. The Fig. 77below shows the comparison of the Si optical properties between the data from Woollam and Horiba. Fig. 78 shows the int_JAW.mat optical properties and the Gauchy model of the interface. Using this approach similar PyO thickness values were obtained when characterizing the same samples in the Horiba or Woollam ellipsometers.

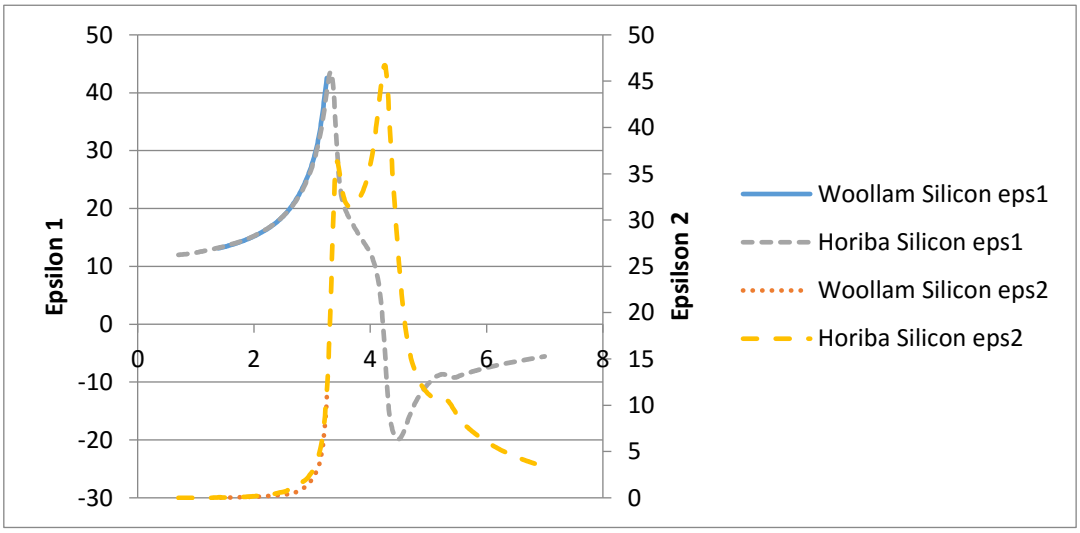

Fig. 79. Si data from different ellipsometer x-axis is energy (KeV)

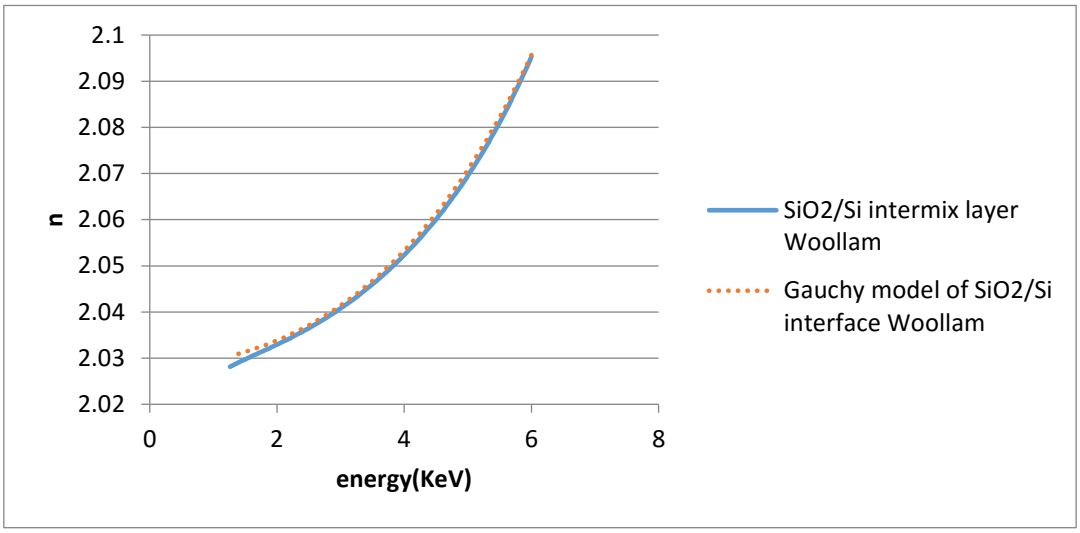

Fig. 80. SiO_2/Si interface layer optical properties simulation

REFERENCES

[1] I. Valyukh, S. Green, H. Arwin, G. A. Niklasson, E. W??ckelg??rd, and C. G. Granqvist, “Spectroscopic ellipsometry characterization of electrochromic tungsten oxide and nickel oxide thin films made by sputter deposition,” *Sol. Energy Mater. Sol. Cells*, vol. 94, no. 5, pp. 724–732, 2010.

[2] H. D. Arnold and G. W. Elmen, “Permalloy, A New Magnetic Material of Very High Permeability,” *Bell Syst. Tech. J.*, vol. 2, no. 3, pp. 101–111, 1923.

[3] H. Katada, T. Shimatsu, I. Watanabe, H. Muraoka, Y. Nakamura, and Y. Sugita, “Induced uniaxial magnetic anisotropy and film magnetostriction in very thin permalloy films,” *IEEE Trans. Magn.*, vol. 37, no. 4 I, pp. 2334–2336, 2001.

[4] E. Y. Tsymbal and D. G. Pettifor, “Perspectives of giant magnetoresistance,” *Solid State Phys. - Adv. Res. Appl.*, vol. 56, no. C, pp. 113–237, 2001.

[5] “No Title.” [Online]. Available: http://ueu.co/.

[6] M. S. Compton, N. A. Simpson, E. G. LeBlanc, M. A. Robinson, and W. J. Geerts, “Electrical and Optical Properties of Permalloy Oxide grown by dual ion beam sputtering.,” in *MRS Proceedings*, 2014, vol. 1708, pp. mrss14–1708–vv08–01.

[7] W. Lee, G. Scherer, and C. R. Guarnieri, “Effects of Oxidation on the Atmospheric Corrosion of Permalloy Films,” *J. Electrochem. Soc.*, vol. 126, no. 9, pp. 1533–1539, 1979.

[8] G. Mihajlović, D. K. Schreiber, Y. Liu, J. E. Pearson, S. D. Bader, A. K. Petford-Long, and A. Hoffmann, “Enhanced spin signals due to native oxide formation in Ni[sub 80]Fe[sub 20]/Ag lateral spin valves,” *Appl. Phys. Lett.*, vol. 97, no. 11, p. 112502, 2010.

[9] C. Du, X. Yang, M. T. Mayer, H. Hoyt, J. Xie, G. McMahon, G. Bischoping, and D. Wang, “Hematite-based water splitting with low turn-on voltages,” *Angew. Chemie - Int. Ed.*, vol. 52, no. 48, pp. 12692–12695, 2013.

[10] S. E. Rios, A. K. Bandyopadhyay, C. Smith, and C. J. Gutierrez, “The enhancement of magnetically ordered oxide layered structures using oxygen radical processing,” in *Journal of Magnetism and Magnetic Materials*, 2005, vol. 286, no. SPEC. ISS., pp. 455–462.

[11] R. Bez and A. Pirovano, *Overview of non-volatile memory technology: markets, technologies and trends*. 2014.

[12] X. Chen, N. Wu, and A. Ignatiev, “Perovskite RRAM devices with metal/insulator/PCMO/metal heterostructures,” in *2005 Non-Volatile Memory Technology Symposium, NVMTS05*, 2005, pp. 125–128.

[13] S. Seo, M. J. Lee, D. H. Seo, E. J. Jeoung, D. S. Suh, Y. S. Joung, I. K. Yoo, I. R. Hwang, S. H. Kim, I. S. Byun, J. S. Kim, J. S. Choi, and B. H. Park, “Reproducible resistance switching in polycrystalline NiO films,” *Appl. Phys. Lett.*, vol. 85, no. 23, pp. 5655–5657, 2004.

[14] D. Ielmini, F. Nardi, and C. Cagli, “Universal reset characteristics of unipolar and bipolar metal-oxide RRAM,” *IEEE Trans. Electron Devices*, vol. 58, no. 10, pp. 3246–3253, 2011.

[15] T. G. Seong, M. R. Joung, J. W. Sun, M. K. Yang, J. K. Lee, J. W. Moon, J. Roh, and S. Nahm, “Bipolar resistive switching behavior of a Pt/NiO/TiN device for nonvolatile memory applications,” *Jpn. J. Appl. Phys.*, vol. 51, no. 4 PART 1, 2012.

[16] G. Ma, X. Tang, H. Zhang, Z. Zhong, J. Li, and H. Su, “Effects of stress on resistive switching property of the NiO RRAM device,” *Microelectron. Eng.*, vol. 139, pp. 43–47, 2015.

[17] X. Tian, L. Wang, X. Li, J. Wei, S. Yang, Z. Xu, W. Wang, and X. Bai, “Recent development of studies on the mechanism of resistive memories in several metal oxides,” *Sci. China Physics, Mech. Astron.*, vol. 56, no. 12, pp. 2361–2369, 2013.

[18] H. Y. Peng, Y. F. Li, W. N. Lin, Y. Z. Wang, X. Y. Gao, and T. Wu, “Deterministic conversion between memory and threshold resistive switching via tuning the strong electron correlation,” *Sci. Rep.*, vol. 2, pp. 1–6, 2012.

[19] “No Title.” [Online]. Available: http://www.lhup.edu/~dsimanek/14/polaroid-short.htm.

[20] H. G. TOMPKINS, *A User’s Guide to Ellipsometry*. 1993.

[21] “No Title.” [Online]. Available: http://www.horiba.com/Us/En/.

[22] “No Title.” [Online]. Available: http://www.jawoollam.com/.

[23] H. Fujiwara, “Spectroscopic Ellipsometry Principles and Applications,” p. 369, 2007.

[24] L. L. Pusep, Yu.A. Milekhin, A.H. Vasiljeva, “IR characterization of thermal SiO2,” *Thin Solid Films*, vol. 209, no. 2, pp. 174–175, 1992.

[25] R. E. Hummel, *Electronic Properties of Materials*, 4th ed. New York : Springer, c2011., 2000.

[26] “No Title.” [Online]. Available: http://www.mksinst.com/docs/UR/.

[27] A. Bergauer, *Technologie Dünner Schichten*. 1991.

[28] F. M. Smits, “Measurements of Sheet Resistivity with the Four-Point Probe,” *Bell Syst Tech J*, vol. 37, no. 3. pp. 711–718, 1958.

[29] “Apollo X SDD Series Specifications.” [Online]. Available: http://www.schmidt.com.tw/www/principal/EDAX/Edax brochure.pdf.

[30] “No Title.” [Online]. Available: http://www.researchgate.net/.

[31] V. Raghavan, “Fe-Ni-O (Iron-nickel-oxygen),” *J. Phase Equilibria Diffus.*, vol. 31, no. 4, pp. 369–371, 2010.

[32] M. A. A. Talukder, Y. Cui, M. Compton, W. Geerts, L. Scolfaro, and S. Zollner, “FTIR Ellipsometry Study on RF sputtered Permalloy-Oxide Thin Films.,” 2016, p. 6.

[33] A. Ghosh, C. M. Nelson, L. S. Abdallah, and S. Zollner, “Optical constants and band structure of trigonal NiO,” *J. Vac. Sci. Technol. A Vacuum, Surfaces, Film.*, vol. 33, no. 6, p. 061203, 2015.

[34] J. Petersen, F. Twagirayezu, P. D. Borges, L. Scolfaro, and W. Geerts, “Ab initio study of oxygen vacancy effects on electronics and optical properties of NiO,” 2016.

[35] C. T. Kirk, “Quantitative analysis of the effect of disorder-induced mode coupling on infrared absorption in silica,” *Phys. Rev. B*, vol. 38, no. 2, pp. 1255–1273, 1988.

[36] U. D. Wdowik and K. Parlinski, “Lattice dynamics of Fe-doped CoO from first principles.,” *J. Phys. Condens. Matter*, vol. 21, no. 12, p. 125601, 2009.

[37] A. Schlegel, S. F. Alvarado, and P. Wachter, “Optical properties of magnetite (Fe3O4),” *J. Phys. C Solid …*, vol. 12, p. 1157, 1979.

[38] A. M. Jubb and H. C. Allen, “Vibrational spectroscopic characterization of hematite, maghemite, and magnetite thin films produced by vapor deposition,” *ACS Appl. Mater. Interfaces*, vol. 2, no. 10, pp. 2804–2812, 2010.

[39] T. Shimada, T. Tachibana, T. Nakagawa, and T. A. Yamamoto, “Site occupation study of ZnFe2O4 and NiFe 2O4 by far-infrared reflectivity,” *J. Alloys Compd.*, vol. 379, no. 1–2, pp. 122–126, 2004.

[40] S. Mochizuki and M. Satoh, “Infrared Spectra of Single-Crystal NiO at High Temperatures,” *Phys. Status Solidi*, vol. 106, no. 2, pp. 667–674, 1981.

[41] T. I. Willett-Gies, C. M. Nelson, L. S. Abdallah, and S. Zollner, “Two-phonon absorption in LiF and NiO from infrared ellipsometry,” *J. Vac. Sci. Technol. A Vacuum, Surfaces, Film.*, vol. 33, no. 6, p. 061202, 2015.

[42] A. M. Hofmeister, E. Keppel, and A. K. Speck, “Absorption and reflection infrared spectra of MgO and other diatomic compounds,” *Mon. Not. R. Astron. Soc.*, vol. 345, no. 1, pp. 16–38, 2003.

[43] N. Demoli, “Optimization in mapping of correlation filters in a liquid crystal display based frequency plane correlator,” pp. 0–6, 1999.

[44] R. S. Nasyrov, V. M. Lopatinb, and B. S. Lunin, “Optical transmission and internal friction in fused quartz melted from natural raw materials,” *Mendeleev Commun.*, vol. 22, no. 1, pp. 260–262, 2012.

[45] D. Brandon and W. D. Kaplan, “Microstructural Characterization of Materials,” in *Microstructural Characterization of Materials*, 2008, pp. i–xiv.

[46] J. Goldstein, D. E. Newbury, D. C. Joy, C. E. Lyman, P. Echlin, E. Lifshin, L. Sawyer, and J. R. Michael, *Scanning Electron Microscopy and X-ray Microanalysis*. 2012.

[47] “No Title.” [Online]. Available: http://www.kayelaby.npl.co.uk/.

[48] T. Nagatomi, “Monte Carlo modeling of electron-excited X-ray emission from bulk materials and thin-film/substrate systems,” *Surf. Interface Anal.*, vol. 37, no. 11, pp. 887–894, 2005.

[49] P. Hovington, D. Drouin, R. Gauvin, D. C. Joy, and N. Evans, “CASINO: A new monte Carlo code in C language for electron beam interactions-part III: Stopping power at low energies,” *Scanning*, vol. 19, no. 1, pp. 29–35, 2006.

[50] D. Drouin, A. R. Couture, D. Joly, X. Tastet, V. Aimez, and R. Gauvin, “CASINO V2.42 - A fast and easy-to-use modeling tool for scanning electron microscopy and microanalysis users,” *Scanning*, vol. 29, no. 3, pp. 92–101, 2007.

[51] R. Gauvin, “What Remains to Be Done to Allow Quantitative X-Ray Microanalysis Performed with EDS to Become a True Characterization Technique?,” *Microsc. Microanal.*, vol. 18, no. 05, pp. 915–940, 2012.

[52] J. L. Pouchou, “X-Ray microanalysis of stratified specimens,” *Anal. Chim. Acta*, vol. 283, no. 1, pp. 81–97, 1993.

[53] R. Gauvin, E. Lifshin, H. Demers, P. Horny, and H. Campbell, “Win X-ray: a new Monte Carlo program that computes X-ray spectra obtained with a scanning electron microscope.,” *Microsc. Microanal.*, vol. 12, no. 1, pp. 49–64, 2006.

[54] J. Evertsson, F. Bertram, F. Zhang, L. Rullik, L. R. Merte, M. Shipilin, M. Soldemo, S. Ahmadi, N. Vinogradov, F. Carlà, J. Weissenrieder, M. Göthelid, J. Pan, A. Mikkelsen, J. O. Nilsson, and E. Lundgren, “The thickness of native oxides on aluminum alloys and single crystals,” *Appl. Surf. Sci.*, vol. 349, pp. 826–832, 2015.

[55] Y. K. Ko, D. S. Park, B. S. Seo, H. J. Yang, H. J. Shin, J. Y. Kim, J. H. Lee, W. H. Lee, P. J. Reucroft, and J. G. Lee, “Studies of cobalt thin films deposited by sputtering and MOCVD,” *Mater. Chem. Phys.*, vol. 80, no. 2, pp. 560–564, 2003.

[56] N. Martin, J. Sauget, and T. Nyberg, “Anisotropic electrical resistivity during annealing of oriented columnar titanium films,” *Mater. Lett.*, vol. 105, pp. 20–23, 2013.